Global energy minimisation of arterial trees with application to embolic stroke

Thesis

How to cite:

Keelan, Jonathan Joseph (2016). Global energy minimisation of arterial trees with application to embolic stroke. PhD thesis The Open University.

Global Energy Minimisation of Arterial Trees with Application to Embolic Stroke

Jonathan Joseph Keelan

Department of Physical Science

The Open University

This dissertation is submitted for the degree of

Doctor of Philosophy

2015

DATE OF SUBMISSION: 8 JANUARY 2016

I would like to dedicate this thesis to my loving parents ...

Declaration

I hereby declare that except where specific reference is made to the work of others, the contents of this dissertation are original and have not been submitted in whole or in part for consideration for any other degree or qualification in this, or any other University. This dissertation is the result of my own work and includes nothing which is the outcome of work done in collaboration, except where specifically indicated in the text. This dissertation contains less than 65,000 words including appendices, bibliography, footnotes, tables and equations and has less than 150 figures.

Acknowledgements

As my advisor, Jim Hague deserves thanks for the majority of this thesis. The central idea behind this thesis was his, and over the years he has continuously produced large quantities of valuable input and advice. The rest of my supervisory team, Uwe Grimm and Emma Chung have also helped immeasurably.

The CEI and various members of the Open University, students and faculty, who are too numerous to name, have helped greatly in various roles; as friends, as colleagues, as confidants and fellow commiserators.

My parents, Ronald and Dorothy Keelan, brothers and the rest of my family also deserve thanks for their continued support and love.

YOUR ACCEPTANCE

1	**Student details**	Your full name: Jonathan Joseph Keelan Personal identifier (PI): B816491 Affiliated Research Centre (ARC) (if applicable): Department: School of Physical Sciences Thesis title: Global energy minimisation of arterial trees with application to embolic stroke
2	**Authorisation statement**	I confirm that I am willing for my thesis to be made available to readers by The Open University Library, and that it may be photocopied, subject to the discretion of the Librarian Signe[redacted].. Print name: Jonathan Joseph Keelan
		Date: 20/01/2017 DD/MM/YY
3	**British Library Authorisation (PhD and EdD candidates only)**	The Open University has agreed that a copy of your thesis can be made available on loan to the British Library Thesis Service on a voluntary basis. The British Library may make the thesis available online. Please indicate your preference below: ☒ I am willing for The Open University to loan the British Library a copy of my thesis OR ☐ I do not wish The Open University to loan the British Library a copy of my thesis

Abstract

Computer generation of optimal arterial trees has previously been limited to the production of locally optimal configurations. The application of a global optimisation algorithm allows for the generation of vasculatures with consistent structure. Comparison of this structure to that of *in-vivo* vasculatures allows the determination of to what extent the vascular structure is the result of energy minimisation. In this thesis an algorithm capable of generation globally optimal vascular trees in geometries derived from medical imaging is developed.

We begin by outlining a small set of constraints which capture physiological principles guiding the organisation of arterial trees. The constraints are then used to produce an algorithm capable of finding the minimal energy configuration of a given arterial tree. The algorithm is used to produce both coronary and cerebral vasculature, and the latter is generated in geometries segmented from MRI data of a human brain. The trees are compared both morphologically and structurally to those found *in-vivo*. The morphological comparisons for the coronary vasculature show excellent agreement with experiment. The positions of the larger coronary arteries in the generated trees agree extremely well with experiment, suggesting that structure of the coronary vasculature is the result of energy minimisation.

The generated cerebral vasculature approximates the vascular territories of the major cerebral arteries, however the morphological comparisons show that the structure of the cerebral arteries is likely not the result of energy minimisation. The cerebral vasculatures is used to extend a statistical model of embolic stroke to include the effects of branching asymmetry, and an analytic approximation to the statistical model of embolic stroke is developed and validated. It is found that branching asymmetry produces an overall reduction in the level of blockage occuring during an embolic event.

Contents

List of Figures

Chapter 1

Introduction

The creation of realistic, morphologically accurate arterial trees using simple optimisation criteria has seemed an achievable since Cecil Murray published his 1926 paper entitled "The Principal of Minimum Work". Previous attempts at realising this goal have fallen short in both the replication of morphological properties and the larger geometric structure of living arterial trees. This thesis represents the first application of a global optimisation procedure to the problem of arterial tree generation, and demonstrates the method by specific application to both the coronary and cerebral vasculatures. As a specific application, the cerebral trees are used to extend a statistical model of embolic stroke due to Hague et. al.[46].

Arterial trees provide the conduit through which blood, containing nutrients and oxygen, is delivered to tissue. Arterial trees are complex, three dimensional networks comprised primarily of bifurcations, although trifurcations do occur, and they span length scales ranging from μm to cm.

In 1926 Cecil Murray published a paper entitled "The Principal of Minimum Work"[94]. This paper used a simple optimisation criteria to derive a mathematical relationship between the radii of the parent and daughter arteries involved in a bifurcation. The fundamental premise of his work was that the driving force of natural selection had resulted in an arterial bifurcation process which minimises energy expenditure. The energetic cost of an arterial tree is broken down into two separate contributing factors: the pumping power required to move blood through the system, due to viscous dissapation, and the volumetric energy cost of the blood required to fill the system. As will be detailed in later chapters, these two costs are at odds with one another, and their summation results in a function which has a single minimum.

1.0.1 Previous Models

Arterial trees deliver oxygen rich blood to tissues, remove waste products of cell motabolism and provide moisture in via osmosis from blood to cell. Their construction is essential to tissue growth in both normal development and theprogess of disease (e.g. cancer). The vascular system of man spans a large range of length scales ($\approx$ 1cm to 10μm), making imaging of the entire vascular system *in vivo* difficult. Models of biological function such as tissue growth, or dysfunction such as stroke and heart attack, can be improved by accurate models of the vascular tree at all length scales. In addition, our understanding of the vascular system and its properties can also be improved by the development of models which accurately capture its behaviour. To this end, various models capable of generating vasculature have been proposed; this section aims to briefly outline a selection of those attempts.

Due to their complexity, optimisation problems are frequently tackled using computational methods. The optimisation of a single bifurcation can be done by hand, but the optimisation of a system of many thousands of connected arterial segments, in both network structure and spatial position, requires an algorithm amenable to computation. Previous work to this end produced a solution known as Constrained Constructive Optimisation (CCO), which builds arterial trees by iteratively adding, and then optimising, new segments. The method produces realistic *looking* arterial trees, but fails to accurately reproduce the morphological and geometric features of real trees. In recent years, various extensions to the orginal CCO paradigm have been attempted, with varying levels of success. One primary difficulty that is yet to be overcome is CCO's inability to grow vasculatures for complex organ geometries e.g. the brain, where there exist multiple tissue types, non-convex geometries and multiple boundary conditions. A more fundamental limitation of the CCO algorithm is its inabillity to find the global minimum of the energetic cost: CCO builds arterial trees iteratively and once a segment is added it is never re-optimised.

In addition to CCO, which is based upon optimisation principles, there are various other methods aimed at producing 3D arterial structures *in-silico*. Perhaps the most impressive are the morphometric models, which produced arterial trees from detailed morphometric databases containing the properties of many millions of arterial segments. The positions and morphology of the largest arteries are often taken from imaging data, and the morphometric database is used to reconstruct the rest of the tree. The morphometric database contains probability distributions relating an arteries radii to its length, as well as topological distribution indicating the probability of arteries being connected to one another via a bifurcation. While these methods are capable of producing large and accurate arterial trees (computational generation based on optimisation simply can not compete with the scale), large morphometric databases are required to construct them. Such databases do not exists for a large range of organ specific vasculatures. In addition, they provide no new insight into the structure of the arterial tree. Comparison of optimisation algorithms with real arterial trees allow us to answer two important questions: is there an internal procedure which guides an energetically minimal design? and if so, what are the components which make up the optimisation criteria? Answering these questions may allow for examination of disease risk due to abnormally formed arterial trees, or allow imaging software to add educated guesses at scales below the imaging resolution.

Beyond morphometric models, there are a wide variety of models aimed at mimmicking angiogenisis, particularly with regard to tumor formation. These mathematical models are vast and varied, but they are often aimed towards the microvasculature and involve the modelling of chemical signals. The large scale modelling performed by optimisation procedures aims to reproduce the major arteries and arterioles of specific organs, where variation in the vasculature of that organ appears to be relatively stable over a population.

Finally, there are also fractal models, which attempt to reproduce various fluid dynamical and morphometric properties of real vasculatures. They are an important tool in the understanding of arterial trees, but frequently they do not contain spatial data or do not result in a 3D structure.

1.0.2 Experimental Data

For any computational model, verification against experimental data is a key objective. The matching of a model against experimental data not only validates the model itself, but also partially the conclusions and inferences obtained from it. For arterial trees there are two primary areas of experimental data: morphological and spatial. The morphological data comprise radii, lengths and network structure of the tree, whereas the spatial data comprises the location of individual bifurcations and the paths taken by the arterial segments. To be successful an arterial generation algorithm must be capable of producing an arterial tree with reasonable agreement to both morphologicla and spatial experimental data.

There has been a vast amount of data published regarding arterial trees. Verification of Murray's "Principal of Minimum Work" has been the focus of many publications, but a consensus over its validity has not been reached. A large morphological study has been performed on the porcine coronary vasculature, but such detailed experimental data is rare. Studies on the microvasculature of the human cerebral cortex have also been performed, but detailed morphometric data spanning larger length scales does not appear to exist. There are numerous publications which investigate specific fluid dynamical quantities of the vasculature of specific organs, or investigate the morphology of arterial trees at specific length scales, but comprehensive morphological data for specific organs appears to be rare.

1.1 Motivation

The main purpose of this thesis is to develop, document and validate a new algorithm capable of generating morphologically and spatially realistic arterial trees *in-silico*, using a global optimisation procedure. The current standard algorithm for generating arterial trees using optimisation is CCO, however the trees it produces lack certain morphological properties of real arterial trees, and also can not reproduce certain geometric features of organ specific vasculature known to be present across a population. The algorithm developed in this thesis is capable of reproducing organ specific vasculature features, and produces trees which are have increased morphological accuracy in comparison to those of CCO whilst simulateously producing them for more complex geometries.

In order to properly assess the "Principle of Minimum Work" as applied to *whole* arterial trees, rather than single bifurcations, the algorithm employs an optimisation routine known as Simulated Annealing (SA). The SA algorithm, in contrast to the optimisation method employed by CCO, allows for the entire topological and geometric space to be explored. While no algorithm could be guaranteed to find the global energetic minimum of an arterial tree in finite time, we demonstrate that for smaller scale trees a consistent minimum is approached, and find that even for trees with 1000s of segments, a consistent structure in the larger arteries appears. The generated trees are visually similar in structure to *in-vivo* organ specific arterial trees, and match the morphological data well. As this is the first algorithm to globally optimise an entire arterial tree, we also present the first evidence that the larger arterial tree structure of the coronary arteries is, atleast partially, a result of a tendency to minimise energy expenditure.

The ability to generate morphologically and spatially realistic arterial trees affords will afford models who use such trees the potential to improve their results. A motivation for the production of this model is the statistical model of embolic stroke produced by Hague *et. al.*, which previously used a simplistic symmetrically bifurcation tree as its input.

1.2 Outline

The second chapter of this thesis provides a literature background on arterial tree research, as it relates to arterial tree modelling. The literature on arterial trees is incredibly vast, and no literature review could hope to cover it all; Chapter 2 aims to provide a thorough background specifically in relation to the computational generation of arterial trees. There exist already numerous high quality review papers relating to vascular morphology and where appropriate these have been highlighted for the interested reader.

The third chapter is divided into two sections. In the first section I develop a small set of criteria which are likely to govern the overall growth of arterial trees. This is not an attempt at indentifying the underlying chemical pathways or processes, but is a coarse graining of the "objectives" of an aterial tree framed in terms of an optimisation problem. Included within these objectives is the minimal energy hypothesis of Murray. In the second section I detail the specific computional representation of the previously identified optimisation criteria, and discuss the Simulated Annealing method. Finally, the consistency and convergence of the developed algorithm are tested on a small two dimensional arterial tree.

The fourth chapter applies the previously developed algorithm to a simplified ellipsoidal heart model, and the resulting trees are compared both morphologically and visually to real porcine coronary vasculatures. The visual inspection shows that the major arteries of the heart are faithfully reproduced by the algorithm, a first for a generative algorithm, and morphological comparison reveals good agreement with published experimental data.

The fifth chapter is divided into two sections. In the first the algorithm is applied to a cerebral geometry segmented from real MRI data. The generated tree is again compared both visually and morphologically to experimental data. It is found that though the morphological data comparisons remain encouraging, the structure of the larger arteries deviates from that found *in-vivo*, most likely due to the complex geometry of the brain. In the second half of the chapter the generated tree is used as input to a statistical model of embolic stroke, and the results of the simulations are compared with those generated for a simple symmetrically bifurcating tree. An analytic approximation for the embolic stroke model is also constructed.

In the sixth chapter, I present some interesting properties of both the simulated annealing algorithm and the optimised trees it produces. The parameter space of the algorithm is fully explored and metrics such as the fractal dimension of the trees are presented. An analytic derivation of the optimal bifurcation exponent for symmetric trees containing arbitrary segments is derived, and its results are compared to those generated by the algorithm.

In the final chapter I summarise the results of the thesis, as well as the limitations, and outline extensions and improvements which could be made to the algorithm. Possible applications to current techniques are also summarised, as well as some speculation on what the uses of an optimal arterial tree generating algorithm may be in the future.

Chapter 2

Optimal Arterial Trees

2.1 Introduction

In this chapter we will review past research into the morphology and geometry of mammallian vascular systems, as well as computational methods used for their generation.

2.2 The Bifurcating Tree

Transport networks are pervasive in biology[11]. The requirement of biological organisms to supply nutrients and remove waste from their tissue has led to the evolutionary development of various transport solutions. For instance in insects, who lack any form of pumping respiration, the transport network for oxygen works through a process of diffusion which begins in microscopic pores on the insect's outer surface, the tubes of which bifurcate and divide perfusing air through the entire insect[39]. In Man, and many other organisms, the main nutrient transport mechanism is blood, which is perfused through tissue by means of a bifurcating tree of vessels[152]. In some plants the transport system for nutrients is again a bifurcating tree, visible on the surface of leaves[117]. While the branching tree design is common in nature, the following will focus primarily on its properties as they relate to blood transport in mammals, particularly humans.

Bifurcations are by far the most common method for flow division within arterial networks. Trifurcations do occur in less than 1% of cases[4], with higher order divisions being even less common. For the purpose of computational modelling a bifurcating system of vessels is an adequate characterisation, where the rare event of a trifurcation can be effectively captured if the distance between bifurcations becomes sufficiently small (Fig 2.1). Bifurcations allow large arteries to connect to the microvascualture in order to facillitate the effective exchange of nutrients and oxygen from the blood, for waste products from cells. Oxygen echange is primarily diffusion driven [37], requiring large surface to volume ratios, low flow rates and thin vessels walls in order to occur effectively. The combination of thin vessel walls and low flow rates means that fluid pressure within the vessel also has to be low. Within the larger arteries, e.g the aorta, pressures are at a maximum (100mmHg[36]), and are far too high to supply the microvasculature without destructive effects. As a result of these restrictions, the distributive duties of the arterial system also include the need to drop significant amounts of pressure during the journey from aorta to microvasculature. Since resistance to flow scales as $\frac{1}{r^4}$ for purely viscous flow, the majority of the pressure is dropped in the smaller arterioles, which also modify their radii in response to pressure changes via a process called autoregulation[57].

The microvasculature is arcade in structure[90], allowing for significant amounts of cross flow between tissue regions. One suboptimal solution to the blood supply problem then could be to have a single, large arcade structure, supplying blood to all tissue within the organism. The previously mentioned scaling law for vascular resistance demonstrates why this solution is suboptimal. The vascular resistance would be high enough that blood would never reach the outer edges of the system if there were only a single pumping source. Arterial systems are adapted to not only distribute blood to the microvasculature efficiently, but also to transport it there. Taking a single path from aorta to an area of microvasculature,

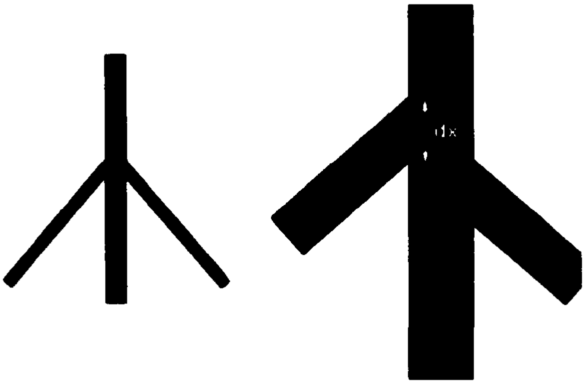

Figure 2.1: A trifurcation can be considered as a special case of bifurcation, where the distance between successive bifurcations dx becomes sufficiently small.

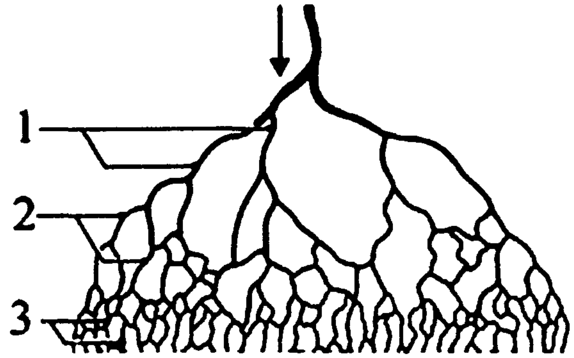

Figure 2.2: The three sections of a typical arterial tree. 1)The transportative stage consisting of large ($>$ 1mm) diameter vessels, which transport blood to a specific organ or location. 2) The distributive stage, where smaller ($50\ \mu m < r <$ 1mm) arterioles distribute blood throughout the tissue. 3) The microvascular regime, where arcade network structure dominates and oxygen and nutrient exchange occurs. ($r < 50\ \mu m$)

we can identify 3 specific regions of the arterial system. The first is purely transportative, a single branch from the aorta transporting blood in bulk to the tissue. The second is distributive, involving many bifurcations, dropping pressure and reducing flow, dividing blood between areas of tissue. The third is the microvasculature, which allows for effective material exchange (Fig. 2.2). In a real arterial system the demarcation between the transportative and distributive regions will not be sharp, however the distinction is still useful and provides the basis for a quantitative analysis of arterial tree structure.

As with all biological systems, the maintainence and use of an arterial system require energy. This energetic cost includes not on the pumping of the heart to overcome dissipitave effects, but also the production of enough blood to fully fill the system. Since red blood cells have a lifetime of 1 month, this blood volume must constantly be maintained and so represents a constant energetic strain on the arterial system. These two energy costs have solutions which directly oppose one another. To minimise the pumping power required, an arterial system should be arranged so as to minimise the the vascular resistance. As noted earlier, vascular resistance of a single artery is proportional to $\frac{1}{r^4}$, and so the pumping power optimised system would consist of a large, single artery snaking through the body and bifurcating highly asymmetrically directly into the microvascular system. In this case, the volume of blood required to fill the system would be huge, as the large artery must be entirely filled to be viable. In contrast, to minimise blood volume, which scales as r^2, the tree would look much like the suboptimal microvascular system outlined earlier. The aorta would bifurcate as quickly as possible down to the microvascular level.

In general the competition between two competing factors in any problem signals the beginning of an optimisation problem, and this case is no different. Balancing the energetic cost of pumping and maintaining blood is a driving force in the generation of arterial tree structure and morphology, but to what extent vasculature is dependent of these factors requires examination of the evidence. In this next section we will review the past and present experimental and theoretical investigations into the optimality of arterial trees for various animals.

2.3 Optimality Principles for Arterial Trees

2.3.1 Murray's Law

The idea that transport systems of biological organisms would evolve to an optimal state was first proposed by Murray[94]. Using the principle of mimimum work and volume, applied to a Newtonian fluid of constant viscosity undergoing Poiseuille flow in a cylindrical tube, Murray was able to derive a theoretical relationship between the radii of parent to daughter vessels at a bifurcation

$$r_p^3 = r_a^3 + r_b^3 \tag{2.1}$$

Where r_p refers to the parent vessel radius and r_a and r_b refer to the daughter vessels. This relation finds the minimum of the function

$$F = \frac{8\mu Q^2 l}{\pi r^4} + bl\pi r^2 \tag{2.2}$$

Where the first term on the right hand side (rhs) is the power dissipated by a fluid undergoing poiseuille flow of magnitude Q in a cylindrical tube of length l and radius r, and the second term is the volume of the same tube. Using elementary calculus and assuming a constant flow in the pipe, Murray shows that the minimum of this function is found when

$$Q^2 = \frac{r^6 \pi^2 b}{16\mu} \tag{2.3}$$

For a flow through a bifurcating tube consisting of an incompressible fluid, the flow through the parent vessel will necessarily equal the sum of the flow through the two daughter vessels, so that

$$Q_p = Q_a + Q_b \tag{2.4}$$

Combining Eq. 2.3 and Eq. 2.4 and assuming constant viscosity, we arrive at Murray's law (Eq. 2.1). While the assumption of poiseuille flow is valid for certain sections of the vasculature[79], elsewhere the behaviour can be more complex. In the larger arteries of the body flow is highly pulsatile[103], and in the microvasculature there are non-Newtonian[49] effects. Even when laminar flow is a valid assumption there are other effects which require

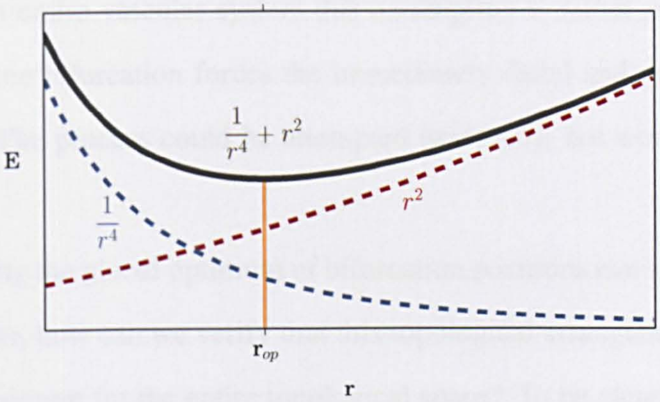

Figure 2.3: Schematic diagram of the energetic cost constributions from volume and fluid dynamic dissipation. The location of the minimum corresponds to the solution found by Murray.

quantification, such as the elastic arterial walls, kinetic energy of the blood, turbulence etc. In response to these additional criteria, Murray's law has been frequently adapted and expressed instead as an instance of a power law relationship between arterial radius and flow, such that:

$$Q = r^{\gamma} \tag{2.5}$$

Where in the specific case of Murray's law $\gamma = 3.0$. The exact value of gamma, as will be shown in the following section and investigated analytically in Chapter 6, appears to on the radius, which in turn is most likely a result of various competing fluid dynamical and biological effects. In computational models the value of γ is fixed at some experimentally determined value relevant to the vasculature being modelled. Murray exposed a principle governing a single artery, however arterial trees consist of many millions of arterial segments and their associated bifurcations. The imposition of Murray's law upon the radii of an arterial system is not sufficient to guarantee global optimality of the entire system. The position of the bifurcation must also be determined. The application of Murray's law to bifurcation position is relatively straightforward but algebraicly tedious, but the primary constraint in the calculation is that the locations of the root entry and daughter exit sites are fixed. In the context of an entire vascular system this assumption is rather paradoxical: optimising the position of one bifurcation forces the immediately distal and proximal bifurcations to be suboptimal. The process could be attempted iteratively, but would be computationally rather slow.

Even assuming the global optimum of bifurcation positions can be found for a particular set of bifurcations, how can we verify that this topological arrangement is the one resulting in the global minimum for the entire topological space? To be clear, the geometric optimisation of single bifurcations ignores the pertinent problem of topological freedom: how the bifurcations are connected to one another. Since each topological configuration must be optimised individually, and there is no way to predict how a topological change will effect the minimum, it would be necessary to enumerate all the non-degenerate topological states and calculate their geometric minimums. This process would be computationally prohibitive for even the most modestly sized trees, as the topological space grows as the Catalan numbers.

These isssues however do not preclude an analysis of the experimental evidence for Murray's law. Various measurements have been made of arterial trees spanning a wide variety of species. The following section is by no means exhaustive, but represents a detailed picture of the current understanding of the morphology of arterial trees.

2.3.2 Bifurcation Exponent

Murray's prediction that the bifurcation exponent should be exactly 3 in order to optimise power and volume is clearly theoretically correct (to first order approximation at least), however the level of various assumptions within the Murray's derivation means that real biological system show significant deviation from this value. The first is the assumption of laminar flow. In many bifurcations far away from the heart, blood flow is nearly laminar[79] (although not too far, where at the micrometer scale blood become non-Newtonian[49]), however in the large arteries of organs such as the heart and brain, the blood flow can exhibit turbulent behaviour [126]. In addition, pulsatile flow is still present to a large degree, which requires the inclusion of energy loss through pulsatile wave reflection at bifurcations. This is enough to suggest that the bifurcation exponent value of 3 predicted by Murray is incorrect, and indeed when measured it has been shown to be as low as 1.8 in the larger arteries[60] and as low as 1.3 in the carotid bifurcation[10]. The exact mechanism behind this relationship will be investigated in Chapter 6, however for now it is enough to note that as the radii decrease there is a general trend upwards to a value of 3 in the capillaries[112], consistent across species and organs.

Horsfield and Woldenberg analysed the bifurcation ratios for the human pulmonary arteries tree using resin casts. They found the bifurcation exponent to be 2.3 ± 0.1 which is equal to the value required for minimum power dissipation for fully developed turbulent flow, however even in the largest pulmonary arterial flow is most likely not turbulent. They concluded that other factors must be at work in determining the optimum branching exponent, such as the turbulence created at bifurcations[52]. Work by Kassab *et. al.*[70] and Restrepo[112] has shown that the bifurcation exponent is most likely a function of arterial radius, rising from 2.0 in the larger arteries, to > 3.0 in the microvasculature. Further analysis of the effects of pulsate flow have shown that the optimal bifurcation exponent in an artery experiencing fully pulsatile flow is 2.0[141]. Theoretical analysis of elastic wall arteries predicts a branching exponent value of 2.33 which matched experimental data for the pulmonary arterial tree[98].

By showing that the apex point of a bifurcation, that point which splits the flow, can always be located such that the flow division matches that required in the branches, and in turn that this apex position is compatible with Murrays law, Zamir was able to show that the local optimality of a bifurcation, in terms of the orderliness of flow through a bifurcation, is compatible with the global, geometric optimality condition of Murray[148]. Beare *et. al* measured the bifurcation exponent of the carotid bfiurcation in 45 subjects and found that the exponent value ranged from 1.3 to 1.6.

Rossitti and Löfgren analysed the bifurcation exponent and branching angles for the internal carotid, middle and anterior cerebral arteries and found a branching exponent of 2.9 ± 0.4 but found no correlation between theoretical and measured branching angles[116]. This is in contrast to data from Frame and Sarelius who looked at the bifurcation angles and exponent for the microcirculation of a Golden Hamster cremaster muscle[40]. They compared measured data for the branching angles to the theoretical predictions of different optimality models (volume, power, shear stress, surface area) but found no correlation. In addition they calculated the value for the bifurcation exponent using the measured values of branching angle and diameters, finding large variations in the value for bifurcations along the length of a feed arteriole[40]. Revellin *et. al.*[113] performed a theoretical eximination of the optimal bifurcation exponent under the assumption of non-newtonian flow. They found the optimal exponent remained at Murray's value of 3.0 if a volume constraint was present. The inclusion of a surface constraint produced optimal exponent values ranging from 2.42 to 3.0, depending upon the fluid properties used in their model. This implies that in regions of highly non-newtonian flow, there is likely to be some deviation from Murray's law, to an extent similar to that found in the larger arteries. Experimental measurements performed on the smaller arterioles however imply that a value of 3.0 is valid for all but the largest arteries[106, 116].

Wright *et. al*[144] performed an analysis on segmented cerebral arterial trees from 64 TOF MRI images of healthy individuals. The bifurcation exponent was found to vary as a function of branching order (calculated as the number of bifurcations occuring from the root of the tree to the segment), with an average value of 2.5. Due to the 0.5mm resolution of the MRI images, only the larger cerebral arteries were examined. Cassot et. al.[22] performed a detailed morphometric study of the cerebral microvasculature (radius less than 300μm), and found an average bifurcation exponent of 3.0, but with significant variation.

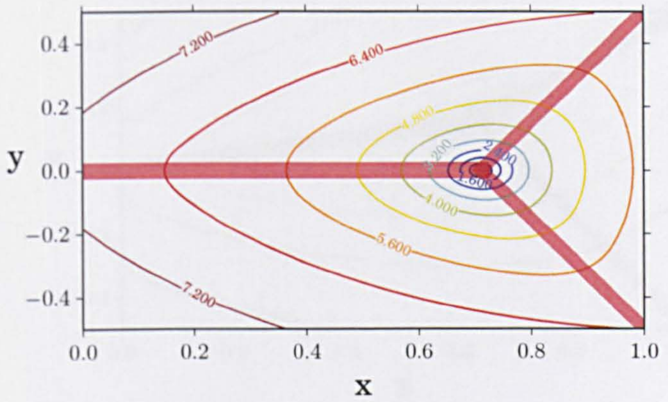

Figure 2.4: Bifurcation position shown for a symmetric bifurcation with an exponent of 3.0. The contours denote the energetic cost of the bifurcation at that position.

A theoretical study of the effect of a heterogenous branching exponent was performed by Karau *et. al*[63], who found that the mean value of the branching exponent had little effect on the wall shear stress throughout the tree. While the true value of the bifurcation exponent appears to be dependent upon the radius of the parent artery, the experimental data does suggest that in most cases a value between 2.0 and 3.0 is appropriate at arteriole length scales. Theoretical studies of the bifurcation exponent in the microvasculature (less than a few hundred micrometers) and large arteries (carotid, aorta etc) suggest pulsatile flow, arterial elasticity and the non-Newtonian properties of blood can explain some of the deviation from Murray's exponent value of 3.0.

2.3.3 Branching Angles

The diameter of bifurcations is not the only relevant geometrical parameter, angles also contribute to the optimality of a bifurcation. Murray extended his work on the optimal branching diameters to include expressions for the optimal angle of bifurcation[95], however this analysis presupposes a cubic relationship between vessel diameter and flow, which in turn implies a preexisting balance between volume and power optimisation. Zamir performed a theoretical analysis of optimal arterial branching angles for the 4 separate optimality con-

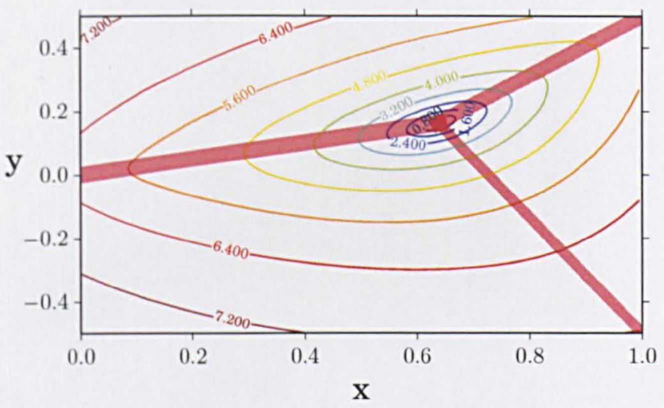

Figure 2.5: Bifurcation position shown for an asymmetric bifurcation with an exponent of 3.0. The contours denote the energetic cost of the bifurcation at that position. In comparison to a symmetric bifurcation, the angle of the parent artery to the daughters is changed. The larger daughter makes a smaller angle with the parent.

ditions of minimum surface area, volume, pumping power and endothelial drag[147]. The diameters of daughter and parent arteries were considered to be separate due to the long range vascular effects of arterial diameter, where the analysis of Zamir was concerned only with the local geometry. It was found that for certain values of the branching angles all four conditions were very close to their respective minima, but in general the conditions did not agree on the most optimum angle. In addition it was noted that any theoretical analysis will only give a rough guide to the reality found in nature, as natural biological scatter will always cause departures from optimality, and that in certain regions of the vasculature (e.g the aorta), geometry and concerns such as pulsatile wave reflection will cause significant departures from the optimality principles considered. Empirical verification of the theoretical optima presented was attempted in 1979 by Zamir and Chee[153] and as predicted the biological scatter was significant. The significant scatter of bifurcation angles posed a problem to Murray's idea of optimal bifurcations. Zamir and Bigelow investigated the size of the biological scatter, but in contrast to previous work they measured the scatter in terms of its energetic cost. They found that a deviation from optimality causing a 2% increase in cost was enough to include almost all the biological scatter found[150]. It thus seems reasonable

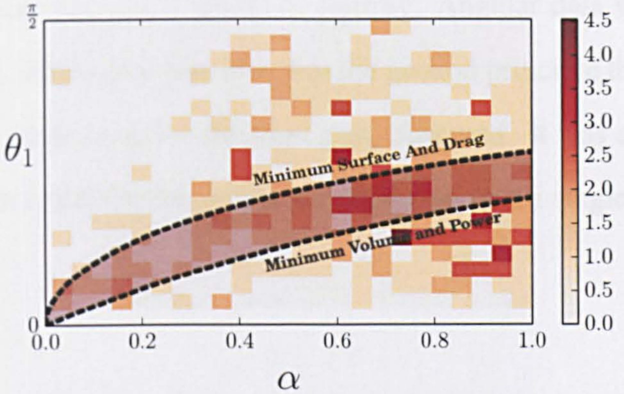

Figure 2.6: Bifurcation angles[143, 150] and theoretical curves for various arterial trees as a function of the branching asymmetry (data is for the larger daughter). There is a large amount of scatter, however this consistutes a relatively small deviation in the energetic cost of the bifurcation.

to conclude that, while nature may be inexact in its workings, arterial bifurcation angles do follow the optimality principles of Murray.

Zamir examined the local properties of arterial branches and their relation to the global optimality conditions of Murray[148]. Each arterial branch has a local structure, the most important feature of which is the position of the apex of the bifurcation relative to the two outside edges of the daughter vessels, which in turn defines the point of division of the parent's stream lines. It was shown that the position of the apex required to divert the nominal amount of flow with respect to Murray's law was compatible with a locally optimal apex position. This is an important point which would be otherwise neglected in a first order fluid dynamics simulation of the arterial tree, and was indeed neglected in the method devised by Murray. That flow division is compatible in an optimal way with the radii defined in Murray's law, lends support to the use of laminar flow approximation in the modelling of the fluid dynamics of bifurcation. Kassab *et al.* analysed 700 large (diameter > 1mm) segments of the porcine coronary arterial tree. Bifurcations angles were found to follow optimality but with significant scatter[143]. Zamir examined arterial bifurcations in the rat cardiovascular system[154]. Diameter data was also recorded and found to be in good agreement with the theoretical model of Murray. Angular data was again subject to large biological scatter, although it was seen that the general principle that larger daughter vessels having a smaller angle was, for the most part, observed. It was also found that in the vast majority of cases, arterial bifurcations are planar, so that a single bifurcation is effectively two dimensional.

2.3.4 General Scaling Laws of Vascular Trees

The structure of the arterial tree can be described in bulk by various power law relationships derived from principles similar to those used by Murray. Effectively these models are extensions of Murrays law applied to large arterial trees rather than single bifurcations. In Chapter 6 we will explore a new method aimed at calculating the optimal bifurcation exponent for a symmetric binary tree, however these scaling arguments aim to produce power law relationships between the various physical properties of arterial trees. Kassab demonstrated a more general scaling law for biological transport networks based upon the minimum energy hypothesis and using a stem-crown formalism (See Fig 2.7) which coalesces the distal subtree of a segment into a single set of parameters (resistance, length etc). The derived scaling exponents show a dependence on crown resistance and this was used to form a theoretical prediction which could be compared with a least squares fit. The values from theory were found to be in good agreement with those of the least squares fit. In analysis of the exponent predicted by Murray, it was found the exact value depends upon the balance of viscous to metabolic power dissipation in the tree being examined[66]. Further work of Kassab *et. al.* resulted in the formation of four structure-function scaling relationships, each relating various physical properties of the arterial tree (volume, length, diameter and flow). The predicted scaling exponents were validated by linear regression for various arterial trees.

West *et al.*[141] derived allometric quarter power scaling laws for mammalian transport networks based upon the minimisation of power and a fixed size of terminal arterioles.

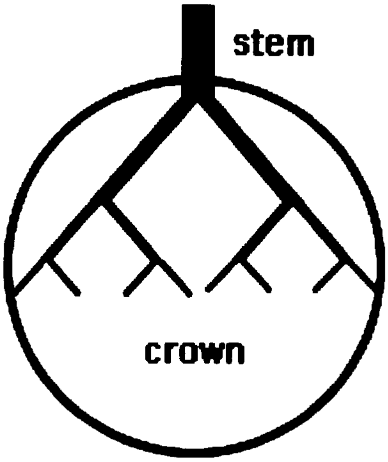

Figure 2.7: The stem crown formalism used in Kassab *et. al.*[66]. The properties of the crown, such as volume, length, flow, are calculated as totals, and related to the properties of the stem via power laws.

Their model incorporated pulsatile flow and showed that area preservation was important near the aorta, which would support a bifurcation exponent of close to 2.0 in that area of the vasculature. The model was verified by comparing the predicted scaling exponents with experimentally obtained values for numerous physiological parameters (e.g. aortal radius, tracheal radius, cardiac frequency, blood volume etc.). Models such as the ones outlined provide good tests for any computational method aimed at generating arterial trees: generate an arterial tree, measure the exponents, compare with the physiological obtained values. However they also provide valuable insight into the underlying mechanism behind this structure. For both models, the key assumption was the minimisation of energy expenditure, in the first case by the application of Murrays law, and in the second case by using an extention of it that includes pulsatile flow. It would seem key then, if any large scale vasculature is to be generated computationally, that the minimisation of energy be the guiding function. Murrays law itself however explains nothing of the large scale structure of arterial trees: it takes scaling arguments, new assumptions and large quantities of algebra to get there. Instead, the law simply relates one radii to two others, at a single bifurcation, disconnected from the whole. In orde to investigate the effect that energy minimisation has on a tree comprised of thousands of bifurcations, an efficient computational algorithm must be developed.

2.4 Previous Methods for Arterial Tree Generation

Various methods for the computer aided construction of arterial trees have been tried in the past. The most pervasive and relevant to this thesis is constrained constructive optimisation or CCO, which uses local optimisation techniques to generate arterial trees based on Murrays principle[118]. The other techniques fall broadly into two categories: statistical and fractal. Statistical models use large morphological databases to reconstruct arterial trees which have realistic physical properties[61]. Fractal models are basic, frequently one dimensional models which are used to investigate network effects and fractal properties of arterial trees. Throughout the broad and varied history of arterial tree modelling no published attempt has been made to investigate the effect of global optimisation on arterial tree structure. CCO would be by far the closest match if global optimisation were the search criteria, however its local optimsation falls short, and computational difficulties often preclude it from investigating realistic tissue geometries. In this section we will examine the CCO algorithm in detail as well as outline some of the morphological and fractal models used previously.

2.4.1 Constrained Constructive Optimisation

Constrained constructive optimisation is an iterative technique which aims to produce morphologically accurate arterial trees. The algorithm successively adds terminal points and optimises their connection to the existing arterial tree. In this way trees consisting of 1000's of bifurcations can be generated. In the following we detail the procedure and characterise its strengths and weaknesses.

Initially a root node is located along the edge of the perfusion volume, being the area of tissue to be supplied, and then a random position inside the volume is picked to be the second node. This node is then connected to the root node and the radius of the connective segment is scaled so that a predetermined flow and pressure are achieved at the second node. The predetermined flow is calculated as the physiological value of the flow through the root node divided by the required number of end nodes. After this first procedure, the algorithm can be fully generalised to the case where a new end node is to be connected between two existing nodes. The generation of a new end node begins by choosing a point inside the perfusion volume. This is done by generating a random point and then checking to see whether this point falls within a certain threshold distance of the current nodes and segments. If the distance is less than this threshold value then the point is rejected and a new point is chosen. If this process of rejection occurs more than a specified number of times, the threshold distance is reduced and the process is repeated. This method ensures that areas of tissue which are lacking blood supply are perfused more preferably, in analogy to angiogenesis in tissue (See Fig. 2.8). Once a position inside the tissue has been chosen, two nodes are added to the tree. The first node is the end node itself (x_{new}), the second is the node which connects the end node to the tree (x_{conn}). The process of addition proceeds first with the determination of the twenty nearest neighbours of x_{new}. When this set is found, connections are made between each and x_{new} by positioning x_{conn} half way between the chosen nearest neighbour and its parent. There are thus four nodes involved in the addition of a new end node to the tree: x_{conn}, x_{new}, and the nearest neighbour to x_{new} which we call x_{NN} and its parent x_{par}. For each nearest neighbour the position of x_{conn} is changed so that the value of a target function is minimised. The nearest neighbour with the lowest value of the target function is then chosen as the permanent connection for x_{new}. This process is then repeated until the required number of terminal nodes is achieved[118].

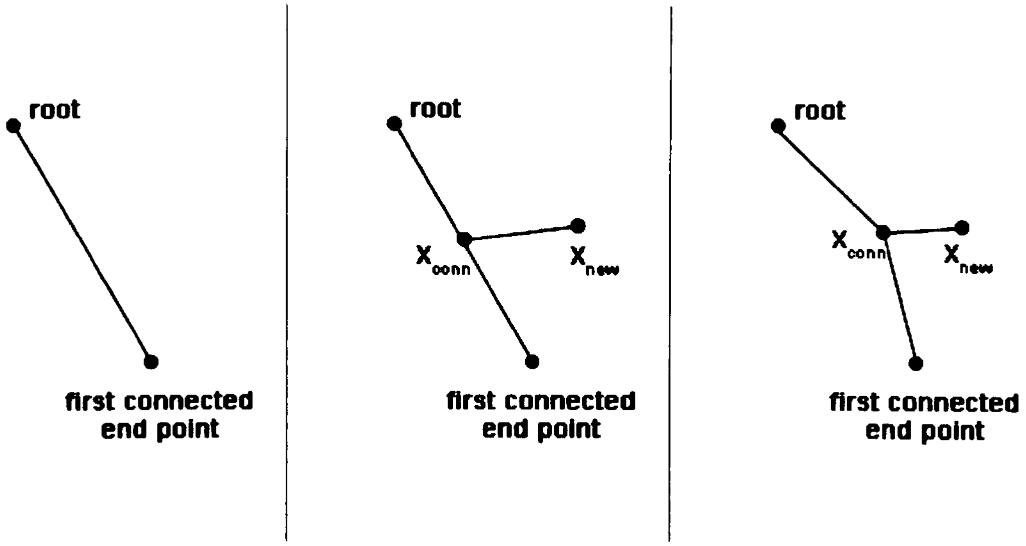

Figure 2.8: CCO iteratively adds leaf nodes to a tree and optimises the connection between these nodes and the existing tree. In the first (left) panel a new leaf node has been added to the tree. In the second (middle) the connection has been made to the existing tree read for optimisation. The final panel shows the final tree, having had a new connection optimised. In a tree consisting of more than a single segment, multiple new connections are tried and the most optimal is selected.

The target function is of the general form

$$P_{cost} = \Sigma_i r_i^{\alpha} l_i^{\beta} \tag{2.6}$$

Where i refers to an individual node and the sum is over the entire tree. Different values of the exponent α and β represent minimisation with respect to different physical parameters. For instance $\alpha = 1$, $\beta = 1$ represents a cost function proportional to the surface area, and so a CCO procedure using those values would produce a tree optimised to minimise the surface area. The standard cost function used throughout the literature is one which minimises the intravascular volume, so that $\alpha = 2$ and $\beta = 1$. In addition to optimising the volume, CCO also enforces Murray's law at bifurcations, so that Eq. 2.1 holds throughout the entire tree. These two optimisation conditions are sufficient to produce physiologically realistic tree structures.

Boundary conditions are necessary to set the physiological parameters of the tree. In general, the terminal flow of each node is specified as some fraction of the inlet at the root node, most usually as Q_{perf}/N_{term}, where Q_{perf} is the inlet flow at the root node and N_{term} is the number of end nodes. The pressure in the root and end nodes are set to physiologically reasonable values, and the bifurcation exponent γ is set.

Maintaining the physiological boundary conditions is achieved by successive scaling of segment diameters. The initial segment comprising of the root node and the first end node is scaled trivially to maintain the pressure and flow conditions in the distal and proximal regions. The addition of a new end node requires that the flow splitting at the bifurcation, which is a result of the pressure drop over the new segment, be readjusted to meet the terminal flow requirements. Previous to CCO most attempts to model vascular systems were statistical and ignored topological and morphological effects[14, 120, 127].

Schreiner et al.[118] performed a morphometric comparison of their CCO generated tree with the corrosion cast results of Zamir and Chee[151], finding good agreement on the diameters of vessels both at the distal and root ends. However the model underestimated the diameters of mid-level (4 - 7 bifurcations from root) arterioles, most likely as a result of small side branching arterioles being burned off the corrosion casts of Zamir and Chee. In addition pressure profile and perfusion heterogeneity comparisons are performed, providing good agreement with experimental data. Schreiner *et al* performed CCO simulations for varying bifurcation exponents and target functions[100]. Trees were generated using the same seed for the random number generator but with different parameters, so that the effect of random variations in structure were avoided. They found that target functions depending on greater exponents of the radius of arterioles tend to decrease the overall bee-line distance from the root to the end nodes. Lowering the bifurcation exponent was found to increase the rate at which the cross sectional area decreases across the tree, but did not affect the trees topological structure.

Karch *et al.* [64] generalized the CCO method to grow vascular trees within convex three-dimensional boundary conditions. As with Schreiner *et al.* a morphometric comparison with the results of Zamir and Chee[151] was performed, with bifurcation levels (4 - 7) again being understimated. In addition, Karch *et al.* improved the CCO method to include variations in end node pressure and perfusion, removing previous limitations. Karch *et al.* [65] also improved the CCO method by including a time dependent probability function in the selection of new end node points. This allowed for a sequence of domains of vascular growth to be defined within the perfusion volume. Kretowski *et al.*[78] developed an algorithm for CCO which ignores the change in global optimisation caused by optimisation of a single additional bifurcation, giving significant speed improvements over standard CCO at the expense of global optimisation. Schreiner et al have demonstrated the use of potential functions in forming 3D boundary surfaces for use in CCO[119], allowing for the modelling of concave tissues. The rigid boundary conditions supplied by finite element representations are often undifferentiable and suitable only for robust optimisations schemes which CCO is not. They showed that finite sums of point potentials give boundary conditions which are differentiable and also able to represent tissue surfaces within organs. Additional constraints are added to the CCO model, such that the first connection to the new node runs along an isosurface of the potential function. Results are compared with the experiments of Zamir[151] and found to provide good agreement. Bui *et al* performed CCO modelling for the cerebral vacsulature using a sign distance level function to provide weighting for the target function(e.g. Total tree volume)[16], extending the work of Schreiner *et al*[119]. This allowed more realistic vascular morphology, where larger arteries exist on the surface of brain tissue rather than penetrating inside. The dependence of diameter, length and number of segment elements upon the bifurcation order number was found to follow the same semi-logarithmic relationship reported by Lapi et al[83], but it was concluded that the variations of branch size, length and number were larger for successive bifurcation order than in rats. In all CCO methods the bifurcation exponent is calculated a priori and entered into the model, and with the exception of Karch *et al.*[64] all reviewed methods pre-set the required end node flow to physiological reasonable values.

That initial decisions of growth drastically affect the resulting CCO generated tree is both a feature and a possible criticism. In anatomical terms, this historical functioning perhaps shows analogue in the process of angiogenesis, where newly grown arteries will not move drastically or alter much more than their widths in the face of increased flow. In optimality terms, a CCO tree is locked in a local optimum of its own geometry, where the growth itself specifies its own optimum, so that the global optimum of design is never approached; when the desire is to search, or at least to presume that nature attempts to search, for a global optimum, it would seem counter productive to exclude such a solution from the search space. However, as was previously mentioned, this is perhaps a reasonable assumption given that arterial trees in humans do not look exactly alike, but still it is not certain whether the departure of individual design, the uncertainty of biological scatter, represents a deviation to a local optimum, arising from early decisions in growth, or the deviation from a global optimum, caused by the imperfection of nature's search algorithm. In addition, given the heretibility of coronary arterial structures, and the overall similarity in design of various organ arterial trees, it would seem problematic for the CCO technique that the structure of large arteries is often highly variable between simulations. That is that the variability resulting from local optimisation is at odds with the observation that the structure of organ specific vasculature, particularly in the larger arteries, is relatively consistent over a population. This implies that either the optimisation criteria used in CCO are incorrect, or that the local optimisation procedure itself is at fault. If the former were the case then it would be necessary to develop computationally efficient fluid dynamics procedures to more accurately calculate flows, as well as techniques for representing curved arteries, in order that error in the first order approximations and geometry could be ruled out as the cause. If the latter were the case then what is required is a new technique capable of generating the global energy minimum for complex tissue geometries.

The primary difficulty arising from non-convex boundary conditions in CCO simulations is the Newton-Rhapson method used to find the minimum. If two nodes which are to be joined have a section of non-occupiable space between them (say, for instance, the ventricle of a heart), then this must somehow be included in the calculations performed as one of the nodes is moved to find its optimal position. More concisely, the optimisation search must be able to recognise and exclude invalid configurations. In a convex space this is done automatically, since no two points have non-occupiable space between them, but in a more realistic geometry, e.g the heart where the internal volume is a “forbidden” region, this is not the case. In order to allow the Newton-Rhapson method to accurately determine whether arteries have entered excluded zones, the virtual substrate being used must be expressed mathematically. This is because there must be some sort of smooth, directional gradient guiding the optimisation routine to the valid solutions. A simple yes no check would not do, as it it would not inform the algorithm which “direction” to head next. To achieve such a mathematical expression for generic organs is difficult, but not impossible. Schreiner et al[119] constructed their tissue substrate by using point sources to build a potential field which represented the geometry. The process is similar to the method of images in electrostatics, where problems are mapped to configurations of point charges in order to make them simpler to solve. In this case, the equipotential lines are created so that they follow the surface of whichever geometry is to be modelled. This process however creates an additional problem in that the optimisation procedure often attempts to create links which penetrate deep into the tissue only to emerge again near the surface, which is completely unphysiological. In order to mitigate this, the potential surfaces inside the tissue divide it into layers, with a bifurcation point being required to lie between the layers of it's parent and daughter nodes. The exact process is more comlicated than this, but this is the general approach. Clearly, the inclusion of arbitrary tissue domains requires a large expansion of the model, including numerous complexities some of which some are entirely organ specific - the algorithm must be adapted subsequently if new organs are to be modelled. The ideal situation would be to have an entirely generic algorithm, one which is founded upon a set of sensible optimisation criteria which emcompass the functions of an arterial tree. We will see in later chapters how this can be achieved, but for now it is enough to note that a locally optimal, iterative procedure is not the best approach.

2.4.2 Statistical And Fractal Models

Statistical techniques form a separate class of models to those involving optimisation of physiological parameters. In order for them to succeed, large morphological databases must be created for the tissue, and detailed imaging data must exist of the larger arteries. This is a severe restriction given the lack of availability of human organ morphological databases. However, once these morphological databases are constructed, they prove to be very powerful for producing accurate arterial trees for the purposes of computational modelling. Being generated from explicitly from experimental data however, their predictive and explanatory powers are limited.

The largest scale statistical model was produced by Kaimovitz *et al.*, who generated a large scale reconstruction of the porcine coronary vasculature[61] based upon morphological data of Kassab[67–69]. The vascular tree was grown in three subsections corresponding to outer, middle and inner layers of the heart wall. Initially tree substructures were grown stochastically based upon the morphological data without being given geometric structures, that is the substructures had vessel order and length, but no 3D geometric structure. Larger networks are then formed by joining compatible (in terms of vessel order) sub structures. Diameters are then assigned based upon statistical matrices formed from the morphological data. Geometric structure is given to the network by use of Simulated Annealing, which is used to optimise the bifurcation angles. Finally the 3 separate layers are transformed to a spheroid surface by means of a least squares change in the lengths and angular properties. The resultant tree includes the vascular system down to the capillary network and has fairly good agreement with experimental data.

Fractal models attempt to measure physiological properties from symbol models characterised by fractal dimension. Diffusion Limited Aggregation (DLA) has been used to model the fractal structure of arterial trees[88], however this method ignores physiological constraints and does not fall under the category of global or local optimisation. The technique is based upon standard DLA, where a seed particle is placed in the centre of the problem space. A particle is then created at the boundary and allowed to diffuse until it comes within a specified distance d_s of the seed, at which point it attaches. The newly attached particle and the seed then become possible attachment sites for other particles allowed to diffuse from the boundary. This process is repeated until a predetermined amount of particles have been attached. Flows in the tree were calculated by assuming that each bifurcation resulted in an equal division. The fractal dimension and frequency distribution of flow values were measured, however there was no comparison to morphological data. While interesting, this technique and other fractal or diffusion based models do not in general produce viable trees in terms of geometric properties.

2.4.3 Global Optimisation Techniques

The global optimisation techniques listed in this sectional are global in the sense that they operate in some way on the entire tree. In contrast to CCO, which optimises a single bifurcation never to revisit it, these techniques perform an optimisation step which involves several or all bifurcations in the tree. However, due to the details of the optimisation performed, neither of the techniques finds a global minimum. The first technique begins with segmented image data, and uses target function optimisation to improve the segmentation.

While this technique is not strictly a method for generating arterial trees, it does attempt to use the concept of optimisation as applied to vascular systems. The second technique listed in this section uses a pseudo global update on top of a CCO algorithm in an attempt to improve consistency in the placement of the larger arteries. The resulting trees do show some improvement in this regard, however they are still not guaranteed to reach the global minimum, and the algorithm still inherits all of the issues associated with CCO.

Bruyinckx *et al.* used Ant Colony Optimisation (ACO) to segment arterial phase CT images of the liver portal vein[15]. The method consists of 3 phases: first, a set of bifurcation points are located within the image. Afterwards, connections between bifurcation points are selected based upon a maximum radius constraint. Finally, the ACO optimisation procedure finds the combinations of connections which minimise an energy function. The energy function itself is built from two separate contributions. The first is an "image" term, which is a measure of the probabilty of the CT image given the current segmentation. The second term is physiological and is built from three separate properties: volume, Murray's radius mismatch and perfusion. The volume term simply optimised for trees with minimum volume. The radius mismatch is a measure of the difference between the calculated optimum radius based on Murray's law, and the vessels radius in the current segmentation. Finally the perfusion constraint is constructed by distributing artificial terminal sites through the imaged tissue, and requiring that all of these sites be with the range d_max of a "real" node in the segmented tree. The authors however elected to contain the artifical terminal sites within the region of interest by placing them at the location of candidate bifurcations. The choice to use Murray's law is also questionable. While there is good evidence to support a radius-flow relationship, as has been shown its value is rarely 3.0, especially in the larger arteries as were considered in this paper.

Georg *et al.*[41] used a combination of global and local optimisation to create realistic vascular trees. The local optimisation was achieved by use of CCO, however as CCO has history it was found that early decisions in the model growth drastically affect the finished tree. The history effect is combated by a global procedure which removes all bifurcations below a certain order and then connects all end nodes to their nearest node on the pruned tree. After this a local optimsation procedure splits and merges nodes which are suboptimal. Once a new optimum has been found the pruning procedure is repeated up to a level lower than previously, where the level is determined by the strahler order of a bifurcation. It must be noted however that this is not true global optimisation in the sense traditionally thought, where the global energy minimum is gauranteed to be found. The process periodically uses a "global" operation which can effect all nodes, in an effort to remove the history effect caused by the sequential addition of arteries in CCO. This means the algorithm is technically not performing global optimisation because ergodicity is not guaranteed. The extra "global" operation simply shifts the subspace of allowable solutions, but does not guarantee that the entire solution space is accessible.

Chapter 3

Method and Algorithm

3.1 Introduction

As we saw in the previous chapter, the most widespread optimisation algorithm for the generation of arterial trees, constrainted constructive optimisation (CCO), proves inadquate on a number of fronts. First and most important is the lack of a global optimisation schedule, which results in unphysiological variation of the larger artery structure. Second is the computational and analytic complexity of the methods required to adapt the algorithm to arbitrary tissue geometries, which themselves are *adhoc* and have no natural justification other than producing superficially realistic results. This last point may seem an odd one to make, but it is important if we are to learn anything from the algorithm. If it is tailor made to reproduce experimental results then we can extract no information regarding the cause of the structures we see. In order to find what the rules of arterial tree construction are inside a human body, we must first construct those rules and then design an algorithm which follows them: if the resulting trees are physiological realistic then we have a strong argument for the correctness of the rules we choose. This chapter is divided into three sections. In the first we detail the arguments for the selection of the optimisation criteria for a new method. In the second we outline various global optimisation procedures capable of generating optimal

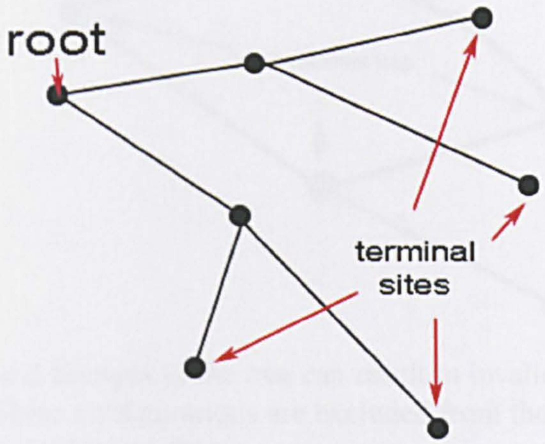

Figure 3.1: Schematic showing the categories of nodes present within the arterial tree model. The root node is the input for both radii and fluid dynamical properties of the tree. Terminal nodes represent the exit point of the tree. All other nodes represent bifurcations.

trees and justify our choice of Simulated Annealing. In the final section we detail the exact implementation used to generate the arterial trees presented in Chapters 4 and 5.

3.2 Arterial Tree Properties

The keystone of any computational model of arterial trees is the representation of the tree. To proceed we must first have an understanding of how exactly we can store an arterial tree, a compex 3 dimensional structure containing millions of tubes, inside a computer. Since the vast majority of bifurcations are binary, we can borrow the binary tree data structure from computer science. Traditionally used to store sorted data to allow faster searching, the binary tree is represented by a collection of nodes which, baring the root and terminal nodes each have 3 connections. The root node is the input, and has two connections which are its two daughters. Terminal nodes have only a single connection to their parent, and are unsuprisingly the point at which a path from the root terminates (See Fig 3.1. For our purposes the root node will be the start of the arterial tree we are modelling. It will in most

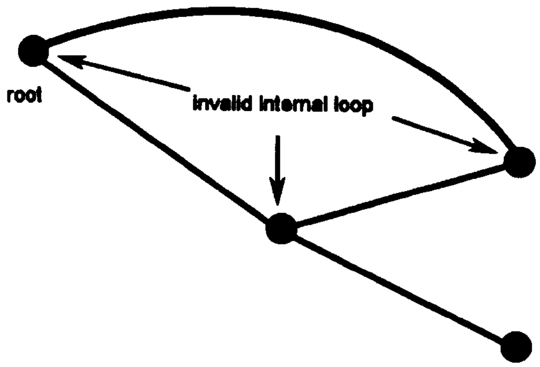

Figure 3.2: Topological changes in the tree can result in invalid configurations which contain internal loops. These configurations are excluded from the solution space by avoiding modifications which could create them.

cases be the largest artery supplying blood to the particular organ of interest. The terminal nodes are the points beyond which we can not model due to computational complexity and computational speed constraints. Each bifurcation of the tree is given a specific location in 3D space and a set of connections which encode its topological configuration. In this way the geometric and topological structure of the entire tree is specified. Any modifications to the tree will involve either swapping some of these connections or moving the 3D location of one of the bifurcations. We will only ever consider modifications which result in valid tree configurations (no internal loops. See Fig 3.2).

3.2.1 Blood Supply

We have noted previously that the main purpose of the arterial system in man is to supply oxygen and nutrient to cells. This requires that the arterial tree terminates with capillaries, small thin walled vessels capable of allowing diffusion to occur. In addition, the blood should be homogenously distributed throughout the tissue[142], meaning that terminal sites are positioned such that the tissue supplied by them is maximised. In CCO, these conditions are achieved by fixing the terminal flow and pressure of the tree and by randomly distributing the terminal sites inside the tissue. Since the terminal sites are never as small as capillaries

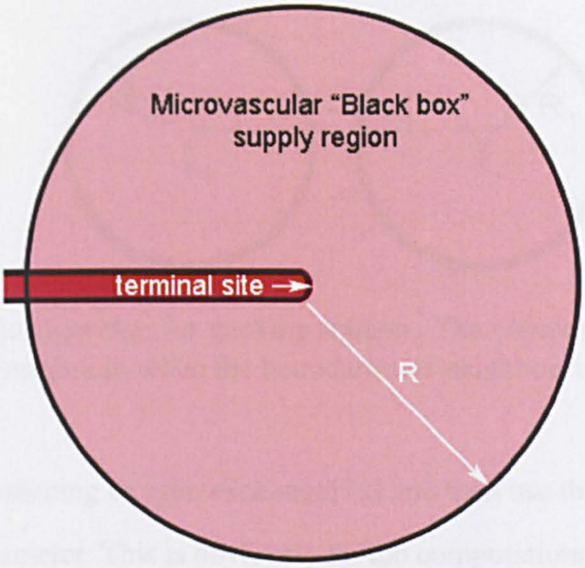

Figure 3.3: Due to the early termination of the simulated trees, it is necessary to provide an approximation for the distal microvasculature. The microvascular black box serves this purpose by approximating the missing vasculature as a sphere of blood supply. As the number of black boxes increases the simulation accuracy increases, up to the limit of the smallest arterioles

(typically they are a few hundred micrometers, whereas capillaries are of the order of tens of micrometers), they are considered to be microcirculatory "black boxes" where the details of the microvasculature have been neglected entirerly (See Fig. 3.3). This approach is not perfect, ideally you would model the tree at all length scales, but it without this assumption the the computational power required to optimise the tree would be prohibitive. We sought to improve this approach on the grounds that it assumes each microvascular black box is of the same general size and maintains the same blood flow, in turn assuming that the tissue to be modelled is completely homogenous. This means that organs consisting of two or more tissue types (e.g the brain) or tissues which have heterogenous blood supply would be impossible to model.

There are many different ways to achieve this improvement each with varying levels of computational complexity and corresponding levels of accuracy. The most complex and accurate method would be to generate arterial trees down to the capillary level, solve dif-

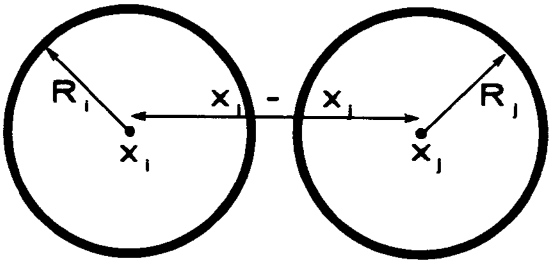

Figure 3.4: A simple algorithm for packing spheres. The objective function is given in Eq. 3.1, and reaches its minimum when the boundaries of neighbouring spheres touch.

fusion equations governing oxygen exchange[72] and then use the oxygen concentration as an optimisation parameter. This is obviously far too computationally complex to be feasible given current hardware. A more conservative approach would be to use a sphere packing algorithm. Assuming there are n microvascular black boxes, each spherical in shape, we can construct a value P which measures how well the spheres are packed together (Fig. 3.4):

$$P = \sum_{j=0}^{n} \sum_{i=j+1}^{n} |(|x_i - x_j|) - (R_i + R_j)| \tag{3.1}$$

The sums give contributions from all combinations of spheres i and j. $x_i - x_j$ is the distance between the centres of spheres i and j, and R_i is the radius of sphere i. This algorithm would be potentially adequate for a precalculation procedure, where the terminal sites are all decided before the optimisation of the actual arterial tree. However if the distribution of terminal sites starts to depend in some way on the structure and geometry of the optimised tree, then it will become prohibitively computationally expensive to recalculate it each time we need a new configuration. More importantly, this algorithm would provide no quantitive measure of whether a section of tissue is under or over supplied with blood. This means that if for some reason it was desireable to prioritise over supply rather than under supply, there would be no way to implement it. This could be resolved, but the algorithm would still require N rather lengthy calculations (or a complicated algorithm) for each update of the end node positions.

If the tissue were voxelised it would be possible to calculate a numeric value for the current level of blood supply in each voxel. Of course, voxels are not the only option, but they are the simplest to implement computationally, and provided their scale is not too coarse they provide more than enough accuracy at tissue boundaries. The voxelised method is to implant spheres (or the closest match in a voxelised space) into the voxelised tissue, so that a grid of values which correspond to the amount of blood delivered to that particular point (see Fig. 3.5b) is created. The process of expanding or moving a sphere then reduces to subtracting the previous contribution from each voxel that sphere influenced, and then adding the contributions to the voxels surrounding the new location. As with the sphere packing outlined previously, this voxelisation procedure allows for the introduction of more complicated supply distributions. It is an obvious approximation that the tissue supplied from the point of termination is a hard sphere centered on that point. The microvasculature at the capillary level is an arcade network that allows for the supply of tissue from various inlets, and so the blood supply cutoff is unlikely to occur sharply. However, at the level of model precision that we are looking to achieve (of the order of 1mm, similar to an MRI data, which will form the tissue geometry) the cutoff would look rather sharp. Still, unlike sphere packing, a more complicated distribution, such as a gaussian centred at the terminal site, could be implemented. However the minimal increase in accuracy resulting from such an improvement would be offset by the increase in computational cost.

The calculation for the total tissue supplied amounts to counting all the voxels in the tissue which are contained within at least one sphere. A measure of the over supply can be achieved by counting the voxels which are contained within more than one sphere, and the under supply by all voxels not contained within any sphere.

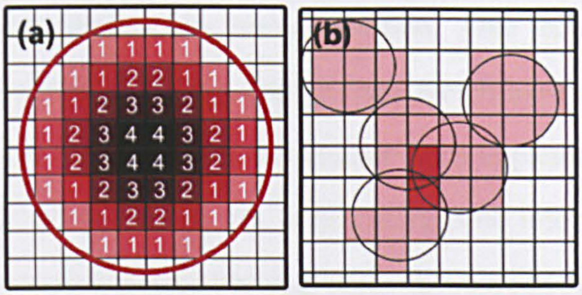

Figure 3.5: a) The distance transform for a circular exclusion zone. Arterial segments which penetrate this zone accrue a numeric cost which can be used in the optimisation procedure to penalize solutions which contain them. b) Voxels of tissues contained within the microvascular black box are considered to be supplied adequately. If more than two spheres overlap, the increased supply is used as a penalty in the optimisation procedure. Unsupplied areas of tissue are also penalized.

3.2.2 Exclusion of Large Arteries

In a flat space, the distance between two points is a straight line: however organs in the human body are rarely flat. For large arteries, there are areas of specific organs which are forbidden, which in the following will be referred to as exclusion zones. An obvious cases is the heart, where no arteries or arterioles penetrate the ventricles. Less obvious is the brain, which has large arteries skirting its surface, running up and down the folds of the grey matter. Grey matter has almost double the blood supply requirements of white matter[38], which may play a role in bringing the larger arteries to the surface. The larger arteries of the heart also run along the surface. This is perhaps due to the strong contraction of the ventricle walls, which would increase the resistance of any large arteries found within it. In an organ such as the kidney however, there are no moving parts and no delicate tissues, and so the larger arteries penetrate and bifurcate within the organ itself.

A method is required to allow for the exclusion of large arteries from arbitrary sections of tissue within the model, if organ specific vasculature is to be modelled effectively. Most optimisation procedures require some sort of "gradient" to follow if they are to function efficiently. An example of one that does not is a purely random search, but this method is far from efficient. Random searches do not take of advantage of the information contained in the surrounding problem space of the current solution. One technique for achieving the desired exclusion, would be to simply disgard trees which have arteries out of place (assuming that a way to identify these trees has already been implemented). This method has a pitfall similar to that of random search, in that there is no information to be gained about exactly how far the solution is from becomg valid - move a node a little bit and you're still given the yes or no answers with no extra value to guide the rest of the search. A more computationally efficient solution would be to construct a cost value which depended in some way on the current distance of the tree to a valid solution. Good candidates for the construction of such a value are the minimum distance between nodes currently occupying forbidden regions and allowed regions of tissue.

We could use a finite element method and extract the surface of the tissue, then using point sources construct a mathematical expression for the exclusion zones in the form of isosurfaces. This is the exact approach which CCO used. However, such an approach is quite complicated, and would increase in complexity if real MRI or CT data were to be used as the basis for the geometry. Instead, we turn again to voxels. The main details of the approach are very similar to that of the point source, in that we will generate a voxelised field of values which denote the distance from the surface, however the generation itself will only require that the surfaces have been segmented from the image. Once this has been done, we make use of a distance map[13]. Each voxel in the space is assigned a value equal to its shortest distance to the surface. The voxels which correspond to areas of tissue which are allowed then have their values set to zero. The values correspond to a penalty, where the larger the value the deeper the voxel lies within the excluded tissue (See Fig. 3.5a). The benefit of this approach is that it allows the optimisation procedure to extract information about which direction to move an artery so that it is no longer in the excluded zone.

We can use this distance map method in two ways. The first is use the location of a single point, the point of bifurcation, as the location of the penalty cost for a segment. This

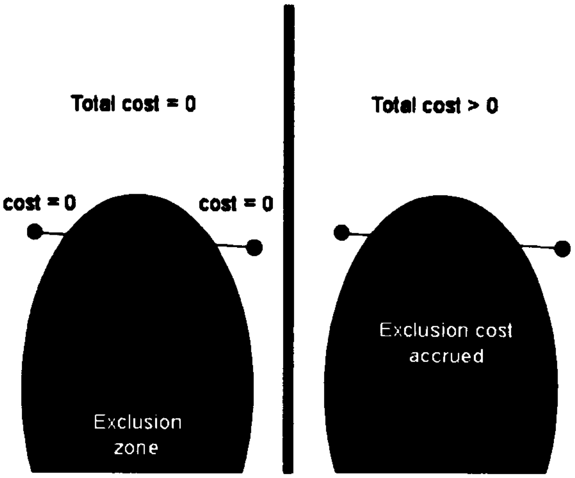

Figure 3.6: The left panel shows the simple algorithm for excluding arteries from tissue. The location of the bifurcation points is used in conjuction withe the distance tranform. In this case, because both bifurcations lay outside of the forbidden region, no cost is accrued and the trial solution is considered valid. On the right is the more complex bresetham algorithm, which acrues cost for the length of the segment which exists inside the exclusion cost. Here the cost would be non-zero due to the connection crossing the forbidden zone, and the trial solution would be penalized.

is computationally very cheap, since it involves only looking at the distance map value at a single point, but suffers from accuracy issues. The second is to follow the path of an entire artery, taking the total of the distance map values at the voxels it intersects. The second method is much more computationally demanding, requiring an implementation of the Bresentham line algorithm[28] (we assume that most arteries will be comparable or smaller to the resolution of the tissue, so that we need not consider it a cylinder). The choice of which to use will depend on the type of tissue. For hollow organs, it is almost certainly necessary to use the line approach, since using only the locations of the bifurcations will results in an artery cutting through the entire ventricle chamber having a zero value when evaluated (See Fig 3.6. With solid organs however, even if the tissue itself is not to be penerated by larger arteries (e.g the brain), the simpler approach may be adequate, provided the radius of curvature is not too large. For solid organs such as the liver or kidney, no exclusion calculation would be required at all.

This method is general in the sense that many different tissue boundaries can be defined within the same organ, each with their own allowed range of radii. In addition, it will work with any conceivable tissue shape.

3.2.3 Energy Optimisation

As was clear in the previous chapters, a key component of arterial tree generation is the optimisation of energy expenditure. Volume calculations are trivial since we assume that all arteries are hollow cylinders. Power calculations however require a choice of approximation. Clearly the gold standard would be to perform full fluid dynamics simulations in order to measure the power expended pumping blood through the tree, however computational expense prohibits this. There are various approximations for pulsatile flow[138] however the vast majority of the bifurcations considered in our model will have very weak pulsatile flow[5]. In addition, the velocities are relatively low. Since we will be performing the fluid dynamic calculations for the entire tree after each modification, they need to be computationally efficient. We assume then that the flow inside the artery is laminar and that a zero dimensional poiseuille flow approximation is sufficient.

To calculate the power dissipated in an artery we first note that the pressure drop over the length of a cylinder supporting a flow of volumetric rate Q, diameter r and length l is:

$$\Delta P = \frac{8\mu l Q}{\pi r^4} \tag{3.2}$$

The power dissipated in this cylinder is $\Delta P Q$. If we can calculate the flows in each artery of the tree, then the total power dissipation can also be calculated.

Given any arbitrary tree configuration, it is necessary to be able to calculate the flows in each artery of the tree. As in all fluid dynamic calculations, a set of boundary conditions are required in order to perform these calculations. There are two choices in this regard: the first is to maintain a constant input pressure and input flow, as well as consant output flows in each terminal site of the tree. This is the approach CCO adopted and it is by far the most computationally efficient. If the output flows are homogenous then the flow in any artery will depend only on the number of terminal sites distal to it. The other approach is to keep only the input flow and pressure fixed. This solution requires a large computational investment, as the flows in each artery will depend upon the distal resistance of its subtree as well as the pressure at its entry point. The calculation is not entirely prohibitive, provided the tree is small, but in comparison to the previous method it will be much slower. The computational approach is to calculate the resitance for each artery as well as the resistance of the subtree distal to it. Then starting from the input, traverse down the tree to each node, calculating the input pressure and flow for its two daughter nodes. This allows the flows to be calculated for the entire tree. Which method to use will depend on whether we wish to model trees with inhomogenous output flows. In our case, since we the radius of the terminal sites is kept constant, the terminal flows are also assumed to be fixed. It is a reasonable assumption given the experimental results supporting a power law relationship between radius and flow. While the flows may be equal in the terminal sites, the blood flow demands on the tissue may not be, which is why the voxelised tissue supply method is still required.

Any optimisation procedure we apply to the tree will necessarily need to modify various degrees of freedom. The most obvious of these is the position of each bifurcation in the tree. Less obvious but still important is the topological configuration. Finally there are the diameters of each artery. Murrays law gives us a guide for how diameters should change at a bifurcation, but the exponent value of 3 does not agree with the experimental data. The power law relationship however is valid for various tissue types[140]. It is then possible to eliminate an entire set of degrees of freedom by imposing Murrays law with a variable exponent. The exact value of this exponent can be either taken from experimental data or be a degree of freedom for the optimisation procedure. This reduces the computational complexity by a large amount, since now the diameter of an artery (much like the flows) is set only by the number of terminal sites distal to it. In Chapter 6 we will calculate the exact optimal values of the bifurcation exponent for a symmetric bifurcating tree.

As we are supplying identical "microcirculatory black boxes" with identical flows, it would seem appropriate to also limit the pressures which are acceptable at the terminal sites. If they are too low then not enough blood will flow, clots will form and the tissue will die. If they are too high then capillaries will burst. To achieve this, it is sufficient to calculate:

$$\sum_{i=0}^{n} |P_i - P_0| \tag{3.3}$$

Where the sum is over all terminal sites, P_i is the pressure in terminal site i and P_0 is the ideal pressure. Choosing the ideal pressure is problematic in that there is a scarcity of pressure data for the arterioles (it is difficult to measure). For the range of diameters considered computationally viable however there is very little pressure drop (10mmHg) so that it is unnecessary to constrain the pressures at all - they will always range within physiological reasonable values.

The three component covered in this section consitute the minimum requirements for the construction of an aterial tree via energy optimisation. In proceeding chapters we will investigate the validity of this claim through comparison of the generated trees with morphological data and images. Now that we have identified the primary criteria and outlined the methods we will use to generate quantatitive values for their evaluation, it remains to find a procedure capable of finding the global minimum. The objective function to be minimised depends upon the positions and topological configuration of the tree, so it will need to be quite general. Topological modification to the tree will necessitate the abillity to cope with discontinous jumps in the search space.

3.3 Optimisation Methods

The previous section outlined the construction of a fitness function which could be used to inform an optimisation routine, but the question remains as to which optimisation procedure to use. The goal of any optimisation method is to minimise some objective function $f(x_i)$ where x_i are the parameters which define a particular solution. While they share this in common, the methods they use to achieve this minimisation vary wildly, and often the types of problems for which they are best suited are just as varied. For instance, a down hill search, which at all times will simply modify the x_i by some amount so that $f(x_i)$ decreases, is perfectly adequate for finding the minimum of a convex function[84]. However if the function has more than one minimum then it is no longer guaranteed to find the global optimum, because the search algorithm can become locally stuck. We will focus our attention in this section on those methods with produce globally optimal solutions for complex search spaces.

There are various deterministic methods capable of finding the global minimum, however the nature of the arterial tree problem precludes their use. For instance, the popular branch and bound method requires the ability to calculate upper and lower bounds of some subset of the search space. This would perhaps be feasible for small trees where the problem space could be divided into subsets based on topology, but for any appreciable number (say, greater than 30 nodes) the number of topological configurations becomes too large for this to work. Other deterministic methods suffer similar pitfalls. We focus then on stochastic and heuristic techniques and present 3 possible approaches.

3.3.1 Multi Solution Algorithms

Multi solution algorithms maintain a population of solutions during the course of optimisation, either in some way picking out the most optimal ones during each iteration or encouraging the population to change towards the most current most optimal solution in the population. They are efficient because large sections of the solution space can be explored during a single iteration, but this efficiency usually pairs with implentation difficulties. This class of methods includes genetic algorithms[53, 81], ant colony[12, 31], particle swarm[8, 71] and the bees algorithm[155].

Ant colony and particle swarm optimisation are both techniques which attempt to influence a population of solutions with information gleaned from the most optimal solutions of that population. While foraging for food, ants lay pheremone trails which are then followed by other ants who also lay pheremone trails. In this way, trails which lead to good food sources are reinforced, and those which lead to dead ends fade away. Shorter trails which lead to food sources are reinforced more quickly than long trails, and in this sense the food foraging is optimised. Computationally an abstract ant entity iteratively constructs a solution, favouring steps which are a shorter distance from its current position (in whichever space the problem is situated) and ones which have higher levels of pheremones. Once a whole solution has been constructed the ant then deposits pheremones if the solution is good (good here is some criteria of fitness).

Particle swarm algorithms work in a similar manner, except that the abstract entities are called particles, and they are given position and velocity inside the solution space. Each particle then represents a solution, and its movements are governed by the locally best known solution, as well as the best solution in the swarm of particles. The primary difficulty with either of these methods are the specifics of the implementation. For particle swarm it is unclear exactly how a velocity through topological space can be constructed, in that it would require a measure of topological "closeness" between trees. For ant colony optimisation the issue lies in the iterative construction of a solution, where it is unclear how pheremone trails should be intepreted if the nodes following them are not of the same topological type (with respect to the number of attached end nodes).

A genetic algorithm is a search heuristic which functions exactly as its name suggests: a large population of trial solutions are compared for fitness and the most optimal are allowed to breed and mutate until a new generation is produced[135]. In order to procede efficiently, the problem space should be adequately encoded in a string of bits, much like a genetic code. This ensure that the process of mating between two solutions produces a valid solution, and allows for the bitwise modification of the solution mimicking the genetic mutation process. In the context of an arterial tree this poses some problems. Geometric data can easily be encoded for any given topological configuration, but the topological configuration itself is more subtle and difficult to formulate in a genetic code format. To avoid the vast majority of breeding between trial solutions resulting in invalid trees, the topological structure must be carefully encoded so that it can be split and joined with minimal chance of failure. If this is not possible, then the efficiency of the genetic algorithm will drop dramatically, and the time taken to reach an optimal, or close to optimal, solution, would become prohibitively large.

3.3.2 Simulated Annealing

While the algorithms discussed in the previous section maintain a large population of candidate solutions, progressing by allowing the most optimal to survive to the next generation, simulated annealing maintains only a single solution. This solution is continuously modified and at each attempt the modification is either accepted or rejected with a certain probability. This process is repeated until a termination condition is reached. The probability of acceptance of a modification is dependent upon a parameter commonly referred to as the "annealing temperature". Simulated annealing is inspired by the physical process of annealing, whereby crystalline materials are cooled quasi-statically to induce higher levels of order in their structure, implying the attainment of lower energy states[1]. Thermal fluctuations at high temperatures allow the system to escape local minima, and the slow reduction of temperature ensures there is adequate time to escape any local minima that may have otherwise have been found if the system was quenched. The temperature of a Simulated annealing algorithm sets the probability of a modification being accepted which increases the cost, with higher temperatures being associated with higher probabilities. At infinite temperature, SA is effectively a random search. The exact expression for calculating the probability of acceptance of a modification is given by the Boltzmann expression:

$$P_{ij} = \exp(\frac{-\Delta C_{ij}}{T}) \tag{3.4}$$

Where P_{ij} and ΔC_{ij} are the probability and change in cost associated with going from state i to j respectively, and T is the temperature. At very high temperatures the probability tends towards 1, meaning that almost all modifications are accepted, even those increasing the total cost of the system. At very low temperatures, any modification increasing the cost of the system will have a probability very close to 0, and and decrease of cost will have a probability equal to 1. The interesting regime occurs when the temperature parameter is between these two extremes, where modifications which increase the cost of the system can still be accepted. If the current solution lies in a local minimum, then these increases of cost allow the simulated annealing search to escape, something which would be impossible with a purely downhill search. Important for the success of the algorithm is the annealing temperature reduction schedule, which dictates how rapidly the temperature declines after each subsequent modification to the trial solution. It is essential that whatever reduction procedure is chosen that it occur slowly, so that the system has adequate time to explore the solution space at any given temperature. In physical terms this is equivalent to allowing the system to reach thermal equilibrium each time the temperature is reduced, or to perform the reduction quasistatically. For most problems an exponential decrease in temperature is sufficient, however there are many different cooling schedules from which to choose[47]. The start and finish temperatures of the algorithm should be chosen so that at it's highest the temperature is much larger than the energy change associated with a typical change, and at it's lowest much lower than the energy associated with a typical change. This ensures that sufficient time is spent in both the randomisation and downhill portions of the optimisation. An annealing temperature which failed to intially exceed the typical cost change would be far more suceptible to reaching local minima, and a temperature which did not decrease to sufficiently small values would mean the system would still be thermalised in some sense.

As with all optimisation techniques some method of evaluation of the fitness of a solution is required. However, once this is attained the algorithm itself becomes refreshing simple:

- Randomly choose a modification
- Accept or decline the modification based on current temperature and Eq. 3.4.
- Reduce the temperature via cooling schedule.
- Repeat previous steps until termination condition.

The key to this algorithm then is to choose the correct set of modications. In order to guarantee that SA will find the globally optimal solution (provided it were given infinite time), a few conditions need to be met. The first is that the set of modifications provided allow for all trial solutions to be reachable (ergodicity). For instance, if the optimisation problem were to find the balance point of a plank of wood, it would be unnaceptable to only have modifications which moved the current best balance point left, since if the global optimum were to the right it would never be found. The second is that detailed balance should be maintained. In simple terms this is the statement that the probability of a modifcation occuring must the same as the probability of its inverse. The core idea is reversibillity, an essential component of any Markov chain process. If the SA algorithm were not reversible, i.e. detailed balance were not maintained, then there would be a net flow of probability towards some section of the solution space, meaning that certain solutions would be favoured simply as a result of the modifications which were chosen. As a result, there is again no guarantee that the optimisation would terminate at the globally optimal solution, even given infinite time.

The power of simulated annealing lies in its simplicity. Once the cost function has been computed, the optimisation procedure is relatively straightforward, meaning complex problems are as simple to optimise as trivial ones. Implementing a genetic algorithm or other multi solution type algorithm such as particle swarm or ant colony would require careful design of the optimisation procedure. In contrast, once a suitable set of candidate moves have been chosen, simulated annealing is algorithmically simple while still offering the guarantee of finding the global minimum. For certain classes of problems it has been shown that genetic algorithms for instance are faster than SA[130], however the increased complexity and the resultant difficulty found if the algorithm requires modification offset this speed increase. With simulated annealing it is possible to add extra boundary constraints and cost function terms without having to modify the optimsation procedure, meaning for biological models improvements can be made to the algorithm without major algorithm modification. In addition, it has been shown that tuning of the cooling schedule can render SA orders of magnitude faster than a genetic algorithm [54]

3.4 Implementation of Simulated Annealing for Vascular Systems

In the previous section various physiological parameters were identified which characterised an optimisation target for arterial trees. In order to show that the optimisation of these quanties leads to the production of morphologically realistic arterial trees, it is necessary to construct from them a numeric value which can be the target of an optimisation algorithm. In this section we detail the construction of these numeric values.

3.4.1 Tissue Supply

At the start of the algorithm, terminal nodes are randomly distributed inside the tissue, with each node having associated with it a sphere of influence for blood supply. The radius of this sphere is calculated using physiological values for the blood demand of the tissue under consideration. The density of myocardium is $\rho = 1.06 \times 10^3$kg m^{-3} [137], and the flow demand is 1.13ml min^{-1}g^{-1} [132] leading to a flow demand per m^3 of heart tissue of $q_{\text{required}} = 1.3 \times 10^{-5}$m^{3}s^{-1}. The total flow into the heart is $Q_0 = 4.16 \times 10^{-6}$m^{3}s^{-1} [48], which can be converted to total flow per node as $Q_N = Q_0/N$, where N is the total number of arterioles (end nodes). The radius of the supply sphere is then calculated via $4\pi R_{\text{supply}}^3/3 = Q_N/q_{\text{required}}$ The sphere can be thought of as a microcirculatory black box [118], where the exact fluid dynamical details of the blood flow have been ignored. Spheres of blood supply associated with end nodes are stored in a voxel map (a voxel is a 3D generalisation of a pixel) of the tissue, where each terminal node adds exactly one to each voxel inside its sphere of supply (Fig 3.5b). The terminal nodes are then allowed to move inside the tissue, where after each move a new voxel supply map is calculated, and the overlap (each voxel supplied by more than 1 sphere, or the dark red voxels in Fig 3.5b) is used as a value in the cost function of the simulated annealing algorithm. In addition, all voxels not being supplied are given a cost, so that as a whole the penalty associated with having both unsupplied and oversupplied voxels is given by:

$$C_s = \sum_{\text{voxels}} s;\, s = \begin{cases} 10 & \text{if } b = 0 \\ (b-1)^2 & \text{otherwise} \end{cases} \tag{3.5}$$

where b is the value of the supply at the voxel (i.e a measure of the total number of spheres contributing to the supply of the voxel) and the sum is performed over all the voxels comprising the tissue. C_s is then a value defining the fitness of the tree in terms of its ability to supply blood, and the penalty for oversupplying voxels forms a sort of self avoidance algorithm, where terminal nodes are encouraged to pack the tissue as densely as possible without overlapping. As the size of the spheres decreases, the accuracy of this approximation improves up until diffusive effects become relevant i.e at the scale of the microvasculature the spherical approximation would no longer be appropriate.

3.4.2 Metabolic Cost of Blood Volume

In order to convert the volume of blood held by the arterial treeto a cost, it must be multiplied by a physiologically reasonable value, m_b, corresponding to the metabolic demand of the same quantity of blood and vascular tissue [86]. Thus the metabolic cost due to the volume of the tree will be given by:

$$C_v = m_b V_{tree} \tag{3.6}$$

where m_b is taken to be 641.3 J s^{-1} m^{-3}[86] and V_{tree} is the volume of the entire tree.

3.4.3 Power cost to pump blood through vessels

To calculate the power needed to pump blood through the entire tree, we must know the pressure and volumetric flows inside each segment (vessel) of the tree, which can be found by first assuming that Poiseuille's law[122], $\Delta P = QR$, is followed inside the segments, where ΔP is the pressure drop over the vessel, and Q is the flow. Due to the application of Murray's law and the assumption that terminal node flows are constant, the procedure for calculating the relevant fluid dynamical quantities is greatly simplified: the only quantity which relies on the geometrical arrangement of the tree is the pressure. In a sense, the segments can be considered to be a connected set of resistors, with the resistance given by:

$$R = \frac{8\mu L}{\pi r^4}, \tag{3.7}$$

where r is the radius of the vessel, L its length and $\mu = 3.6 \times 10^{-3}$Pas the viscosity of blood. The pressures for every node in the tree can then be found recursively. Knowing the pressure, resistance and flow of each segment, the power consumed by each segment i can be easily calculated according to:

$$W_i = Q_i^2 R_i, \tag{3.8}$$

where W_i is the power consumed by segment i. Summing over all segments in the tree, we find the total power required to maintain the proper flow through the tree is given by:

$$C_w = \sum_i^{N_{tot}} W_i. \tag{3.9}$$

3.4.4 Exclusion of Large Vessels from Tissue

In order to calculate the cost associated with a large vessel penetrating a forbidden area of tissue, arteries entering forbidden zones must first be identified. To do this, we define a cutoff radius R_c whereby any vessel exceeding this radius incurs a cost should it penetrate the tissue. For each segment satisfying the radius criteria, a list of voxels which its centre-line penetrates is generated [3] along with a value for the length element of the segment present inside that voxel. A cost is then calculated based upon the value of the distance transform at each of the voxels according to,

$$C_o = \pi r^2 (D_{i,j,k} W_{i,j,k})^6, \tag{3.10}$$

where i, j and k are the x, y and z voxel coordinates taken from the centerline of the segment. D_{ijk} is the value of the distance transform at that voxel coordinate. W_{ijk} is the length of the segment inside the voxel. The sum is performed over all the voxels contained in the list calculated from the centre-line. This cost can then be used in the algorithm as a penalty, which makes moves taking large segments out of the tissue favourable. This method takes into account only the centre line penetration of the artery, but for the voxel resolutions used in the model (1mm) it is entirely appropriate given the low population of larger diameter vessels, where even the largest have radii approximately 1mm in size.

3.4.5 Pressure constraints

In physiologically realistic trees, capiliary networks should receive a constant pressure of blood to function correctly. In order to ensure that a constant pressure P_{term} is found at the terminal nodes, a new cost can be devised. The quantity must be a positive definite function of the sum of the difference between the ideal end node pressure P_{term} and the actual terminal node pressure of node i: P_i. A suitable candidate is then given by:

$$C_p = \sum_{i}^{N_{term}} (P_i - P_{term})^2, \tag{3.11}$$

where the sum is performed over all terminal nodes. In practice, for trees which can be realistically optimised on feasible time scales (i.e of a few thousand nodes), the pressure drop from root to end node is less than 10% of the total pressure drop of a real arterial tree, with the bulk of the pressure drop occuring over smaller arterioles than those considered here. It is then unnecessary to perform this calculation, however when it becomes possible to grow larger trees the pressure at the capillaries will need to be taken into consideration. This will add a significant computational cost.

3.4.6 Total Cost Function

We have now determined a form for all the relevant costs associated with an arbitrary tree configuration supplying arbitrary tissue shapes. We can therefore define a total cost which gives a numeric measure of the fitness of a given tree, defined as:

$$C_T = A_{w,v}(C_w + C_v) + A_o C_o + A_p C_p + A_s C_s \tag{3.12}$$

where A_i are dimensionless constant indicating a weighting value which scales each relevant cost. There is no way to analytically determine what weights to use, and the selection of appropriate weights must found experimentally, however a few basic principles such as the having a very high weight for the blood supply cost and a low weight for the end node pressure cost can guide the process. In this work, we use $A_{w,v} = 1$, $A_p = 0$, $A_s = 1 \times 10^{18}$ and $A_o = 1 \times 10^{13}$. In this way, A_s and A_o force the exclusion of vessels and uniform supply of tissue to act like constraints.

3.4.7 Exploring the tree structure: Translations and node swaps

In order for the simulated annealing algorithm to work, it must have access to a set of moves which allow it to alter the configuration of the tree. It is necessary to find changes that can be made to the topological and geometrical structure of the tree such that all possible solutions, between perfectly symmetric structures and a single trunk vessel can be explored (i.e. the algorithm is ergodic). This is achieved by allowing: (1) repositioning of bifurcations, and (2) swapping the parent vessels of bifurcations between different parts of the tree. The first of these moves is simple: translate a node in space. (Fig 3.7a). For every type of node this move is possible, so that each node is allowed to explore the entire physical space. The second move is performed by swapping the parents of two nodes. (Fig 3.7b). For all nodes but the root node, this move is valid, and performed consecutively it allows all possible tree topologies to be explored. If one of the two nodes is a direct parent of the other (i.e while traversing up the tree to the root node from one of the chosen nodes, the other node is encountered), then the move is rejected as the tree resulting from the move would form

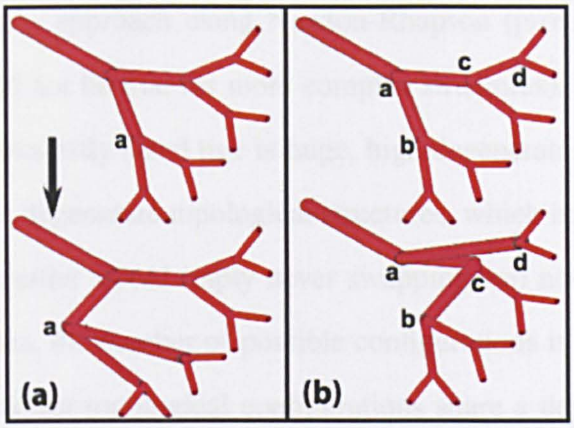

Figure 3.7: The two types of modifications present within the SA algorithm. a) A geometrical move translating the position of a single bifurcation in space. b) A topological move which swap the parent node of a single bifurcation. The combination of these two nodes allows the algorithm to reach any trial solution in the problem space.

a closed loop. With these two modifications, the entire parameter space of the tree can be explored, allowing the algorithm the opportunity to reach a globally optimal solution.

3.5 Convergence and Consistency

The primary purpose of the algorithm is to produce arterial tree configurations which conform to those found in living organisms. As the algorithm itself relies only upon optimisation principles, the close agreement with experimental results implies an evolutionary pressure towards a structure with minimal power consumption. This is itself a far from new concept, however in this paper we have shown that energetic constraints lead not only to a morphometrically realistic tree, but also to the production of major arteries which closely follow the paths of major arteries in living systems.

While it is clear that the algorithm produces both morphometrically and geometrically realistic structures, what is not clear is how close the optimisation procedure gets to the global energy minimum, or indeed whether there is a non-degenerate energy minimum at all. For any given topological configuration there is a single, non-degenerate energy minimum which it is possible to approach using Newton-Rhapson (provided the solution space is convex, which would not be true for more complex structures). In contrast, the toplogical space for any even modestly sized tree is huge, high degenerate and not easily searchable. Even if one excludes degenerate topological structures, which in the case of the swap node procedure outlined earlier would imply never swapping two nodes with the same number of distal terminal sites, the number of possible configurations is still massive. It is entirely possible that two distinct topological configurations share a degenerate energy level, and proving that this is not the case appears difficult.

While it may be that the global energy minimum is highly degenerate, the algorithm itself can still be characterised in terms of reliability and convergence. For reliability, we can perform visual inspections on trees and assess their similarity. It must be noted here that the geometry in which the tree is grown will have a large effect on the consistency of the results. For instance, in the case of a circular section of tissue with an input in the centre, there is a high degree of rotational symmetry. In the case of convergence, we can produce many trees and plot the frequency distribution of their resultant energies, or as in this case the average and variance of the cost as a function of SA steps.

The convergence and consistency tests trees were generated on a 2D plane with the input placed in one corner. The trees consisted of 127 nodes total (64 end nodes) and had a bifurcation exponent of 3.0. The 2D tissue plane was sized at 10cm by 10cm and the root radius at 2.4mm. Each tree was optimised for a given number of simulated annealing steps, with the minimum energy of the SA run being recorded. The average energy reached for a given number of SA steps was then calculated (Fig. 3.8). The results show a clear tend towards lower average energy and standard deviation as the number of SA steps increases. The high variance at the lower numbers of SA steps are typical of a system which has been quenched, i.e high temperature disorder has been locked into the system, which has not had sufficient time to reach equilibrium.

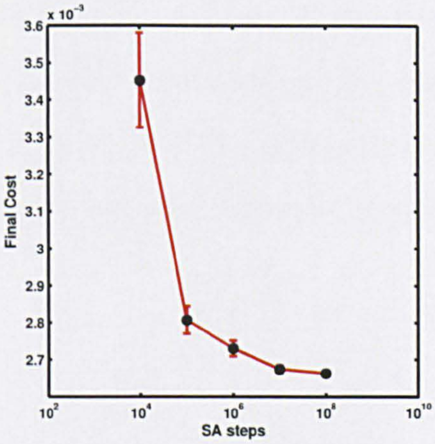

Figure 3.8: Average cost and standard error vs SA steps for a 127 node tree grown in a 2D plane.

For the consistency test we have a produced Fig 3.9, which show trees generated for three different numbers of steps. As would be expected, at low numbers of SA steps the trees are very dissimilar, however as the number of steps is increases the similarity between the overall trees increases dramatically, with a main diagonal artery dominating the structure.

3.6 Summary

In this chapter we have constructed a new algorithm for the optimisation of arterial trees based on physiologically reasonable principles. The cost function for the optimisation is built from numeric values for blood supply, pressure, energy cost and the exclusion of large arteries. The algorithm is capable of generating arterial trees in complex tissue geometries which consist of arbitrary numbers of tissue types, and can also be easily integrated with medical imaging data. This represents a significant step in the field of generative arterial tree modelling.

Simulated annealing was chosen as the optimisation procedure due to its robustness, ability to find the global minimum and its ease of use. The consistence and convergence of the algorithm were then verified on a small sample geometry and were found to be reasonable given the vast size of the problem space. In the following Chapter the algorithm will be used to generate arterial trees on physiologically reasonable geometries and geometries taken from MRI data of living tissue. The results will be compared to morphological data and the geometry of the larger arteries assessed in comparison to imaging studies.

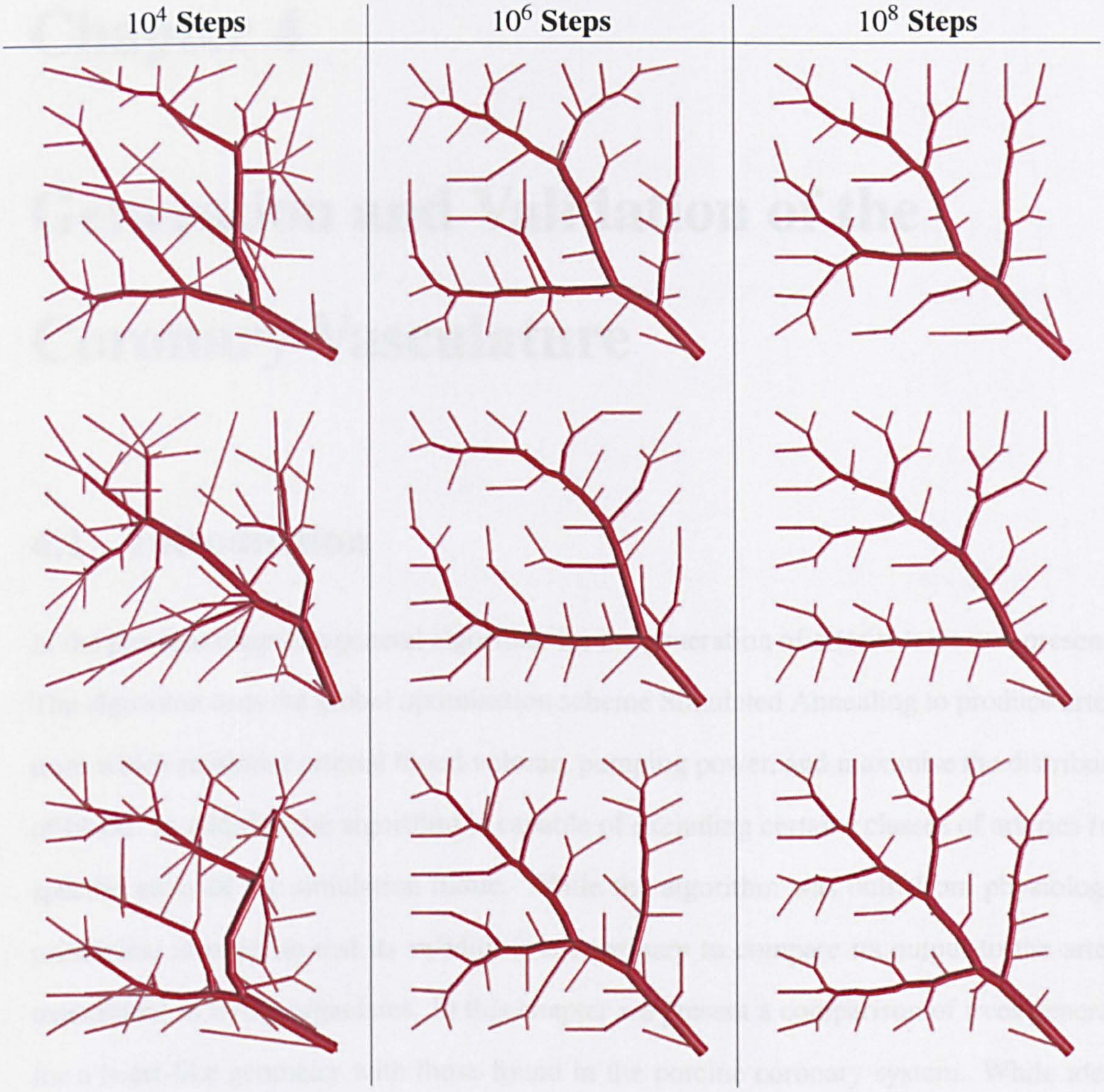

Figure 3.9: Examples of trees grown for various numbers of stepsizes.

Chapter 4

Generation and Validation of the Coronary Vasculature

4.1 Introduction

In the previous chapter a general algorithm for the generation of arterial trees was presented. The algorithm uses the global optimisation scheme Simulated Annealing to produce arterial trees which minimise arterial blood volume, pumping power, and maximise the distribution of blood. In addition the algorithm is capable of excluding certains classes of arteries from specific areas of the simulation tissue. While the algorithm was built from physiological principles, in order to test its validity it is necessary to compare its output to the arterial trees found in living organisms. In this chapter we present a comparison of trees generated for a heart-like geometry with those found in the porcine coronary system. While ideally the comparison would be performed on Human vasculatures, it was found that a lack of extensive morphological databases precluded such an analysis.

We will begin by describing the ellipsoidal heart model which was created to be the geometry input for the SA algorithm. We also describe the diameter defined strahler ordering scheme used in the morphological analysis of the generated trees, and the simulation parameters given as input to the SA algorithm. In the final section we present the morphological comparison and analysis of the various properties of the generated trees.

4.2 Preliminaries

In order to accurately generate the a coronary vasculature the SA algorithm requires a set of input values, such as the tissue geometry, root volumetric flow, root radius etc. This section documents those input parameters which were used in the generation of the results presented in the proceeding section.

4.2.1 Ellipsoidal Heart Model

We require a set of geometric data which accurately capture the geometry of the heart. The large, left ventricle is routinely modelled as a prolate ellipsoid[2, 51, 74, 75, 133], and the right ventricle as a superellipsoid[134] with exponent 2.5. The dimensions of the ellipsoids were chosen to give a left ventricle wall thickness of 90mm[131] and a right ventricle wall thickness of 34mm[89]. The radii of the prolate ellipsoid and super ellipsoid were then scaled, keeping the same ratios, as necessary to provide a total myocardial mass of 218g. The intraventricular septum was created by truncating the right ventricle where ever it penetrated the outer surface of the left ventricle.

The combined right and left ventricle were then truncated in the horizontal plane. In physical terms this remove the right atrium and left atrial appendance from consideration in the model. Given the relatively low blood supply provided to these areas of the heart in comparison to the myocardium this is a reasonable approximation.

While the ellipsoidal model is a good first order approximation, it does fail to account for some of the more subtle geometric properties of the heart. For instance, the path followed by the Anterior Descending Artery (ACA) exists in the indentation formed along the line where the intraventricular septum meets the outer mycardium. This is effectively the boundary where the left and right ventricle meet. This indentation is not captured within the ellipsoidal model and so neither is the possible cost saving from following it. In addition, the heart is a kinematic organ, and the ellipsoid model a static boundary condition. We implicitly assume that any evolutionary pressure tended towards a time averaged configuration of the heart, where approximately equal time is spent both diastole and systole.

4.2.2 Strahler Order

The Strahler (or stream) ordering method was first introduced to classify river systems, but can be applied to any bifurcating system. In standard Strahler ordering, nodes at the end of a tree (in this case the arterioles) are assigned a number 1. At a bifurcation, if two vessels (segments) of the same order meet, then the order of the parent vessel is 1 higher. However, if two vessels of different orders meet, the artery supplying these vessels has the largest order of the two. For example, if two arteries of order 1 meet, then the vessel supplying these arteries has order 2. If an artery of order 3 meets an artery of order 2, then the vessel supplying these arteries has order 3. Therefore, within this scheme, vessels with the lowest order are arterioles. The major vessels have the largest order.

Within a standard Strahler ordering scheme it is possible for arteries of vastly different diameters to be classified within the same order level. For the large arteries within the coronary vasculature, this effect is particularly noticeable due to the tendency for highly asymmetric branching. In order to counteract this effect, a diameter defined Strahler ordering can be introduced. The procedure for determining the diameter defined strahler ordering of arterial segments is iterative, but begins with the arteries being assigned their standard Strahler order value. From this intial ordering a mean and standard deviation of the diameters of segments within strahler order n, D_n and Δ_n, can be calculated. The arteries are then assigned new order numbers based on their diameters such that a segment lies in order n if its diameter D satisfies[55]:

$$\frac{1}{2}((\mathrm{D}_{n-1}+\Delta_{n-1})+(\mathrm{D}_n-\Delta_n)) \leq D < \frac{1}{2}((D_n+\Delta_n)+(\mathrm{D}_{n+1}-\Delta_{n+1})) \qquad (4.1)$$

The newly created set of diameter defined strahler orders are then used to recalculate D_n and Δ_n, which are in turn used to assign new order numbers as before. This process is then repeated until convergence is obtained. For the trees generated by the SA algorithm convergence was assumed when the change in average Diameter and Standard deviation between iterations was less than $1e-5$m.

Within the Strahler ordering scheme it is possible to identify continuous sections of vessels with the same order number. These are refereed to as elements, so a single arterial element may pass through multiple bifurcations. Throughout this article it is the properties of elements which will be calculated for direct comparison with Ref. [66]. We note that due to the early termination of the simulated trees, calculated order numbers are modified so that the root nodes have an order number equivalent to that of the largest arteries of real coronary arterial trees. For example, in the work of Kassab, the largest diameter defined Strahler order number is 11, corresponding to the input artery. For a computer generated tree of only 6000 nodes spanning order numbers 1-6, 5 must be added to each order number so that the orders of the root nodes (largest vessels) match and a direct comparison can be made. This is consistent with assuming that the smallest vessels in the computer generated tree correspond to vessels of order 6. Which is due to the absence of smaller vessels downstream of the smallest arteries in the in-silico model.

4.2.3 Simulation Parameters

In this chapter globally optimised vessels are grown using the previously outlined SA based approach to supply a myocardial substrate, and validated through comparison with morphological data from the porcine arterial tree. We choose to examine the coronary vasculature, since the structure of the large coronary arteries has been found to be similar between individuals[43] and the full arterial tree has been well characterised in porcine models [66]. In modelling the coronary arteries we used the following parameters:

1. A tissue substrate representing an ellipsoidal human heart muscle of mass 218g, constructed based on physiological parameters [134]. The right ventricle was assumed to take the form of a super ellipsoid of exponent 2.5 and the left ventricle was represented by a simple ellipsoid. Truncation of the ellipsoidal substrate was chosen so that the mass of the tissue corresponded to a reasonable physiological value given morphological data for ventricle thickness.

2. Blood flow through each of the terminal segments of the tree was assumed to be constant, with each arteriole supplying an equal volume of tissue and homogeneous perfusion throughout the tissue parenchyma [111]. These assumptions greatly simplify fluid dynamical calculations for estimating the total power needed to pump blood through the tree.

3. The metabolic cost of maintaining a given volume of blood was assumed to be $641.3J\ \mathrm{s}^{-1}$ per metre cubed of blood [86] . For convenience, each arteriole supplies a sphere of tissue with a size calculated by assuming a mean blood flow per unit mass for cardiac muscle of 0.8 ml $\mathrm{min}^{-1}\ \mathrm{g}^{-1}$[73]. The value taken from the literature was chosen such that it lay within the given error, but also conformed reasonably with both the ellipsoidal heart model, input flow and radii.

4. The larger arteries with diameters greater than 0.01mm were constrained to avoid

penetration of the outer layer of heart tissue. This simplification differs slightly from real coronary vasculature, where progressive intrusion of arteries into the myocardium can be observed [128]. However, as the major arteries modelled by our method are far larger than the intra-myocardial vessels, a sharp cut-off is thought to provide a reasonable approximation.

5. The starting positions of the two root arteries were fixed with a total input flow of $4.16^{-6}\,\mathrm{m}^3\,\mathrm{s}^{-1}$[56]. Relative radii of the two inputs to the tree were constrained via $r_1^{2.1} + r_2^{2.1} = [2.1\mathrm{mm}]^{2.1}$ however, the relative sizes of root arteries and division of perfusion territories are determined by the method alone.

6. The branching exponent varies throughout the coronary arterial tree, but for the larger arteries its value remains in the range 1.8 to 2.3. A variable branching exponent would greatly increase the computational cost of the approach, so a compromise value of 2.1 was chosen for the entire tree [59].

4.3 Results

In this section we present the results of a large scale (12000 segments) simulation of the coronary vasculature. The generated tree is compared against both morphological data extracted from porcine hearts as well as geometric data from schematic heart diagrams.

Coronary arterial trees containing increasing total numbers of vessels grown using the SA based method are presented in Fig. 4.1. In real human coronary trees, there are 3 identifiable main coronary arteries (see e.g. the schematic from Ref. [29]): Left Anterior Descending (LAD), Right Cardiac Artery (RCA) and Left Circumflex Artery (LCX). The positions and relative dimensions of these are similar in most humans, with major variations observed in less than 1% of healthy individuals [42]. Trees grown using SA (Fig. 4.1) adhere well to this structure. There is a consistency in the placement of the larger arteries, although

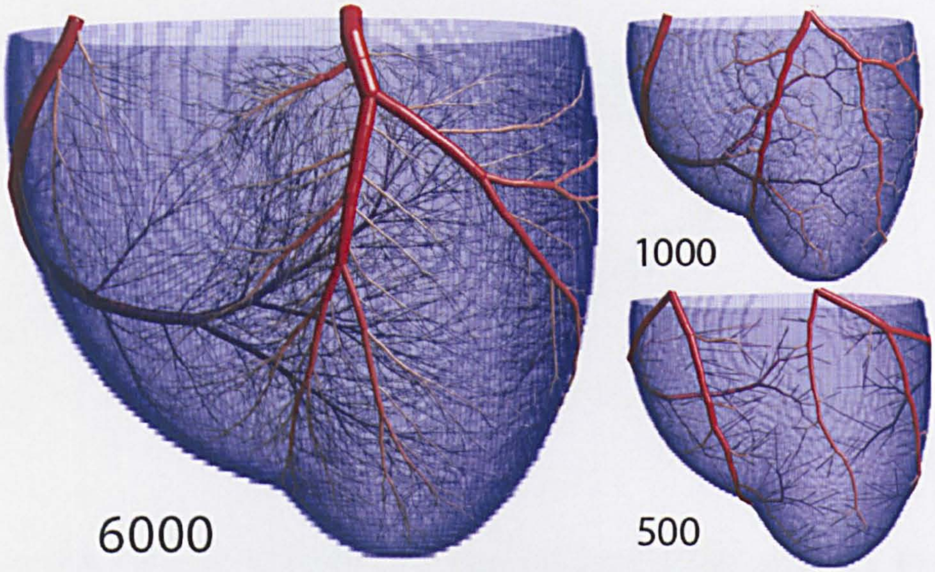

Figure 4.1: Images showing arterial trees grown with the approach detailed here. The number of terminal arterioles is increased from 500 to 6000 (the total number of arterial segments is roughly twice this). There is consistency in the positioning of the larger arteries between the numerical method and the typical arrangement of the major arteries, suggesting that the coronary arteries may be the result of a biological process seeking the global minimum in metabolic demand.

the RCA appears slightly lower, and the right marginal artery appears slightly shorter, in our models. Overall, visual inspection of the arterial structure appears extremely promising.

To provide a quantitative comparison of our trees with anatomical data, the topological characteristics of the computer generated coronary artery trees were extracted and compared to morphological data characterising the pig coronary arteries published by Kassab *et al.* [66] Kassab and colleagues used a combination of corrosion casting and optical sectioning to obtain detailed morphometric data, tabulated using the Strahler (or stream) ordering scheme to denote elements of the tree of varying scale. Within this scheme, the lowest Strahler order numbers correspond to the smallest arterioles and the largest numbers refer to major vessels (for details on Strahler ordering see method). To directly compare arterial diameters, lengths, and branching properties, of our computer-generated arterial tree with real data from pig coronary arteries, averages were obtained over all elements of the same diameter defined Strahler order.

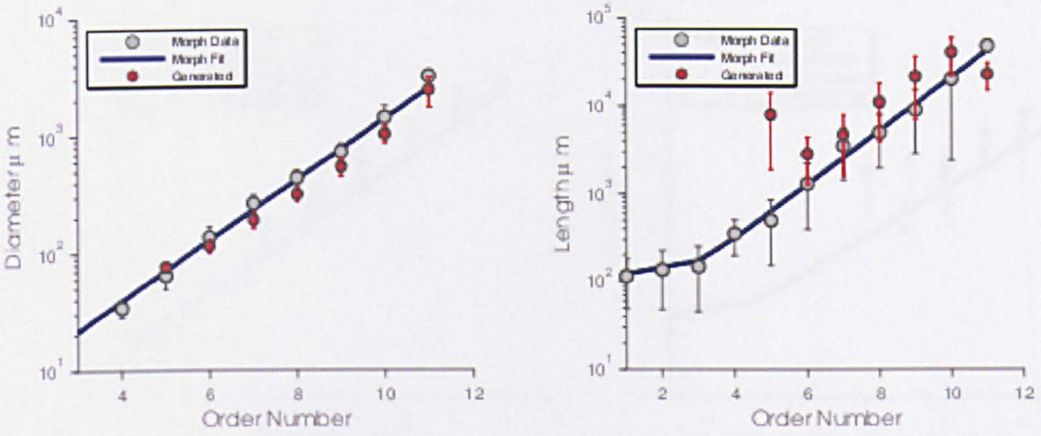

(a) (b)

Figure 4.2: (a) Vessel diameter as a function of order in a tree with 6000 arterioles. Excellent agreement is found for vessels on all length scales. (b) Vessel length as a function of order number. Agreement is excellent for the major vessels (large order). The large variation seen for arterioles (lower order) is a result of early termination. Also shown are the morphological data reproduced from Table 2 of Ref. [69] for easy comparison. (Error bars show standard errors, both axes are logarithmic.)

4.3.1 Diameter and Length

The primary morphological points of comparison are the diameters and lengths of the tree segments, categorised by diameter defined Strahler order. The diameters of the generated tree are loosely controlled by the bifurcation exponent, however due to the diameter defined Strahler ordering scheme and the tendency towards highly asymmetric branching in the larger vessels, there is still a significant amount of freedom in the possible distribution of diameters. For instance, in a perfectly symmetric tree with bifurcation exponent γ, we would expect a strahler order vs logarithmn of the diameter plot to have a gradient of $\frac{\ln 2}{\gamma}$. In an asymmetric tree this gradient can be significantly different, the degree to which depending upon the nature of the asymmetry and the details of the strahler ordering scheme.

The mean vessel diameters are shown as a function of order number, for a tree comprising of 6000 arterioles (12000 vessel segments) in Fig. 4.2(a). Excellent agreement is found

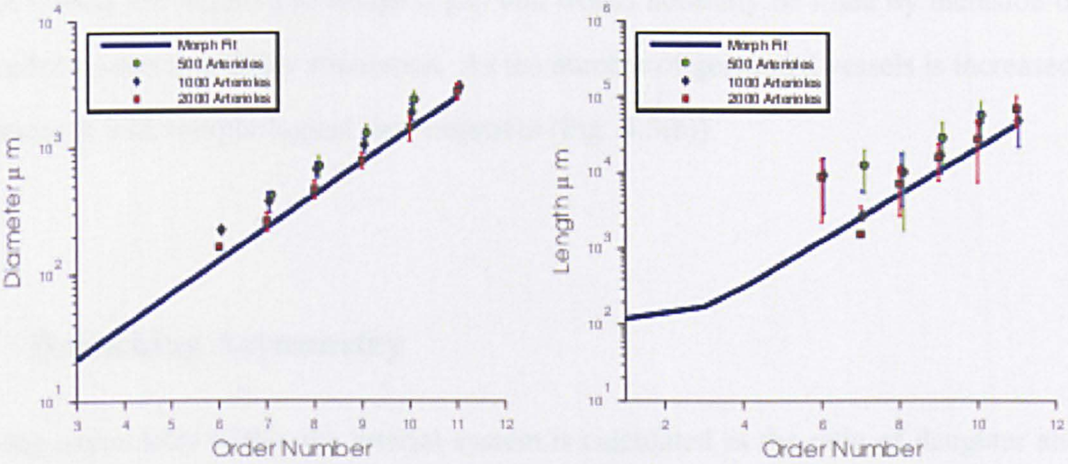

(a) (b)

Figure 4.3: (a) Vessel diameter and (b) length as a function of order in trees with varying numbers of nodes. As the size of the simulated trees increases so does the agreement to the morphological data. Also shown are the morphological data reproduced from Table 2 of Ref. [69] for easy comparison. (Error bars show standard errors, both axes are logarithmic.)

between the trees generated *in-silico* and the morphological data. Only slight deviations from the morphological data can be seen for the smallest vessels (lowest order arteries) in the generated tree. This is likely to be due to the combination of integer order numbers and the condition that terminal sites are of constant radius. The result of this constraint is that the terminal radii will only match the anatomical data for a correct choice of the number of arterioles. Fig 4.3(a) shows the effects on diameter of increasing the number of arterioles from 500 to 2000. Agreement is generally good, regardless of the number of terminal arteries, and there is a clear trend towards matching the experimental data as simulated tree size increases.

Fig 4.2(b) compares average vessel length in the model and porcine morphological data as a function of order number. For the largest arteries (high order numbers) the agreement is excellent. Although the lengths of the smaller arteries (Strahler orders < 7) in the computer generated tree tended to be overestimated, this can be easily explained by the fact that the smallest vessels are required to bridge a gap that would normally be filled by inclusion of lower order vessels in a larger simulation. As the number of generated vessels is increased, the agreement with morphological data improves (Fig. 4.3(b)).

4.3.2 Branching Asymmetry

Branching asymmetry within the arterial system is calculated as the ratio of daughter and parent diameter involved in a bifurcation. In the following we follow the analysis of Kassab *et. al.* and calculate two branching asymmetry parameters A_s and A_l, which refer to the ratio of the smaller and larger daughter segment diameter to the parent respectively. A symmetric branching tree with branching exponent γ has a constant branching asymmetry ($A_s = A_l$) value of $2^{-\frac{1}{\gamma}}$, which for the generated trees with branching exponent 2.1 would be equal to 0.72.

Previously, the best methods available for the computer generation of arterial trees struggled to recreate realistic branching asymmetry. Fig 4.4 shows the ratio of daughter to mother vessel radii for the largest and smallest daughter vessels as a function of order number. For the ratio of the larger daughter vessel, values close to 1 suggest a trunk like morphology. For the smaller daughter vessel, values approaching 0 suggest the same morphology. Where the ratio drops to 0.7, symmetric branching occurs. For Strahler orders corresponding to microvascular arterioles, both the computer generated and true morphology approach 0.7, which is consistent with perfectly symmetric branching where both daughter vessels are of similar size. Agreement with the morphological data from Ref. [59] improves as the size of the computer generated tree increases. This is not the result of any special input parameters or initial conditions. The trees are topologically and spatially randomised before SA optimisation begins, and are allowed to explore the entire parameter space during optimisation. The observed asymmetry is purely the result of a balance between pumping power

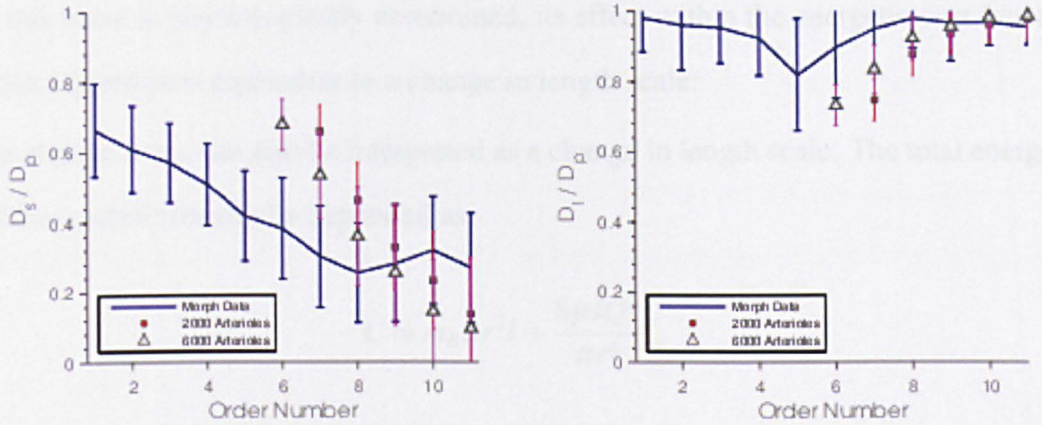

(a) (b)

Figure 4.4: The ratio of daughter vessel diameters (D_s and D_l are the diameters of the smallest and largest daughter vessels respectively) to diameters of parent segments, D_p as a function of order number, showing how the tree tends towards more symmetric branching at lower orders. Agreement with morphological data reproduced from tables in the online supplement of Ref. [59] is good, if the early termination of the generated trees is taken into account, with the trend towards the morphological data as the tree size increases. Both graphs demonstrate that there are large trunks at high orders with the largest daughter vessel (panel (b)) of similar size to the parent vessel and another side artery which is much smaller (panel (a)). At smaller orders, the ratio becomes similar showing that the branchings of the smaller arteries are near symmetric. Realistic branching asymmetries are a clear advantage over other methods of generating arterial trees *in-silico*.

and metabolic maintenance cost, and is a major improvement in predicting the trunk-like structure of major vessels.

4.3.3 Metabolic Cost

The metabolic cost of blood m_b gives the energy cost per unit time of a volume of blood. While this value is physiologically determined, its effect within the energetic cost function of the SA algorithm is equivalent to a change in length scale:

The change in m_b can also be interpreted as a change in length scale. The total energetic cost of the arterial tree can be expressed as:

$$C = m_b \pi r^2 l + \frac{8\mu l Q^2}{\pi r^4}$$

We can make the following transformation: $r \rightarrow r' = Ar$, $l \rightarrow l' = Al$. So that the cost function itself is transformed into:

$$C = A^3 m_b \pi r^2 l + \frac{8\mu A l Q^2}{A^4 \pi r^4}$$

The cost function maintains the same form but acquires a multiplicative factor which affects all terms. This factor can then be absorbed into the cost itself without affecting the location of the energetic minimum:

$$C' = A^6 m_b \pi r^2 l + \frac{8\mu l Q^2}{\pi r^4}$$

A new value of the metabolic constant can now be identified: $m_b' = A^6 m_b$. The cost function now has the same form. Since changing m_b is equivalent to changing the length scale, these results suggest that there are likely to be structural differences between organisms of different sizes, as the power required to pump blood becomes relatively more important than the metabolic demand to maintain blood volume in small vessels. In the absence of mor-

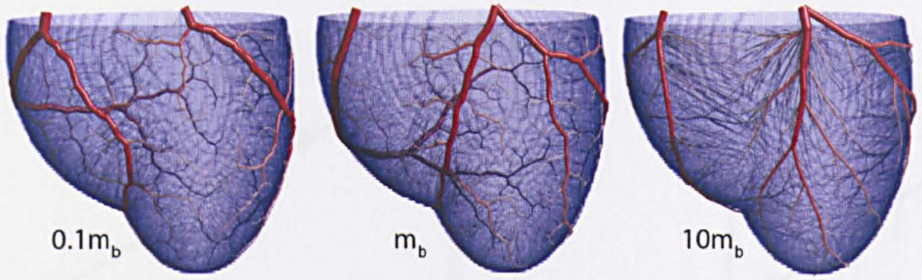

Figure 4.5: Example trees generated with different values of m_b, which changes the relative weight of the pumping power to cost of maintaining blood in the optimisation. For small m_b (corresponding to small hearts), vessels in the trees wind around - this is because there is little penalty to make a single wide vessel that curves to supply blood, rather than bifurcating. For large m_b (corresponding to large hearts) the vessels travel as straight as possible.

phological data, visual comparison of the coronary arteries tentatively indicates that vessels meander around in smaller species [146] and that vessels are straighter in larger species [105].

Figure 4.5 shows the effect of altering the metabolic energy cost of blood per unit volume m_b. The largest morphological change is found in the lengths of the larger arteries (Fig 4.6). As m_b increases, bifurcation symmetry is also increased in the larger arteries and as a result there is an increase in the number of Strahler orders present in the tree (Fig 4.6). The explanation for these scaling behaviours is evident when considering the limiting cases. For $m_b = 0$ the power involved in pumping the blood dominates the optimisation, which leads to a large, 'snaking' artery with small side branches that supply the tissue. This large artery would cover the entire surface of the heart, and the configuration is equivalent to a completely asymmetric binary tree. For a large m_b value (or small power cost) there is a huge penalty associated with larger arteries, and so their lengths are contracted. In order to accommodate the reduction in length, the larger arteries must bifurcate more frequently and symmetrically. Additionally the high volume cost causes the trunk artery to minimise its total length, resulting in a much straighter path across the tissue. Less extreme examples of this behaviour can been seen in Fig 4.5, with meandering arteries for small m_b and straight

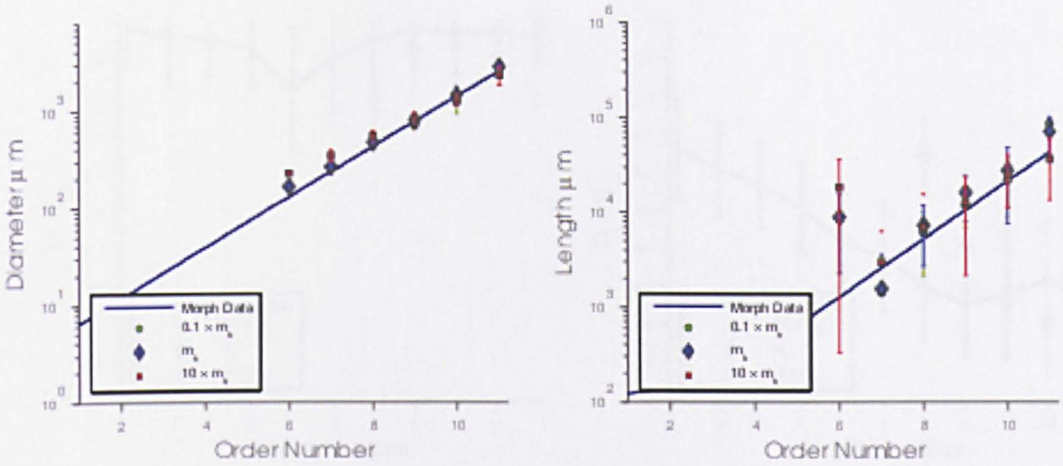

(a) (b)

Figure 4.6: (a) Diameter as a function of Order Number for trees with 1000 vessels. Decreasing m_b, which describes the relative energy cost of an amount of blood and the power required to pump it, has little effect on the agreement of the diameters with morphological data. (b) For lengths however there is an obvious effect in the larger arteries, with regimes of high pumping cost being more accurate. The primary optimisation for high pumping cost then is to increase the length of the largest arteries.

arteries for large m_b.

4.4 Discussion

We have developed a powerful and universal method for growing arterial trees *in-silico*, which is capable of identifying the near globally optimal configuration of arteries for arbitrarily shaped tissues with heterogenous blood supply demands. As input, the method only needs information about the tissue structure and the entry point positions of the largest arteries. From this information, the approach generates morphologically and structurally accurate coronary arterial trees at almost every length scale. This is a significant improvement on previous optimisation methods, which failed to reproduce the consistent structure found in the coronary arteries. We have shown that the method improves with the number of vessels modeled, so that, as computing power increases, there is a systematic improvement

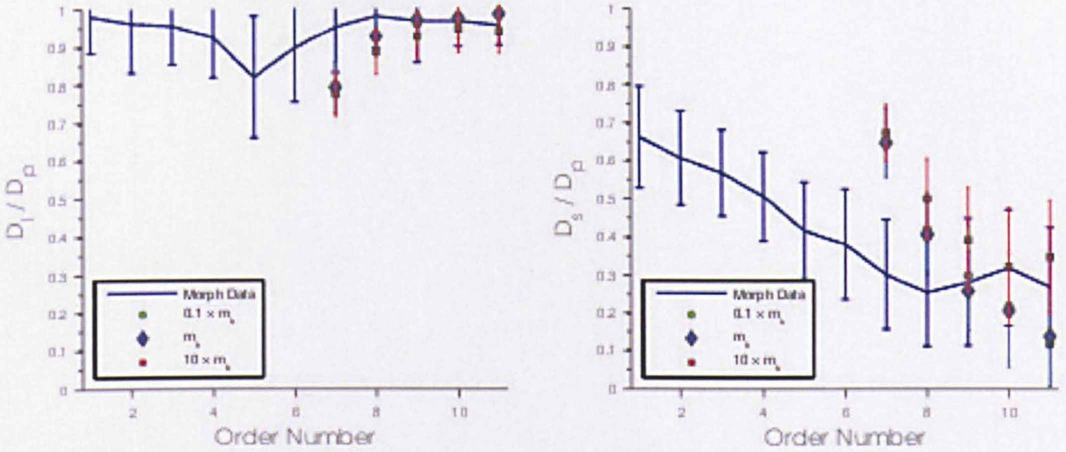

(a) (b)

Figure 4.7: (a) and (b) The main effect of changing m_b is a change in the asymmetry of the branching of the largest arteries - for large m_b, the branches are more symmetric than for small m_b. As m_b becomes very small, the limiting behaviour is broad trunks that wind around all the tissue, with a large number of very small offshoots that supply blood in the direct vicinity of the large vessel.

in the accuracy of the generated trees. To our knowledge, no other method can generate realistic arterial trees that closely match morphological data by taking only the shape of the tissue as input, and claim systematic improvement in the generated trees with increased computational power.

Chapter 5

Modelling Embolic Stroke

5.1 Introduction

While the results of the previous chapter validate the Simulated Annealing algorithm for use in generating the coronary vasculature, any organ specific application will require its own separate validation. In this chapter the capability of the algorithm to generate realistic cerebral vasculatures, in tissue volumes segmented from MRI images of a human brain, are assessed and validated. The extension of the algorithm is motivated by a specific application to a previously published statistical model of embolic stroke.

The chapter is divided into two main sections. In the first section the segmentation of MRI imaging data for the purposes of arterial tree modelling and generation of the cerebral arterial tree are described. The generated trees are subjected to morphological and vascular territory comparisons with *in vivo* data[144]. In the second section the statistical stroke model is outlined[46], and results of simulations performed both on the generated vasculature, and a symmetric bifurcating tree (the symmetric tree being the model previously employed in the stroke simulations of Hague *et. al.*[46]) are compared. The effect of using realistic vasculatures in the context of stroke modelling is assessed,

5.2 Cerebral Arterial Tree

The geometry of the Human brain is complex. The cerebral cortex contains deep folds on its surface upon which the pial arteries attach. At sub $250\mu m$ diameter scales, the microvasculature of the cerebral cortex extends into the cerebral tissue[87], perfusing blood into the capillary network. The larger arteries of the cerebral vasculature attach to the Circle of Willis (CoW), which acts as a distribution mechanism for the cerebral blood supply. The complex connectivity of the CoW is difficult to model in the context of arterial tree generation, and its anatomical structure is highly variable between individuals[76]. The primary issue for the arterial generation algorithm stems from the proximity of the major cerebral artery inlets. The middle, posterior, and anterior cerebral artery (MCA,PCA,ACA), connect to the CoW within a small volume (10mm^3). The proximity of the inlets forms a degeneracy which is difficult for the Simulated Annealing algorithm to resolve, and in general leads to solutions in which a single inlet dominates.

The internal structure of the brain also presents a new challenge. Unlike the heart which could be effectively modelled as consisting entirely of myocardial tissue, the brain is comprised of two very separate tissue types: white and grey matter. The two tissue types have different volumetric blood flow requirements per mass of tissue[85], which must be factored into the arterial tree generation algorithm, specifically the distribution of end node sites.

In order to convert the volumetric MRI data into a form compatible with the arterial generation algorithm, the images must first be cleanly segmented from the surrounding skull and meninges. The outer surface of the brain must then be extracted so that the distance map calculation on the internal volume can be performed, and the locations of the CoW inlets for the major arterial segments must be located so that realistic boundary conditions can be imposed. After the volume, surface and distance map data have been created, they can be loaded into the generation algorithm in the same manner as the ellipsoidal heart volume, or

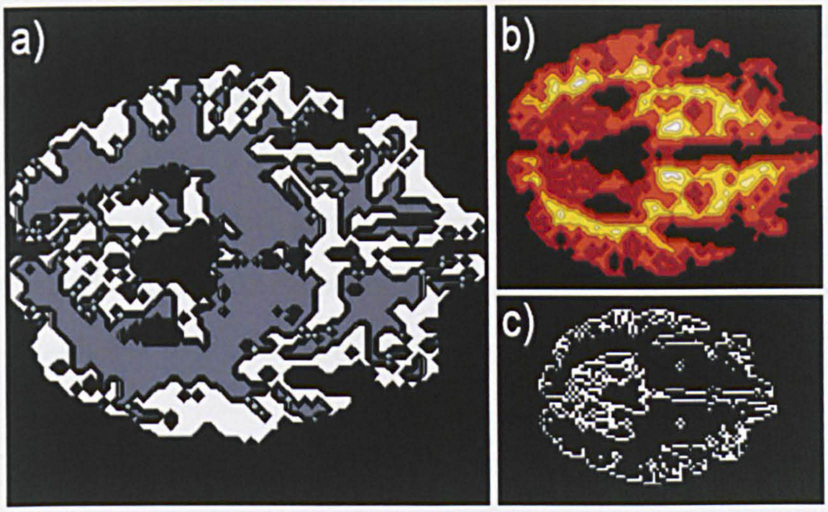

Figure 5.1: Here details of the MRI data used in the arterial tree generation model are displayed. Panel a) shows the segmented brain tissue. b) shows the result of the distance function calculation of the brain surface, which is shown in panel c).

any volume data, would be. Generation of the arterial trees then proceeds in the manner described in previous chapters.

5.2.1 MRI Data and Extraction

To create a realistic geometry in which to grow the cerebral arterial trees, T1 weighted MRI data of a healthy individual was obtained in the form of DICOM image slices. A TOF image was used in order to locate the starting positions of the major cerebral arteries: the Middle Cerebral Artery (MCA), Anterior Cerebral Artery (ACA) and the Posterior Cerebral Artery (PCA). The DICOM image files were loaded into MATLAB and the automatic segmentation routines in the statistical parametric mapping (SPM) MATLAB library were used to segment both white and grey matter from the tissue volume. The surfaces of the combined White and Grey matter were identified via a nearest neighbour search, where voxels having at least one unoccupied neighbour were labelled as belonging to the outer surface of the brain. These surface voxels were then used to compute a distance map from the surface to all occupied pixels, as previously discussed. A sample slice at each stage of the segmentation process is shown in Fig. 5.1. While the brain itself exhibits some asymmetry[139], at the length scale of the MRI image ($0.75 \times 0.75 \times 0.80\text{mm}^3$) the two hemispheres of the brain are effectively symmetric. It is reasonable then to divide the brain into left and right hemispheres and perform arterial tree generation for a single hemisphere only. A full tree could then be generated by either combination of trees grown for right and left hemisphere, or from joining a single tree to it's mirror image.

In comparison to the coronary vasculature, which has two "input" arteries, the brain has 3 major inlets in each hemisphere: the MCA, PCA and ACA. These inputs are connected through the circle of Willis so that a concentration of flow in one would mean a reduction in flow to the other. In the case of the heart, the coronary arteries attach directly to the aorta, with each pulling a relatively small amount of blood, so small that the effect on the overall aortic flow (5%) can be neglected and the two arterial inputs treated as effectively separate. As this is not true in the brain, only a single arterial inlet will be provided to the generation algorithm. The three cerebral arteries supply very separate territories of the brain, and it will be left to the SA algorithm to determine whether this behaviour is replicated. I adopted this approach in part as a remedy to the problem of atrophied inlets, but under consideration too was avoiding the addition of unnecessary adhoc rules to the algorithm: where possible, the optimisation procedure should take care of organ specific details. There are other solutions to the inlet problem: for instance, flow constraints in each inlet could be the target of the SA algorithm. This would guarantee correct vascular territory sizes and flow proportions for the MCA, PCA, and ACA, but it would also make it impossible to discern to what extent those morphological properties are the result of energy optimisation.

5.2.2 Arterial Tree Generation

As with the Heart, the generation of the Cerebral vasculature requires inputs other than the geometry. The radius and flow of the root node can be calculated from summation of average flow values, and the radius exponent summation of the average MCA, ACA and PCA radii so that:

$$f_{\text{root}} = \langle f_{\text{MCA}} \rangle + \langle f_{\text{PCA}} \rangle + \langle f_{\text{ACA}} \rangle \tag{5.1}$$

and

$$r_{\text{root}}^{\gamma} = \langle r_{\text{MCA}} \rangle^{\gamma} + \langle r_{\text{PCA}} \rangle^{\gamma} + \langle r_{\text{ACA}} \rangle^{\gamma} \tag{5.2}$$

The diameters of the MCA, PCA and ACA were taken as 2.7mm, 2mm and 2mm[123]. The flow rates in the MCA, PCA and ACA were taken as 127 ml/min, 51 ml/min and 88 ml/min[34]. A branching exponent γ of 2.5[23, 145] was chosen, so that the total radius of the root node is 1.35mm.

In cerebral tissue arterioles of diameters less than $300\mu m$ are responsible for penetrating deep within cortical tissue[21]. As a result the node exclusion parameter was set to $300\mu m$ so that only arteries with radii less than this would penetrate into the voxelised tissue map. Grey and white matter are distinguished by the relative amount of blood supply they require[85], which affects the number of voxels supplied by each terminal site in the arterial tree. The result is that the density of the generated trees terminal sites should be much less in the white matter than in the grey. The grey and white matter blood supply requirements were provided as input to the simulation, at values of $1.3 \times 10^{-5} \mathrm{m}^3\mathrm{s}^{-1}$ and $0.6 \times 10^{-5} \mathrm{m}^3\mathrm{s}^{-1}$ respectively[85]. Multiple cerebral arterial trees were generated, with the tree producing the lowest value of the cost function being chosen as the final output. The Simulated annealing algorithm was given 5×10^9 steps spanning a temperature range of 10^{12} to 10^{-11}.

5.2.3 Results

The morphology of the generated arterial tree is compared with the data of Wright *et. al.*[145] who extracted cerebral arterial tree morphometry from 3. T time-of-flight MRA high-resolution images of 61 healthy volunteers. In contrast to the coronary data of Kassab *et. al.*[70] which was categorised in terms of diameter defined Strahler order, Wright *et. al.* labelled arterial segments using the branching number. In assigning branching number, the root node is first given order number 0. The tree is then traversed recursively, and at each bifurcation the order number is incremented by 1. The trees used by Wright *et. al.* were segmented from MRI images with a resolution of $0.5 \times 0.5 \times 0.5\text{mm}^3$ and as a result the arteries it includes span a relatively low range of radii (1.1mm to 0.5mm). This low range allows the ordering scheme they employed to be feasible, where in larger, asymmetric trees it would create very large values of the maximum branch order, and result in arterial segments with vastly different morphological properties being labelled with the same branch number.

In order to allow a comparison of the generated trees to the data of Wright et. al. the MRI segmentation process needs to be replicated in the generated trees. The effect of the MRI and subsequent segmentation is to prune arteries which have a radius of less than approximately 0.5mm, which is relatively straightforward to replicate in the generated trees. In the subsequent morphological comparisons only the arteries in the generated tree with radius $\geq$ 0.5mm are considered. After the pruning, there exist many connected arterial segments which have the same value of order number. This occurs for instance when the small branches of a large trunk artery are pruned and the bifurcations are transformed into "internal" nodes. The internal nodes are points of direction and radius change without bifurcation, and the arterial segments which contain them are grouped together into a single segment. Wright *et. al.* performed the same procedure, and calculated the radii of the arterial segments as the average radius along the segment length. The same method is reproduced in the analysis performed on the generated trees.

The analysis of Wright et. al. includes some metrics which do not exist, or exist to only a limited degree, in the generated arterial trees. The analysis includes measures of the tortuosity of the arterial segments, which exists in the generated trees only to the extent that pruning leads to the creation of internal nodes. Wright *et. al* also include data on the path and euclidean distances traversed by a segment. The path distance is the total length of the arterial segment, and the euclidean distance is the straight line distance between the start and end point of the segment. Due to the lack of tortuosity in the generated trees, the extent to which the path and euclidean distances of segments differ is severely restricted.

Wright *et. al* divided their data into those segments belonging to the MCA, ACA and PCA. To perform the same analysis on the generated trees requires that the locations of the MCA, ACA and PCA be identified, as there is only a single root point in the generation algorithm. To achieve this, the tree was first pruned of segments with radii less than 0.5mm. The tree was then rendered in 3D so that the root points of the major arteries could be manually identified. The root points were chosen under the following conditions: that their radii conform within error to the associated cerebral artery[124]; and that the locations of the end nodes attached to the root lay within the vascular territory of the associated cerebral artery.

Appearance

Figure 5.2 shows the appearance of the generated vasculature from three axis. The MCA, PCA and ACA are color coded (red, green and blue respectively), and the pale pink segments indicate sections of the tree which have been identified as being representative of the Circle of Willis. This occurs at the points before the common parent of two of the major arteries. The vascular territories are apparent in the image, with the ACA supplying the majority of the front of the brain and the PCA supplying the cerebellum. The MCA supplies the largest

Figure 5.2: Cerebral vasculature automatically generated on a geometry obtained from MRI imaging. Aterial segments belonging to the MCA, PCA and ACA are color coded red, green and blue respectively. The pale pink arteries are segments which can not belong to any definitive major cerebral artery; in subsequent analysis they are excluded as being representative of the Circle of Willis.

volume of tissue and covers a wedge between the front and rear.

Radii

Figures 5.3, 5.4 and 5.5 show a comparison of the relationship between arterial radius and order number for the MCA, PCA and ACA respectively. The solid lines indicate the data extracted from the generated trees and the dashed lines the data of Wright *et. al*. For the MCA (Fig. 5.3) the general agreement with experimental data is good. The overall behaviour of the radii as a function of branching order is matched between the experimental and generated data, however there are significant deviations from the expermental values at specific points. This could be due to the low sample size involved in the data points for the generated tree (> 10).

Both the PCA and ACA show significant deviation from the experimental values. The size of both of these trees in terms of numbers of bifurcation is small (< 15), and so it is possible that the differences could represent normal statistical variation (Wright et. al. did not publish errors).

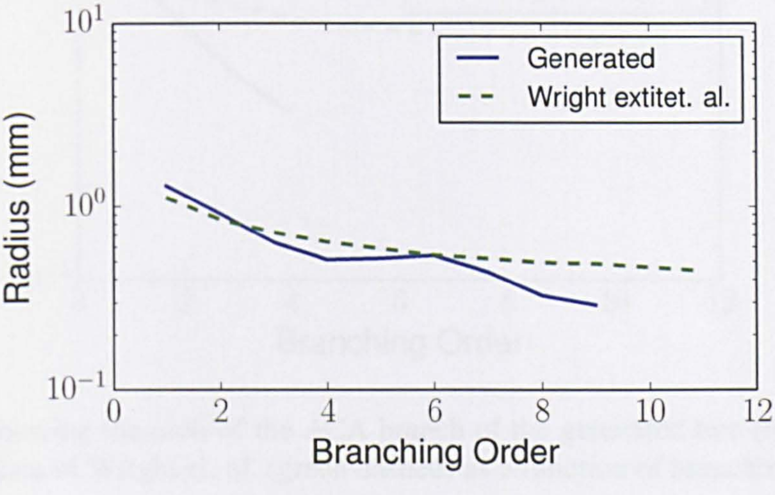

Figure 5.3: Plot showing the radii of the MCA branch of the generated tree (blue solid) vs the experimental data of Wright et. al. (green dashed) as a function of branching order.

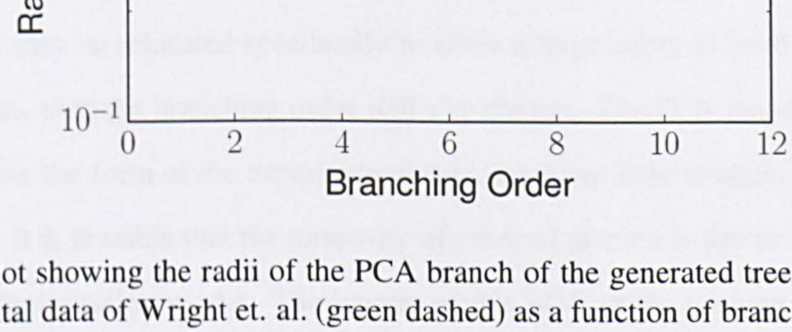

Figure 5.4: Plot showing the radii of the PCA branch of the generated tree (blue solid) vs the experimental data of Wright et. al. (green dashed) as a function of branching order.

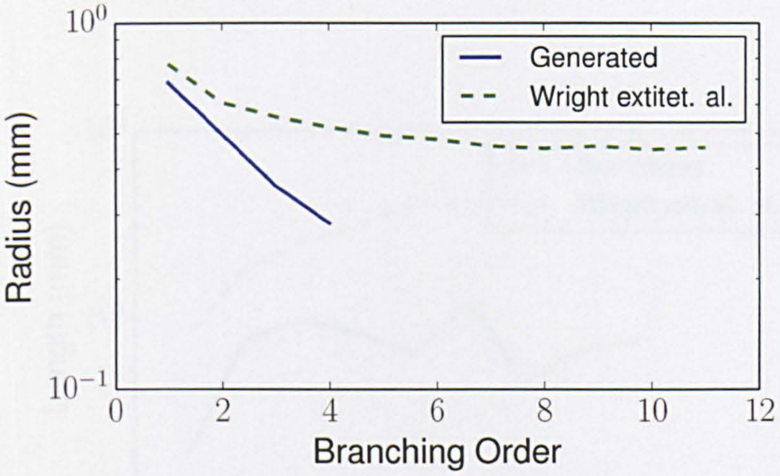

Figure 5.5: Plot showing the radii of the ACA branch of the generated tree (blue solid) vs the experimental data of Wright et. al. (green dashed) as a function of branching order.

Lengths

Figures 5.6, 5.7 and 5.8 show the relationship between length and branching order for the MCA, PCA and ACA branches of the generated tree respectively. The MCA lengths (Fig 5.6) show a similar variation with branching order in comparison to the experimental data of Wright et. al, however there is a systematic underestimation of the segment lengths. Since arterial segments of living trees are rarely straight segments, this is not suprising. In the generated trees a bifurcation must occur in order for a branch to change direction, meaning that a bifurcation may be relocated specifically to allow a large artery to bend along a surface. If this occurs, then the branching order will also change. The PCA lengths (Fig. 5.7) also broadly follow the form of the experimental data, however there is again a systematic underestimation. It is possible that the tortuosity of cerebral arteries is due to a feature not captured by the optimisation model. The lengths of the ACA in the generated trees (Fig. 5.8) do not follow the experimental data. While the length of the first segment is correct, the overall behaviour of the lengths with the variation of order number is incorrect.

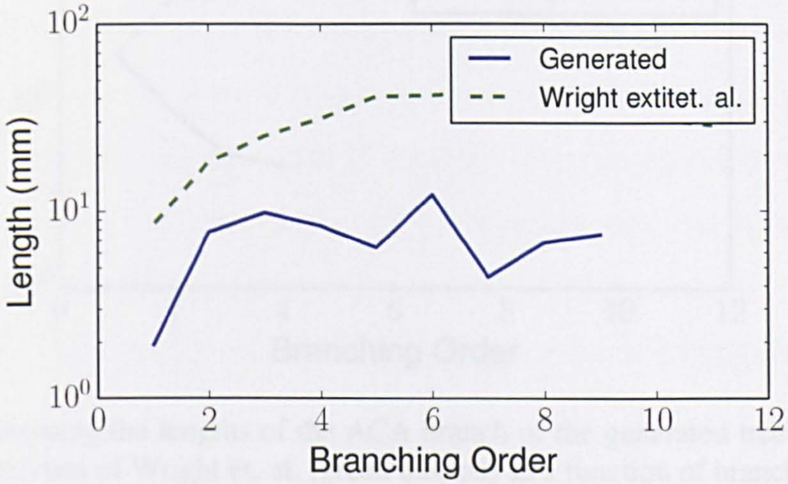

Figure 5.6: Plot showing the lengths of the MCA branch of the generated tree (blue solid) vs the experimental data of Wright et. al. (green dashed) as a function of branching order.

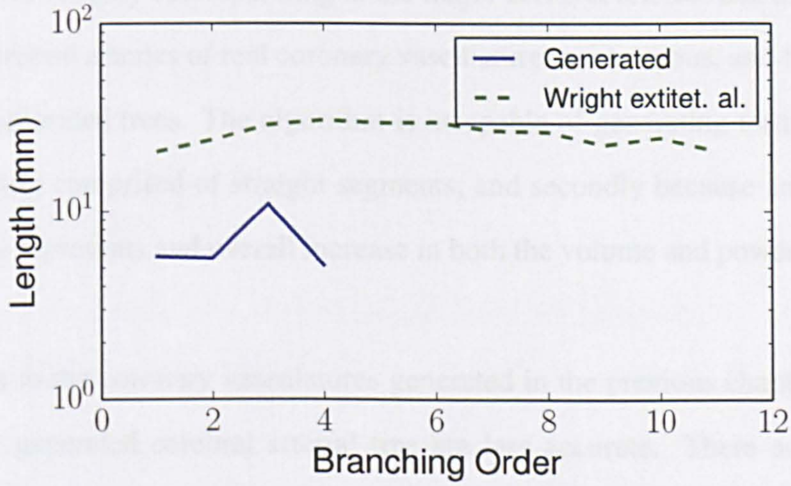

Figure 5.7: Plot showing the lengths of the PCA branch of the generated tree (blue solid) vs the experimental data of Wright et. al. (green dashed) as a function of branching order.

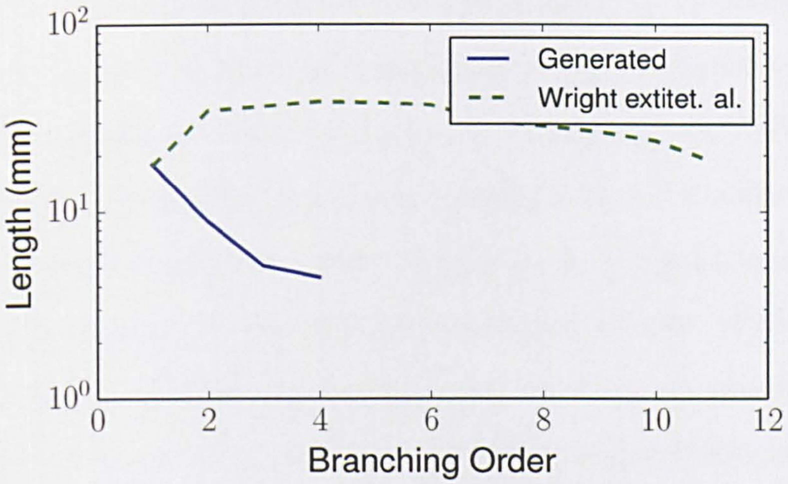

Figure 5.8: Plot showing the lengths of the ACA branch of the generated tree (blue solid) vs the experimental data of Wright et. al. (green dashed) as a function of branching order.

5.2.4 Discussion

In comparison to images of *in vivo* cerebral arterial trees and their vascular territories, the visual appearance of the generated trees is promising. Given that there was only a single root point to the tree, it is encouraging that the algorithm produced solutions which produced major arteries roughly corresponding to the major cerebral arteries and their vascular territories. The cerebral arteries of real coronary vasculatures are tortuous, and this aspect is absent from the generated trees. The algorithm is incapable of generating tortuosity firstly due to arteries being comprised of straight segments, and secondly because an increase in length of an artery represents and overall increase in both the volume and power cost of that artery.

In comparison to the coronary vasculatures generated in the previous chapter, the morphological of the generated cerebral arterial tree are less accurate. There are clear discrepancies between the experimental data and the generated results. The branching order dependence of the radii for the ACA for instance is clearly incorrect, both in value and overall form. In contrast however, the values and form of the dependence for the MCA is encouraging. The length depdence in the MCA segment is also encouraging, however there is a clear need to investigate the effects of adding some form of tortuosity to the model.

The PCA and ACA are both underrepresented in terms of numbers of bifurcations involved in the vasculature. They both consist of less than 15 total bifurcations, and it is difficult to distinguish between what may be statistical variation and what may be inadequecies in the formulation of the algorithm. The generation of larger trees consisting of many thousands of segments may somewhat alleviate this uncertainty. The underrepresentation of the root radius of the PCA suggests that the algorithm has not ascribed the full vascular territory of the PCA, where the MCA has acquired a vascular territory larger than expected.

5.3 Application: Modelling Embolic Stroke

In this section the previously generated arterial tree is used to perform a statistical simulation of embolic stroke. The stroke simulation is based upon the work of Hague *et. al*[26, 45, 46], but the performance of the algorithm has been improved to allow for potential real time applications and to improve the statistical accuracy of the results. The effect of using a computer optimised vascular tree versus an entirely symmetric tree is assessed, and the physical locations of blockages occurring in the generated tree are analysed.

5.3.1 Introduction

The applications for computer generated vasculatures are numerous[77, 80, 102]. Organ specific blood flow[92], drug delivery[121], and imaging phantoms[33] all use computerised vasculatures to improve realism, and the ability to generate realistic vasculatures for arbitrary three dimensional tissue volumes could potentially lead to further advances in these areas. As an example case, the arterial tree generated in the previous section will be used in a statistical simulation of embolic stroke, previously developed by Hague *et. al*[26, 46]. The ability to model the process of embolic stroke on patient specific vasculatures, generated from MRI imaging, could have important clinical applications, specifically in the area of open heart surgery[46], where gaseous embolisation can pose a significant risk[9].

Embolic stroke accounts for 22% of all strokes, and is the second most common form of stroke behind atherothrombotic brain infarction which accounts for 61%[20]. The consequences of gaseous or solid emboli entering the cerebral vasculature can be devastating. Cerebral tissue deteriorates rapidly whilst blood flow is halted, but the exact neurological effects of an embolic event can be difficult to quantify (e.g silent strokes[136]). The most common causes of gaseous embolisation are decompression sickness and clinical cardiovascular intervention (particularly open heart surgery featuring cardio-pulmonary bypass), but gaseous emboli are also formed in mechanical heart valves albeit at low levels. Solid emboli occur when a fragment of solid material exists within the circulatory system. Typically they are thrombi[50], however there are numerous means of production and solid emboli can be formed from various materials. Solid emboli typically cause significantly more tissue damage than gas[96], and the effect of a large embolus entering the cerebral vasculature (stroke) can be clearly resolved by perfusion weighted MRI imaging[115].

Models of embolic stroke are typically animal based[6, 7, 104], and knowledge of the role of the cerebral circulation has been largely derived from perfusion studies on cadavers, or magnetic resonance perfusion studies on healthy individuals[107]. More recently, large scale fluid dynamics studies of embolus trajectories have been performed[35, 93, 129], which suggest that the distribution of embolus depositions during embolisation may be dependent on both the size of the embolus and on the specific anatomy of the vascular system.

Hague *et. al.*[27] have previously demonstrated the use of a Monte Carlo simulation in the prediction of arterial blockage during gaseous embolisation. The method used a symmetrically bifurcating arterial tree to model the cerebral vasculature. This tree was entirely topological and contained no spatial information, so that extraction of blockage data was limited entirely to the temporal dimension. Using the more accurate computerised model of the cerebral vasculature generated in the previous section, the embolic stroke model can be extended to more accurately account for branching asymmetry and the spatial distribution of blockages. The first point is important as vessel asymmetry will influence the topological distance between blockages[109], and the second because strongly spatially correlated blockages are more immediately dangerous due to the reduction of cross flow in the capillary beds[101].

5.3.2 Integration of Cerebral Vasculature

The tissue damage caused by solid and gaseous emboli are a result of arterial segment occlusion, leading to reduced blood to a localised volume. The reduction in flow persists so long as the embolus continues to block the arterial segment, causing hypoxia, swelling, and eventually and cell death. As the embolus dissolves over time, it traverses through arterial tree, blocking ever smaller arterial segments, until it has dissolved sufficiently to pass through the capillary bed. In the generated tree, arterial segments are terminated well above the capillary bed radius of $\approx 5\mu\text{m}$. To correctly account for the cascade of a dissolving embolus, an extension to the generated arterial trees, which bridges the gap between capillary bed and terminal segment radius, is required.

At each of the terminal points of the generated tree a symmetrically bifurcating tree is attached. The symmetric tree spans radii from the terminal segment radius of the generated tree r_e to just above the capillary radius at $r_{\text{cap}} 5\mu\text{m}$. The bifurcation exponent of this symmetric tree is matched to the generated tree at a value of 2.5, and the length of the individual arteries are calculated as $20r_s$ where r_s is the radius of the segment[46]. The number of bifurcations required in the symmetrically bifurcating tree can be calculated using r_e and The attached symmetric trees allow for emboli smaller than the terminal segment radius of the generated tree to block flow, but because the symmetric tree contains no spatial data the physical location of the blockage is unresolveable. The blockages associated with the terminal sites of the generated tree are calculated as the ratio of the attached symmetric tree end nodes which receive no flow to the total number of attached end nodes:

$$\mathbf{B}_i = \frac{n_{blocked}}{n_{total}} \tag{5.3}$$

Where n refers to the total number of symmetric tree end nodes attached to the end node of the generated tree, and blocked(unblocked) refer to the relative proportion of those end nodes currently experiencing blockage(normal flow). The spatial distribution of the blockages can then be mapped by associating the blockage value $\mathbf{B}_i$ with the spherical supply volume of the generated tree end node. While this procedure allows small emboli to contribute to a spatial map of blockages, it can not distinguish between certain patterns of blockages below the generated tree radius. A specific blockage ratio $\mathbf{B}_i$ can be formed from a single embolus, from many small emboli, or some combination. To account for this a time average of the blockages can be taken. In this case a single embolus will contribute a larger total blockage than would many small emboli.

5.3.3 The Stroke Model

The stroke model previously developed by Hague *et. al* is a Monte Carlo simulation which tracks blockages caused by emboli as they traverse through a vascular tree. The emboli navigate the bifurcations of the tree probabilistically, preferentially following the maximum relative amount of blood flow until they reach arterial segments smaller than a certain radius. Once an embolus has become "stuck", the flow of blood distal to that point in the tree is temporarily cut off, and the fluid dynamic properties in the rest of the tree are recalculated. Emboli are inserted at the root node randomly, but with an average insertion per unit time equal to the rate of embolisation τ. Once inserted the emboli begin to dissolve at a rate proportional to their surface area[26], with the specific rate depending on their composition (gaseous vs solid).

Various experimental data[17, 109] suggest that emboli flow in specific proportions through the outlets of a bifurcation. In the limit of the embolus size approaching that of red blood cells, the proportion should be equal to that of the hematocrit division at the bifurcation, which for symmetric bifurcations is essentially proportional to blood flow division[110]. The regime where emboli are divided in proportion to the flow division at a bifurcation is known as the linear flow weighting regime. Non-linearities can arise as a result of large asymmetries involving small vessels ($< 30\mu$m), which in the present model can be neglected as a result of the symmetric tree model used for segments of radius $< 100\mu$m. For large emboli (ratio of embolus to daughter artery diameter > 0.5), non-linearities also occur[17] at asymmetric bifurcations, resulting in a disproportionate amount of emboli entering the larger daughter. The non-linearity arises due to the Fahraeus-Lindqvist effect[109], causing non uniform distributions of particles in the radial direction as a function of both particle and arterial radius. In the cerebral vasculature this is thought to cause preferential deposition of emboli at the termination points of the larger arteries.

The MCA shows a disproportionate uptake of emboli with regard to a linear flow weighting scheme[24], consistent with the high proportion of stroke events seen in the vascular territory supplied by the MCA. For small emboli (radius of emboli to parent artery < 0.07), the linear flow weighting regime is recovered. Chung *et. al* performed a study of embolus deposition for a realistic phantom of the major cerebral vasculature, including the CoW, and found preferential deposition in the MCA branches for large emboli. Fluid dynamic simulations of specific anatomies[19, 25] indicate that individual arterial configurations also heavily influence the trajectory of emboli. Hague *et. al*[46] derived a semi-empirical flow weight relationship from the data of Bushi *et. al*[17] for use in their stroke model, however little difference was observed in comparison to simulations performed with the simpler linear weighting.

Full 3D fluid dynamical simulations of embolus trajectories in vascular systems are computational feasible only for relatively small systems, but embolic stroke involves the occlusion of arteries which may be proximal to high numbers of arterial segments, and supply large volumes of tissue. A large scale model of the cerebral vasculature, containing upwards of 2^{20} total bifurcations and capable of dynamically incorporating occlusions due to emboli, would be computationally infeasible if detailed fluid dynamics calculations were performed. To allow such a simulation to be performed in reasonable time requires a number of simplifying assumptions which will now be described:

1. Flow throughout the cerebral vasculature system is laminar.
2. Vessel walls are thin and non-elastic, with constant radius.
3. Embolus deposition is proportional to flow division.
4. An embolus dissolves proportional to its surface area.
5. There is no blood flow distal to a blockage.
6. The time taken to traverse an arterial segment is much less than the typical timescale of dissolution.

The first assumption is the same as that used in the arterial generation algorithm, but is essential due to the large numbers of arterial segments in involved in the stroke simulation. The second assumption ignores the effect of cerebral autoregulation[58], pulsatile flow[91] and potential vasoconstriction due to cerebral swelling[18]. The third assumption ignores the previously discussed non-linear effects for highly asymmetric or large emboli. The magnitude of these effects had been previously studied by Hague *et. al.* and was found to be minimal within the stroke model. The fourth assumption is relatively well accepted[46], however may not be valid for gaseous emboli, or those emboli blocking arteries. The fifth

```
while $T < T_{end}$ do
    if $U(0,1) < \tau$ then
        Generate e of size $U(0,1) \times r_{\max}$
        Add e to $\mathscr{T}$ at root node
    end
    for $e \in \mathscr{T}$ do
        if $r_e < r_{cut}$ then
            Remove e
        end
        Move e
        Dissolve e
        Check for blockage at e's location in $\mathscr{T}$
    end
    Recalculate Pressures, flows and resistances in $\mathscr{T}$
end
```

Algorithm 1: Stroke simulation algorithm[46]. Where $\mathscr{T}$ denotes the bifurcating tree on which the simulation is being performed, $U(0,1)$ a uniform pseudo-random number between 0 and 1, r_{cut} the radius of the smallest arteriole in $\mathscr{T}$, $r_{\max}$ the radius of the largest embolus being simulated, T_{end} the embolisation time period, and τ the rate of embolisation. The specific rules used for whether an embolus **e** can move or not depend upon its composition (gaseous or solid), as do the rules for checking whether an embolus has blocked a specific segment in the Tree ($\mathscr{T}$).

assumption directly relates to the arterial generation algorithm, which does not include connections between subtrees. The final assumption relates to the implementation of the algorithm, which assumes an embolus will traverse a single arterial segment during each time step (provided it is not blocked).

The basic outline of the stroke simulation is presented in Algorithm 1. The process of checking for blockages involves not only finding those emboli whose radii exceed the radius of their current arterial tree location; but also finding those segments of the tree for which all distal terminal nodes are blocked. These segments are "stagnant" and experience no flow, so that any emboli within them are unable to move. The last step of the algorithm is the most computationally expensive, as it potentially involves the recalculation of 2^{20} fluid dynamical quantities.

5.3.4 Fast Fluid Dynamics

In previous work Hague *et. al*[26, 45, 46] used a recursive algorithm to calculate the fluid dynamic properties for the symmetric tree. The algorithm first recursively assigns resistances based upon the resistance of the current segment, plus contributions from the distal subtrees. The distal subtrees act as resistors in parallel, and so their contributions are summed using the familiar rule for resistors. The total resistance provided by segment i is then:

$$R_i = \left(\frac{1}{R_{sub1}} + \frac{1}{R_{sub2}}\right)^{-1} + r_i \tag{5.4}$$

Where R_i is the total resistance provided by the segment, R_{sub} indicates the resistance of a subtree of segment i, and r_i is the resistance of the segment length. In order to calculate the flow and pressures in the tree a boundary condition must first be chosen. Hague *et. al*[26, 45, 46] chose the boundary condition to be a constant inlet pressure of 100mmHg, so that the total flow through the tree varies as the resistances of the tree changes. Once a boundary condition is chosen the rest of the fluid dynamical properties can be calculated by traversing the tree from root to end node and assigning values of pressures and flow. As flow is conserved throughout the tree, the flows in each node can be calculated as a fraction of the flow in the parent. The fractions of flow sent to the first and second subtree of node i are given by:

$$Q_{sub1} = \frac{R_{sub2}}{R_{sub1} + R_{sub2}} \quad \text{and} \quad Q_{sub2} = \frac{R_{sub1}}{R_{sub1} + R_{sub2}}$$

Where Q_{sub} is the fraction of the parent flow given to the subtree and R_{sub} is the total resistance provided by the subtree. The pressure at the outlet of a node can be calculated as:

$$\mathrm{P}_i = \mathrm{P}_p - Q_i r_i \tag{5.5}$$

Where P_p is the pressure at the outlet of the parent node and r_i is the resistance along the segment length. The algorithm can correctly calculate the pressures, flows and resistances for even very large trees (2^{20} nodes) however due to the use of recursion and the necessity to recalculate all flows and resistances after a single change in the tree (e.g. an embolus blocking an artery), it performs rather poorly. In order to speed up the computation, produce more statistically accurate results, and provide scope for real time usage in clinical settings, an effort was undertaken to drastically increase the performance of the algorithm.

While a blockage event in the tree affects the flows and pressures in the entire tree, changes in resistances occur only for the segments connected proximally to the event. When a blockage occurs, the change in resistances can be sent up the tree (See Algorithm 2), which for a tree consisting of 2^{20} nodes means reducing the number of calculations performed by a factor of 10^{-19}. For a solid embolus, the direction of travel at a bifurcation is a function of the relative flow in each branch, and from Eq 5.3.4 these can be calculated entirely from the resistances. For a gaseous embolus however, the value of the pressure in the segment is required in order to decide whether the embolus will block the flow. This calculation must be performed after the resistances are calculated, and requires at least one recursion of the tree.

Implementation of the fast resistance update for solid emboli provided a near 3 orders of magnitude performance benefit over the recursive algorithm. For gaseous emboli, which require the pressure, the performance increase was more modest at around a single of order magnitude. In both cases the largest improvement is seen when a high number of emboli are present, however it is unclear how much of this is a result of the fluid dynamics optimisation and how much is a result of other algorithmic improvements.

5.3.5 Analytic Approximation

The dynamics of the stroke model can be incredibly complex. Many hundreds of emboli can be present in the tree at any one time, each affecting the trajectory of the next embo-

```
for e in $\mathscr{T}$ do
    if e changed state then
        i = Location of e in $\mathscr{T}$
        while Bifurcation i is not root do
            i = Parent of i
            if i is Blocked then
                break
            end
        end
        if i is Root then
            Add location of e to List of Blockages
        end
    end
end
for i in List of Blockages do
    while Bifurcation i is not root do
        i = Parent of i
        Recalculate resistance i (Using Eq 5.4);
    end
end
```

Algorithm 2: Fast fluid dynamics for the Stroke simulation. An embolus is considered to have changed state if goes from being stuck to not stuck, or vice versa, in the current time step. The list of blockages created in the first for loop represent top-level blockages in the tree. Any blockages below that do not need to be considered.

lus entering the tree. This complexity combined with the number of bifurcations involved means that many simulations must be performed in order to reach a significant level of statical accuracy. In the following section I will develop an analytical approximation to the full monte carlo dynamics of the stroke model. The results of the model are compared with the results of the monte carlo simulation for a fully symmetric tree, and it is found that the approximation performs well over a large portion of the model parameter space.

To construct a rate equation for the number of emboli at time t, we first note that the production rate for emboli of all sizes in time dt is equal to τ. The average size of an embolus, $\langle r \rangle$, produced in time dt is equal to $0.5r_{\max}$, where $r_{\max}$ is the largest embolus size. The time taken for all emboli produced in time dt to dissolve will be $\frac{\langle r \rangle}{\alpha}$, where α is the rate of dissolution of the emboli. Thus in time dt the fraction of emboli which have dissolved will be $\frac{\alpha \mathrm{dt}}{\langle \mathrm{r} \rangle}$. Summing these terms, we arrive at the rate equation for the total number of emboli:

$$\frac{\mathrm{dN}}{\mathrm{dt}} = \tau - \frac{\alpha \mathrm{N}}{\langle \mathrm{r} \rangle} \tag{5.6}$$

Which has the solution:

$$\mathrm{N(t)} = \frac{\tau \langle \mathrm{r} \rangle}{\alpha} \left(1 - e^{-\frac{\alpha t}{\langle \mathrm{r} \rangle}} \right) \tag{5.7}$$

Where the boundary condition N(0) = 0 has been imposed. At equilibrium $\frac{\mathrm{dN}}{\mathrm{dt}} = 0$, and thus $N_{eq} = \frac{\tau \langle \mathrm{r} \rangle}{\alpha}$ is the equilibrium saturation of emboli within the tree. The average embolus size at equilibrium, $\langle \mathrm{r} \rangle_{eq}$, is not equal to the average size of emboli introduced to the tree ($\langle \mathrm{r} \rangle$), due to contributions of emboli released at previous times. To calculate the average embolus size we first note that only emboli introduced at time $\mathrm{t} - \frac{r_{max}}{\alpha}$ will contribute. We now work in the time interval 0 to $\frac{\mathrm{r_{max}}}{\alpha}$, and find that the fraction of emboli contributed at time t which still remain in the tree, with radius equal to $\mathrm{r_{max}} - \alpha \mathrm{t}$ is equal to:

$$N_{\mathrm{t}} = \frac{\tau \alpha \mathrm{t}}{\mathrm{r_{max}} N_{\mathrm{eq}}} \tag{5.8}$$

The average radius at equilibrium can now be calculated as:

$$\langle \mathrm{r} \rangle_{\mathrm{eq}} = \int_0^{\frac{\mathrm{r_{max}}}{\alpha}} N_{\mathrm{t}} (\mathrm{r_{max}} - \alpha \mathrm{t})\, \mathrm{dt} = \frac{\mathrm{r_{max}}}{3} \tag{5.9}$$

Where the equilibrium distribution of emboli as a function of radius r is given by:

$$\mathrm{N(r)} = \frac{\tau}{\alpha} \left(1 - \frac{\mathrm{r}}{\mathrm{r_{max}}} \right) \tag{5.10}$$

Integration of this equation between 0 and $\mathrm{r_{max}}$ recovers the equilibrium saturation $\mathrm{N_{eq}}$. The average blockage at equilibrium due to the distribution in Eq. 5.10 can now be calculated. The fraction of terminal sites in the tree blocked by an embolus at level i in the tree is given by:

$$B_i = 2^{-i} \tag{5.11}$$

Using the approximation that the tree holds a continuum of radii from 0 to r_{root}, an embolus of radius r blocks the tree at i(r) given by:

$$i(r) = -\gamma \ln \frac{\frac{r}{r_{root}}}{\ln 2} \tag{5.12}$$

So that the blockage due to an embolus of radius r is given by:

$$B(r) = \left(\frac{r}{r_{root}}\right)^{\gamma} \tag{5.13}$$

Combing Eq's 5.10 and 5.13 and integrating from 0 to r_{max} we find the average blockage at equilibrium:

$$\langle B \rangle_{eq} = \frac{\tau r_{max}}{\alpha} \left(\frac{r_{max}}{r_{root}}\right)^{\gamma} \left(\frac{1}{\gamma+1} - \frac{1}{\gamma+2}\right) \tag{5.14}$$

5.3.6 Non-Equilibrium Dynamics

In order to calculate the maximum blockage experienced for time periods less than the equilibrium saturation time $\frac{r_{max}}{\alpha}$, the embolus size distribution at time $t < \frac{r_{max}}{\alpha}$ must be calculated. To construct this, the first point to note is that in time period dt the size distribution created will be a top hat function of height τ and width r_{max}. If the embolisation time t is less than than the equilibrium saturation time, the distribution function will no longer be analytic but instead be a composite function. The first part of the distribution function consists of a flat distribution of height $\tau(\frac{r_{max}}{\alpha} - t)$, which ranges from embolus sizes of $r = 0$ to $r = r_{max} - \alpha(\frac{r_{max}}{\alpha} - t)$. The second part resembles the equilibrium distribution, having value $\tau(\frac{r_{max}}{\alpha} - t)$ at $r = r_{max} - \alpha(\frac{r_{max}}{\alpha} - t)$ value 0 at $r = r_{max}$. The Non-equilibrium blockage is then given by:

$$\langle \mathbf{B} \rangle_{\text{non-eq}} = \frac{\tau}{\alpha} \frac{r_{\text{max}}^{\gamma+1}}{r_{\text{root}}^{\gamma}} \left(\frac{1}{\gamma+1} - \frac{1}{\gamma+2} \right) - \frac{\tau}{\alpha} \frac{r_{\text{lim}}^{\gamma+1}}{r_{\text{root}}^{\gamma}} \left(\frac{1}{\gamma+1} - \frac{r_{\text{lim}}}{r_{\text{max}}(\gamma+2)} \right) + \frac{\tau t}{r_{\text{max}}} \frac{r_{\text{lim}}^{\gamma+1}}{r_{\text{root}}^{\gamma}} \frac{1}{\gamma+1} \tag{5.15}$$

Where $r_{\text{lim}} = r_{\text{max}} - \alpha t$. As expected, when $t = \frac{r_{\text{max}}}{\alpha}$, the result of Eq 5.14 is recovered.

5.3.7 Results

Symmetric and Generated Trees

Fig. 5.9 shows the average maximum blockage which occurs in the symmetric tree for a wide range of maximum embolus size and embolisation times. These results are similar to those obtained by Hague *et. al.*[46], which is expected given the only variation between the two models is the size of the root radius. Fig 5.10 shows the results of the same simulations performed on the generated trees. There is a marked difference in the average maximum blockage between the two trees, suggesting that branching asymmetry can reduce the potential impact of embolic events in the cerebral vasculature.

The reduction in maximum blockage occuring for the generated tree is most prominent at low embolisation rates ($\tau < 0.1\text{s}^{-1}$). At high embolisation rates the results of the two trees are almost indistinguishable. In addition, at very low embolisation rates ($\tau < 0.01$) the average maximum blockage in the symmetric tree is so low that any reduction would be inconsequential.

Analytics

To assess the accuracy of the analytic model developed in the previous section a comparison to the monte carlo simulation must be made. The nature of the calculation performed previously suggests that the blockage will be systematically overestimate. This is due to the

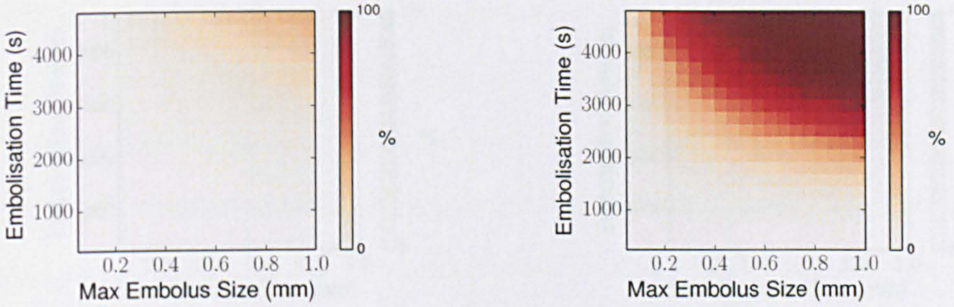

(a) $\tau = 0.001\mathrm{s}^{-1}$ (b) $\tau = 0.01\mathrm{s}^{-1}$

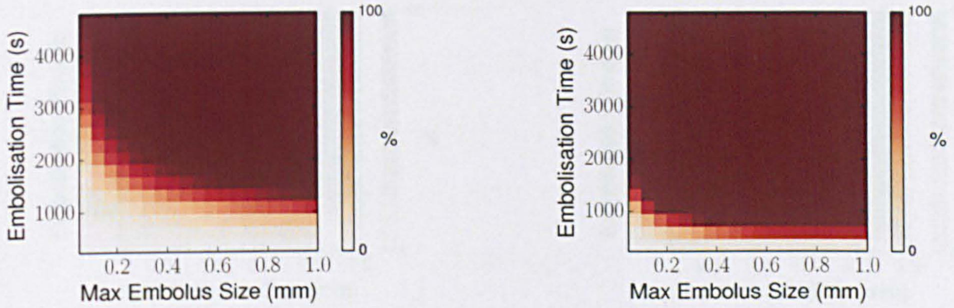

(c) $\tau = 0.1\mathrm{s}^{-1}$ (d) $\tau = 1\mathrm{s}^{-1}$

Figure 5.9: Average maximum blockage over 100 iterations of the monte carlo stroke model using a symmetric tree. In comparison to the simulations performed on the generated tree (Fig. 5.10) there is overall increase in the level of expected blockage.

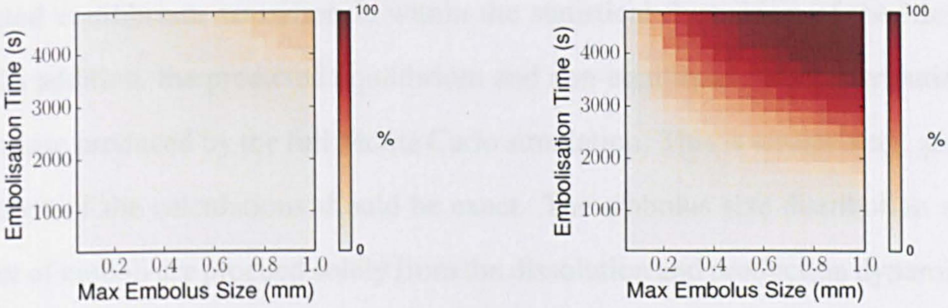

(a) $\tau = 0.001\mathrm{s}^{-1}$ (b) $\tau = 0.01\mathrm{s}^{-1}$

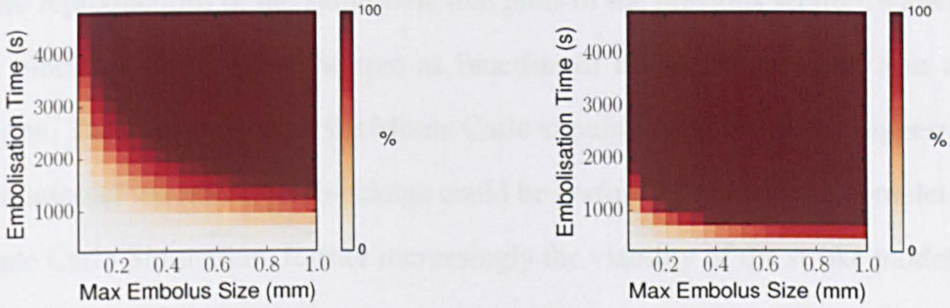

(c) $\tau = 0.1\mathrm{s}^{-1}$ (d) $\tau = 1\mathrm{s}^{-1}$

Figure 5.10: Average maximum blockage over 100 iterations of the monte carlo stroke model using the generated tree. In comparison to the symmetric tree used in Fig. 5.9 there is an overall reduction in the total amount of expected blockage.

assumption that blockages in each level block independent numbers of end nodes, neglecting the "shadowing" effect where newly introduced emboli block bifurcations proximal to previously established blockages. In addition, due to the method of calculation, the blockage fraction reported in the analytical model can be higher than 1, which is clearly incorrect. To compensate, blockage fractions greater than 1 are considered to be fully blocking, and are scaled back to 1 in the following results. Integrating this equation from 0 to

The predicted equilibrium saturation is within the statistical fluctuation of the Monte Carlo model. In addition, the predicted equilibrium and non-equilibrium size distributions closely match those produced by the full Monte Carlo simulation. This is unsuprising, given that these sections of the calculations should be exact. The embolus size distribution and average number of emboli are procued solely from the dissolution and production dynamics, which are controlled precisely by α and τ respectively.

Fig. 5.11 are reproductions of the symmetric tree plots of the previous section, showing the maximum blockage occuring in the tree as function of maximum embolus size and embolisation time. The agreement with the Monte Carlo simulation is very good, suggesting that a fast calculation of the maximum blockage could be performed prior to the completion of the full Monte Carlo Simulation, further increasingly the viability of the stroke model as a real-time clinical tool. While the accuracy of the analytical model in comparison to the symmetric tree simulations is good, the agreement with the generated tree is not. This is clearly a result of the symmetric tree used in the formulation of the analytic model.

5.3.8 Discussion

The results of the monte carlo stroke simulation for the symmetric model are as would be expected from the work of Hague *et. al*[26, 45, 46]. There is a clear transition from low to maximum blockage at high embolisation rates for simulations performed on both the symmetric and generated trees. For the generated tree, the location of this transition is

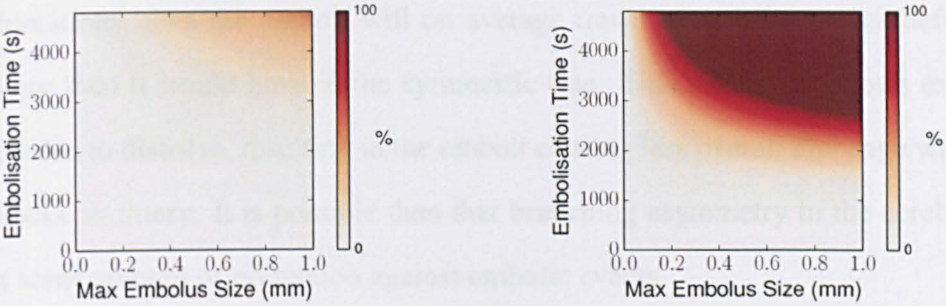

(a) $\tau = 0.001\text{s}^{-1}$ (b) $\tau = 0.01\text{s}^{-1}$

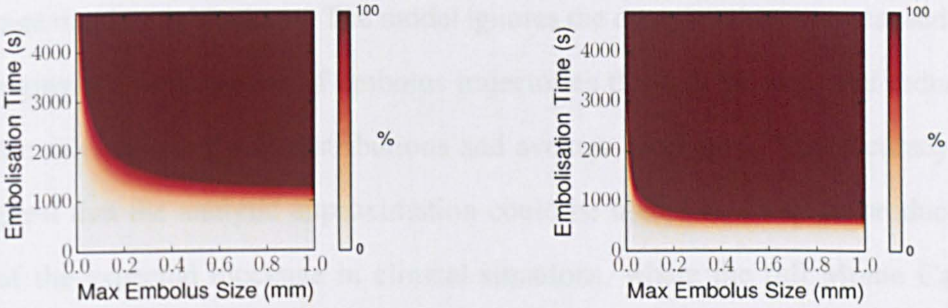

(c) $\tau = 0.1\text{s}^{-1}$ (d) $\tau = 1\text{s}^{-1}$

Figure 5.11: Average maximum blockage for the analytic stroke model for various embolisation rates (τ). In comparison to the equivalent monte carlo simulations the analytic approximation performs well.

shifted towards lower levels of blockage with respect to the symmetric tree. The number of bifurcations, terminal and root radii are the same for each tree, and so the difference in blockage can only be ascribed to the level of branching asymmetry present in the generated tree.

A highly asymmetric bifurcation will cause a representative fraction of emboli to take trajectories which follow the path of the larger daughter. If this asymmetry is present at subsequent bifurcations, then the emboli will on average travel more bifurcations before blocking an artery than it would have in the symmetric tree. This difference allows extra time for the embolus to dissolve, resulting in the emboli causing less overall blockage when it eventually blocks an artery. It is possible then that branching asymmetry in the cerebral arteries affords some amount of protection against embolic events.

The analytic approximation to the full monte carlo stroke simulation accurately reproduced the average maximum blockage. The model ignores the complex dynamics caused by blockages changing the probabilities of embolus trajectories through the tree, and reduces the model to the calculation of size distributions and average blockages. The accuracy of the results suggest that the analytic approximation could be useful as a tool to produce a fast estimate of the expected blockage in clinical situations, where the full Monte Carlo simulations may be innappropriate due to time scales of the simulations.

The difference in maximum average blockage between the generated and symmetric trees suggests that in models of cerebral embolisation the branching asymmetry of the cerebral tree must be taken into account; or at least that the results of simulations performed on symmetric trees must be presumed to overestimate the total amount of blockage.

As mentioned previously, the presumption that emboli follow a linear flow weighting trajectory becomes invalid in the presence of highly asymmetric branching. In this case, emboli will preferentially flow into the larger daughter above what would be expected given a linear flow weighting. With respect to the current model, this suggests that the effect of asymmetry are being underrepresented, and it is possible that an improved fluid dynamic or semi-empirical model may produce more pronounced differences.

5.4 Summary

In this Chapter the arterial generation algorithm was applied to the cerebral vasculature. The morphometric comparison of the MCA was good, but the PCA and ACA were less accurate than expected. The vascular territories of the identified major cerebral arteries in the generated trees roughly corresponded to experiment.

The generated vasculature was then used in a statistical model of embolic stroke, and the results were compared with the previously used symmetric tree model. The results of simulations suggested that branching asymmetry in the cerebral arterial tree may reduce arterial blockage during embolic events. In addition, the computational efficiency of the stroke model was vastly improved via algorithmic improvements.

An analytic approximation to the stroke model was derived and its results compared with that of the full Monte Carlo simulation. The analytic approximation produced results with a high degree of accuracy.

Chapter 6

Theory Chapter

6.1 Introduction

Previous chapters dealt with the computational generation of arterial trees using a novel, global optimisation technique. This technique relied upon the use of a radius-flow relationship of the form $q \propto r^{\gamma}$, where q is the volumetric flow and r is the radius of an arterial segment. When generating both coronary and cerebral arterial trees the value of γ was taken from the literature as a single value which best represented the real bifurcation exponent in the radius range of interest. In living systems, as was shown in Chapter 2, the bifurcation exponent is not constant and instead varies as some function of the radius. The factors causing this variation, and the resulting effects it has on the structure of the arterial tree, are not well understood. In this chapter we will provide a theoretical analysis of the optimal bifurcation exponent for a symmetrically bifurcating tree. In contrast to the work of Murray[94] and others[52, 98, 143, 149, 153], this analysis is performed on an entire tree, rather than a single arterial segment. To further explore the effect of the bifurcation exponent on the structure of arterial trees, we will use the previously developed algorithm to generate arterial trees for various exponent values.

6.2 The Symmetrically Bifurcating Tree

In Murray's analysis the optimal exponent for a single arterial tree segment, based upon the minimisation of volume and viscous power dissipation, was calculated and found to be equal to 3.0. While his analysis, and the subsequent work performed by other authors, was sound, it was performed on an arterial segment in isolation from its environment. An arterial tree is a connected set of arterial segments such that changes in any single segment are felt in the rest of the tree. For instance, in an occlusion event such as embolic stroke, the distal and proximally connected arteries to the event suffer a reduction in pressure and flow, and all other arteries experience an increase. This connectedness suggests that in order to fully understand the branching behaviour of arterial trees, the entire tree must be taken into account.

Following the work of Murray, we begin by writing the energy cost equation for a single arterial tree segment experiencing Poiseuille flow:

$$E = m_b \pi r^2 l + \frac{8\mu Q^2 l}{\pi r^4} \tag{6.1}$$

Where m_b is the metabolic power cost of blood, r is the segment radius, l its length, Q its volumetric flow and μ the dynamic viscocity of blood. The total cost of an arterial tree will be the sum of these individual segment costs. For an arterial tree consisting of n_T segments labelled i we write the total cost C_T as:

$$C_T = \sum_{i=1}^{n_T} \left(m_b \pi r_i^2 l_i + \frac{8\mu Q_i^2 l_i}{\pi r_i^4} \right) \tag{6.2}$$

In a symmetrically bifurcating tree it is possible to group "layers" of arteries together, so that each layer comprises arteries with similar properties (e.g length, diameter, flow). The symmetric tree has the advantage, in terms of analysis, that each of of the segments in a layer exist at the same bifurcation level. In a real arterial system, this would not be true, but it would still be possible to group arteries with similar lengths, radii and flows together. In the symmetric tree each layer has 2^i segments, where i is the number of bifurcations which occured before that layer ($i = 0$ at the root segment). We can now rewrite the cost function so that the sum now runs over the layers in the tree:

$$C_T = \sum_{i=1}^{n} 2^i \left(m_b \pi r_i^2 l_i + \frac{8\mu Q_i^2 l_i}{\pi r_i^4} \right) \tag{6.3}$$

Where i now refers to a particular layer rather than a segment. For a real arterial tree, which will not be perfectly symmetric, the 2^i term must be replaced by a function $N(r,l,q)$ which gives the number of arterial segments with similar radii, lengths and flows. n determines the depth of the arterial tree, or the maximum number of bifurcations experienced along a path from the root to an end node. What is left now is to determine the lengths, radii and flows at layer i in the symmetric tree. We begin by noting that, since the tree is symmetric, a bifurcation will split the flow in the parent artery evenly between the two daughters, so that:

$$Q_i = Q_0 2^{-i} \tag{6.4}$$

Where Q_O is the flow in the root segment of the arterial tree and Q_i the flow in the segments of layer i. This is a clear consequence of the continuity equation, but is valid only for symmetric trees. For asymmetrically bifurcating trees, as is the case in living systems, the picture is much more complicated.

To derive an expression for the radii in layer i of the symmetric tree we begin with the radius-flow relationship:

$$Q_{i,i+1} \propto r^{\gamma_i} \tag{6.5}$$

Where $Q_{i,i+1}$ are the flows in layer i and $i+1$, and γ_i is the bifurcation exponent associated with the bifurcation distal to layer i. This allows us to write the following expression, analogous to the one derived by Murray, for the bifurcations leading to the segments in layer i of the tree:

$$r_{i+1} = 2^{-\gamma_i^{-1}} r_i \tag{6.6}$$

Using this equation it is possible to write the radius r_i of the segments in layer i of the tree in terms of the root radius r_0:

$$r_i = 2^{-\sum_{j=1}^{i} \gamma_j^{-1}} r_0 \tag{6.7}$$

Here it has been assumed that the bifurcation exponents γ_i are independent at each bifurcation layer of the tree. In Murray's derivation a single optimal exponent was found and thought to goven the bifurcations of the entire arterial tree, and in later sections we will investigate the effects of fixing the bifurcation exponent to a constant value, however to begin we will operate on the assumption that they remain independent.

The final unknown in the cost equation are the lengths of arterial segments in layer i of the tree. Experimental data suggest that the length of an arterial segment is proportional to some power of the radius, $l_i \propto r_i^{\alpha}$, where the value of the exponent α has been found to be very close to 1.0[62]. The equation for the length l_i of an arterial segment in layer i of the tree can then be written as a function of the radius r_i:

$$l_i = \left(\frac{r_i}{r_0}\right)^{\alpha} l_0 \tag{6.8}$$

Where l_0 is the length of the root segment of the tree. We are now in a position to rewrite Eq. 6.3 in terms of the derived expressions for radius, length and flow. Inserting Eq 6.4, 6.7, and 6.8 into Eq 6.3 we find:

$$C_T = \sum_{i=1}^{n} \left(c_1 2^{-\phi_i} + c_2 2^{\phi_i}\right) \tag{6.9}$$

Where $c_1 = m_b \pi r_0^2 l_0$, $c_2 = \frac{8\mu Q_0^2 l_0}{\pi r_0^4}$, and $\phi_i = 3\left(\sum_{j=1}^{i} \gamma_j^{-1}\right) - i$. This is the energy cost for a symmetric tree consisting of n bifurcation levels. It is expressed purely as a function of the layer number i and the value of the bifurcation exponent at that layer γ_i. Given this equation, we are now in a position to calculate the optimal bifurcation exponents which minimise the cost function of the symmetrically bifurcating tree.

6.3 Optimal Bifurcation Exponent

In the previous section we derived a simplified cost function for the symmetric bifurcating tree (Eq 6.9). In deriving an expression for the radii at level i in the tree, the bifurcation exponents γ_i were taken to be independent of one another so that the radii of segments in level i are given by Eq 6.7. While this may be a valid choice, experimental data suggests that the bifurcation exponent holds some functional dependence on the radii involved in the bifurcation[112]. To begin with however, we will calculate the optimal exponent values for the case where each γ_i is independent.

6.3.1 Independent γ_i

Since in this case the γ_i are independent of one another, we can assume that each level of the tree achieves its own optimum with respect to the cost function. In precise terms we may take the partial derivative of the cost function with respect to γ_k and set it equal to 0, then solve for γ_k. The derivative of the cost function with respect to γ_k is given by:

$$\frac{\partial C_T}{\partial \gamma_k} = 3\gamma_j^{-2} \sum_{i=k}^{n} \left(-c_1 2^{-\phi_i} + c_2 2^{\phi_i}\right) \tag{6.10}$$

Here we have made use of the fact that since $\phi_i = 3\left(\sum_{j=1}^{i} \gamma_j^{-1}\right) - i$, the sum terms in the cost function with $i < k$ will not contribute, so that the sum runs from k to n. To find the minimum we set the partial derivatives equal to zero and note that the expression for the partial derivative with respect to $\gamma_n$is:

$$c_1 2^{-\phi_n} - c_2 2^{\phi_n} = 0 \tag{6.11}$$

Solving for ϕ_n, substituting the full expression and rearranging we find that:

$$\sum_{j=1}^{i} \gamma_j^{-1} = \frac{1}{3}\left(\frac{1}{2}\frac{\log\frac{c_1}{c_2}}{\log 2} + i\right) \tag{6.12}$$

Which can be easily solved to give an optimum value of 3 for γ_i when $i > 1$ and equal to:

$$\gamma_1 = 3\left(\frac{1}{2}\frac{\log\frac{c_1}{c_2}}{\log 2} + 1\right)^{-1} \tag{6.13}$$

This is in contrast to Murray's law which states that the bifurcation exponent should be 3 in all bifurcations, regardless of position in the tree. The difference can be explained by noting that in Murray's derivation the optimal radius-flow relationship is derived for a single arterial segment, and then this rule is used in the continuity equation to find an expression governing the arterial diameters in a bifurcation. In this derivation, the root node flow and radius were not assumed to have any particular relation to one another. The optimal radius flow relationship as derived via Murrays law is given by:

$$Q_0^2 = \frac{m_b \pi^2}{16\mu} r_0^6 \tag{6.14}$$

Using Eq 6.14, one finds that $\frac{c_1}{c_2} = 2$ and so Eq. 6.13 recovers Murray's law throughout the entire tree i.e a γ value of 3 throughout the entire tree. It seems then that deviation from Murray's law in the root segment of the tree generates a corresponding deviation in the first bifurcation, with regards to the optimal exponent value. This makes sense from an optimisation perspective, in so far as the first bifurcation is likely to have the smallest overall impact on the cost function. The number of arterial segments grows as 2^i with the layer number i, and since the viscous dissipation grows as $1/r_i^4$ it is likely that the later layers in the tree will make comparatively large contributions to the cost function.

While it may seem strange to perform an analysis which differs appreciably from Murray's law only when the root bifurcation has a suboptimal radius-flow relationship, there are a few reasons why this may important. The first is that there may be physiological situations which demand a divergence from the optimal radius-flow relationship, which must be later "recovered" by the rest of the tree. For instance, measurements of the bifurcation exponents in the largest arteries of the human body have shown a significant deviation from the exponent values predicted by Murray[108]. These deviations have been attributed to elastic arterial wall effects[97], pulsatile flow[5] and turbulence[125]. While the exact mechanism of the deviation may be unknown, the recovery of Murray's law in the smaller arterioles[114] suggests that its effect diminishes far from the heart. As such, there will be instances where near laminar flow is supplied into a tree segment from an arteriole which does not have the correct radius-flow relationship. The second is that it allows us to examine the optimality of various bifurcations under the assumption of laminar flow conditions.

The analysis of arterial bifurcation exponents can now be peformed with reference to the morphometry of the parent artery. Previously comparison would be against either Murray's law, or one of the other theoretical derivations performed on single arterial segments[156]. All comparison methods of this form have the same fault, in that they presuppose the parent artery has some fixed radius-flow relationship and asses the bifurcation exponent starting from this assumption. The general method is to measure the 3 radii involves in the bifurcation and then perform a linear regression to fit the radii to the equation:

$$r_p^\gamma = r_{c1}^\gamma + r_{c2}^\gamma \tag{6.15}$$

The fitted γ value is then compared to the theoretically optimal value. If the radius-flow relationship in the parent artery differs from that predicted by the theory, then so will the

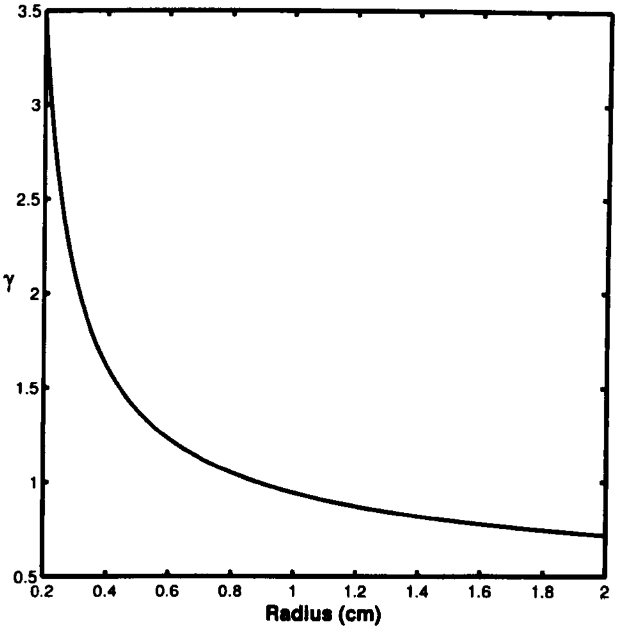

Figure 6.1: The optimal bifurcation exponent for bifurcations with parent arteries having a $Q \propto r^2$ relationship. As the radius of the artery increases the optimal γ value decreases. Typically, the carotid artery has a radius of approximately 0.3cm. Experimental data shows the carotid bifurcation to have an exponent value of ≈ 1.6 [97]

theoretically optimal bifurcation exponent. In this case, comparison of the measured exponent value with, for the case of laminar flow, Murray's exponent value, is meaningless. In order to make a true comparison the morphology of the parent artery must be taken into account.

In fact, if the objective is a comparison of experimental data with the prediction of Murray's law, then calculations of Eq 6.15 are undesireable. Instead where possible both the radius and volumetric flow in the artery should be measured. This allows a direct calculation of the radius-flow relationship, and so a direct comparison to the prediction of Murray's law without the issues outlined in the previous paragraphs.

6.3.2 Constant γ

We now look at the case of a constant γ value throughout the entire tree. This case is particularly relevant for the study of optimisation algorithms for arterial trees, such as CCO and the algorithm presented in this thesis, since they rely upon a fixed bifurcation exponent to set the radii in the generated trees. From the previous analysis it is clear that any significant deviation from a bifurcation exponent of 3 will result in a higher cost tree, but to what extent would depend on the morphometric properties of the root segment. Computationally generated trees often take the properties of the root segment as an input, where the values for diameter and flow are taken from experimental data. This means that the radius-flow relationship in the tree is not guaranteed to be the same as that suggested by the chosen bifurcation exponent.

For constant γ it is possible to make the susbtituion $\gamma_i = \gamma_n$ in the right hand side of Eq. 6.10. In this case, all derivates dissapear except for $\frac{\partial C_T}{\partial \gamma_n}$, which can be set equal to zero and solved for γ to give:

$$\gamma = 3\left(\frac{1}{2n}\frac{\log\frac{c_1}{c_2}}{\log 2}+1\right)^{-1} \tag{6.16}$$

This solution is almost identical to the expression given for the first bifurcation in the case of independent γ, except for the factor of $\frac{1}{n}$ in the first term of the right hand side. This factor is again a result of the larger cost contributions of the later levels in the tree. The $\log\frac{c_1}{c_2}$ term is entirely the result of the root segment morphology, but for large trees the $\frac{1}{n}$ term ensures its effects are barely felt. In the case of very large n, the effect of the root segment is largely negated, and for infinite n Murray's result is once again recovered (i.e $\gamma = 3$ for any root segment morphology).

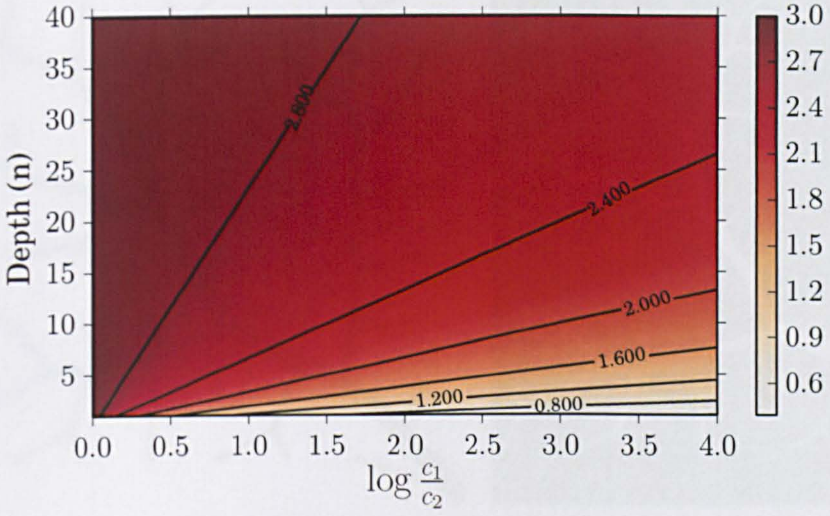

Figure 6.2: Optimal bifurcation exponent as a function of $\log \frac{c_1}{c_2}$ and tree depth n. As n increases the optimal exponent value approaches 3, however this approach is slowed for large values of $\frac{c_1}{c_2}$. This indicates that the optimal bifurcation exponent may depend on the specific configuration of the input artery for arterial trees in living organisms.

6.4 Properties Of Generated Trees

In this section an investigation of the unexplored parameter space of the arterial generation algorithm is performed. The results of the previous section are also compared against the results obtained for generated trees; specifically the optimal bifurcation exponent for the generated trees is assessed and compared to the theoretical value. The fractal dimensions of the generated trees are calculated using the box counting method, and their value assessed as a function of both the bifurcation exponent and the boundary conditions of the generation algorithm.

6.4.1 Box Counting Method

In order to estimate the fractal dimension of the generated vasculatures, the method of box counting was employed. Trees generated by the algorithm are first rendered as two dimensional images. The tree is viewed from above and the image is cropped to minimize white

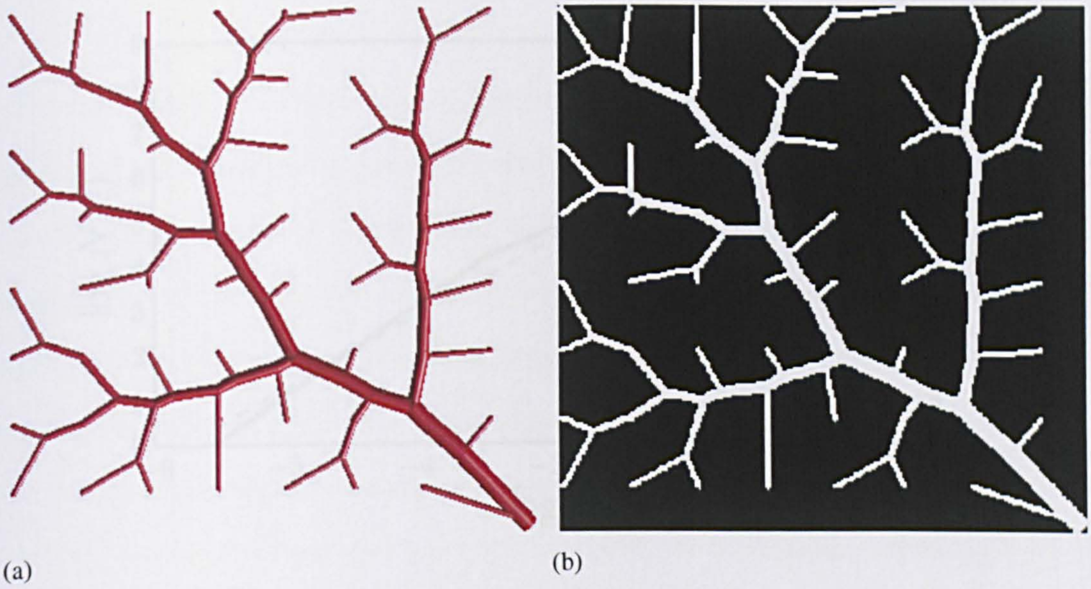

Figure 6.3: On the left is an image of a generated tree as viewed from above, cropped to minimize whitespace. On the right is an example of a thresholded image of the generated trees, converted to a binary format.

space (See Fig. 6.3(a)). The resulting image is then converted to binary form so that pixels belonging to the tree are colored white and empty space is colored black e.g Fig 6.3(b). After this process, the images are then processed using the box counting method.

The method itself estimates the fractal dimension of an image by dividing it into boxes of size ε. If the box contains an occupied pixel of the image then it is counted, and the sum of this count is determined for the entire image. For boxes of size ε the count of boxes countaining an occupied pixel is $N(\varepsilon)$. The estimate of the box counting dimension for an image S, at box size ε is then given as:

$$\mathrm{dim_{box}}(\mathrm{S},\varepsilon) = \frac{\log N(\varepsilon)}{\log \frac{1}{\varepsilon}} \tag{6.17}$$

The box size is then changed, and the process is repeated. The values obtained are then plotted, and the gradient of a linear fit is extracted to give an estimate of the box counting dimension (See Fig. 6.4). For well behaved fractals, the box counting dimension is exactly

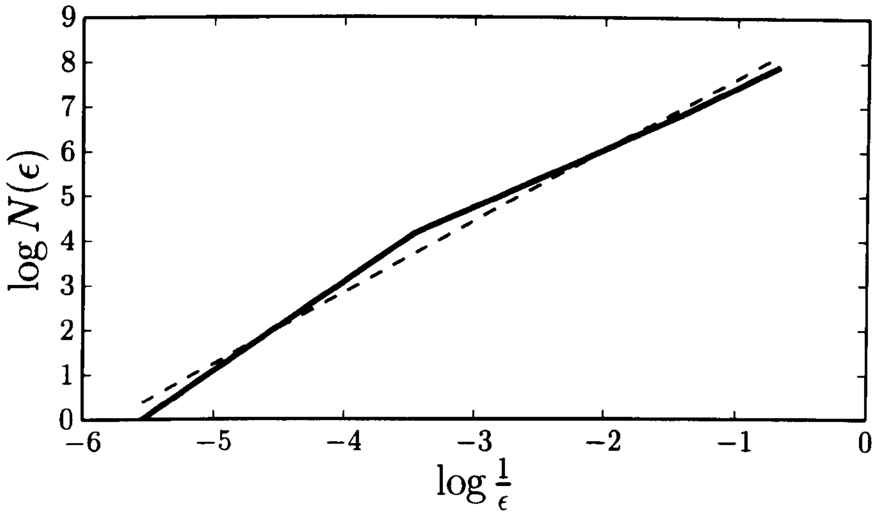

Figure 6.4: $\log N(\varepsilon)$ vs $\log \frac{1}{\varepsilon}$ for the example tree of Fig. 6.3(b). The dashed line represents the first order fit. The box counting dimension is calculated as the slope of the fitted line.

equal to the Hausdorff dimension, however in general they are related by the inequality[44]:

$$\dim_{\text{Haus}} \leq \dim_{\text{box}} \tag{6.18}$$

The calculated box counting dimension then also sets an upper limit for the Hausdorff dimension. The box counting dimension has the benefit of being the same quantity as that calculated for images of *in vivo* arterial trees, allowing for a direct comparison to experimental data.

6.4.2 Results

The fractal dimension of an arterial tree is a measure of its structure. To characterise the effect of a changing bifurcation exponent on the structure of an optimised arterial tree, the fractal dimension can be measured. The algorithmn developed in earlier chapters can be used to generate arterial trees in the 2D plane. The fractal dimension of these arterial trees can then be calculated via the box counting method outlined in the previous section.

For each value of the bifurcation exponent and metabolic constant values 5 arterial trees consiting of 1024 nodes were generated. The size of the geometry was 10cm by 10cm and the root node had a radius of 1mm and input flow of $5 \times 10^{-6} m^3 s^{-1}$. The optimisation geometry was confined to the 2D plane, but within it there was no node exclusion. A sample of the trees produced at each bifurcation exponent and metabolic constant values are presented in Fig. 6.5. The effect of changes in the metabolic constant are quite dramatic at the lowest values of the bifurcation exponent, but become less apparent at higher values. There are obvious structure changes occuring as the bifurcation exponent changes at all values of the metabolic constant, with higher values being generally associated with shorter segments and more symmetric branching.

In Fig. 6.6 we show the calculated fractal dimension for the generated trees. While there is a significant difference in the appearance of the trees generated for $\gamma = 2$ at each value of the metabolic constant, the difference in the fractal dimension at this γ values is minimal. This suggests that the bifurcation exponent has a much stronger on the fractal structure of the tree than the metabolic constant. Experimental data show that the human retinal arterial tree has a fractal dimension of 1.7 [82], and the renal arterial tree a fractal dimension of 1.61 [30]. Since it is unlikely that a measurement of the branching exponent in the renal arterial tree would yield a value less than 2, it appears as though the results of the 2D simulation can not be applied to three dimensional arterial trees. However, measurements of the retinal arterial tree bifurcation exponent yield a value of 2.65 ± 0.18[82], which aligns with the fractal dimension given the current algorithm. It appears then that the basic 2D simulation is enough to capture the important aspects of the retinal arterial tree.

In Fig. 6.7 the generated trees have been altered so that the total number of bifurcations is 128 and the end nodes lie on evenly spaced grid points. In addition, the fractal dimension has been calculated over a wider range of bifurcation exponents and for different values

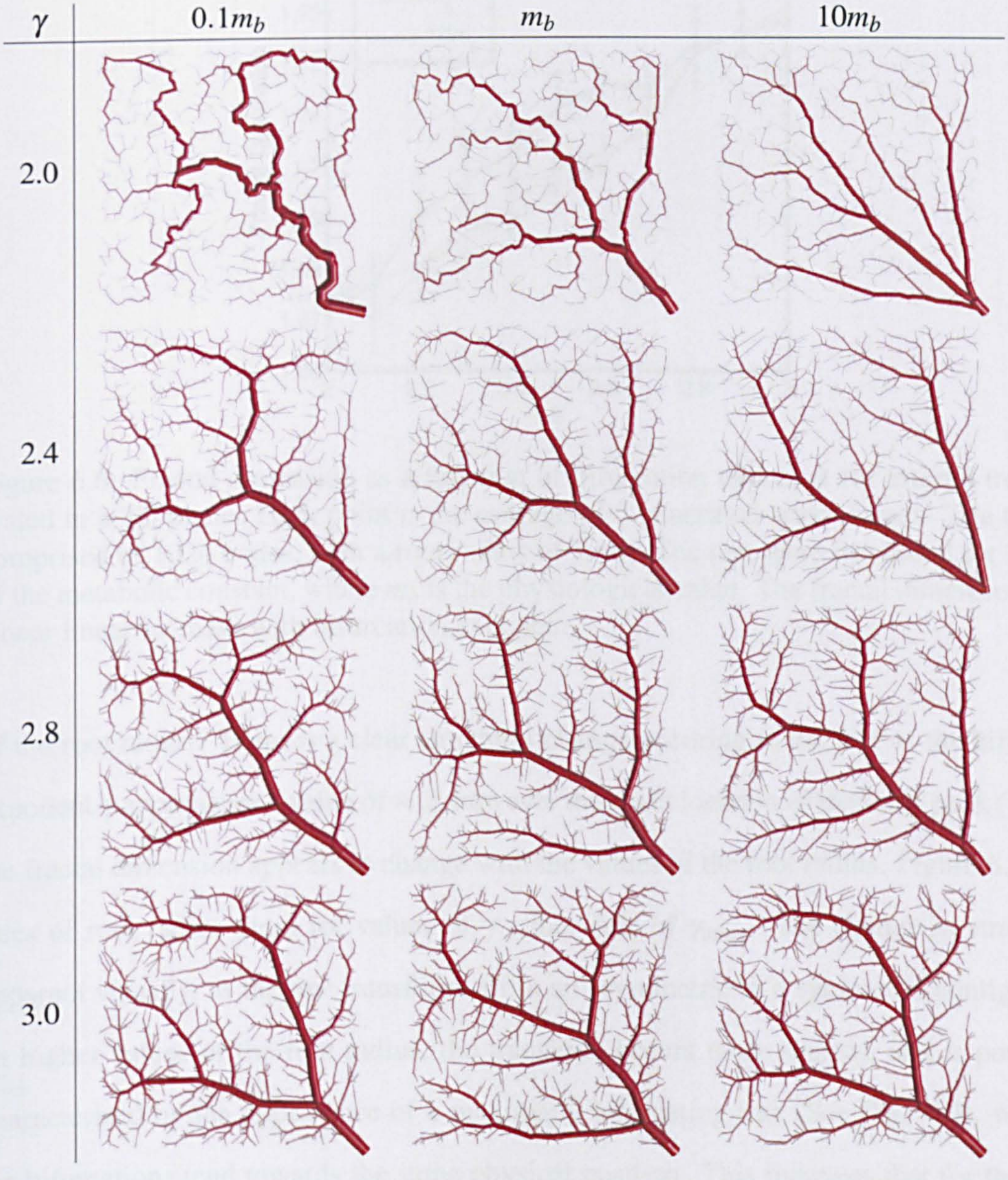

Figure 6.5: Example trees generated for various values of the m_b and γ. While there is a large visual difference in the structure of the tree for $\gamma = 2.0$ at various metabolic constant values, the change in fractal dimension is relatively small. The fractal dimension of the tree should thus be relatively constant over a variety of length scales, for a fixed bifurcation exponent.

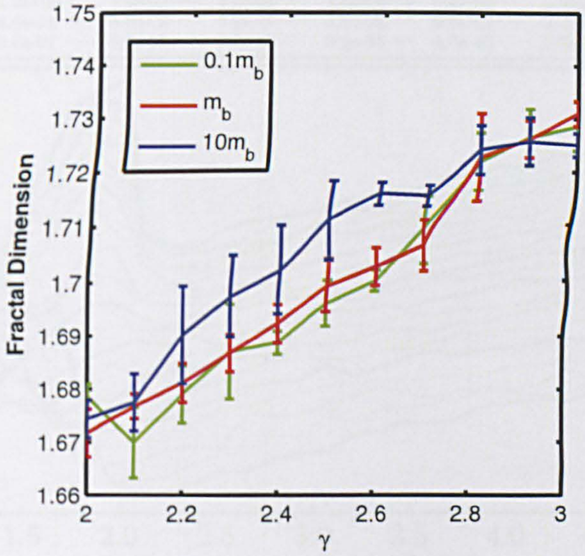

Figure 6.6: Fractal dimension as a function of bifurcation exponent for arterial trees generated in a 2D plane. Each point is the average of 5 generated arterial trees. The trees are comprised of 1024 nodes, with a root radius of 1mm. The tree were generated for 3 values of the metabolic constant, where m_b is the physiological value. The fractal dimension shows a near linear increase with bifurcation exponent.

of the root radius. There is a clear structural change occuring in the tree as the bifurcation exponent γ approaches a value of ≈ 2, however the exact location of the local peak (γ_{trans}) of the fractal dimension appears to change with the values of the root radius. Figure 6.8 shows trees of root radius 1mm for values of γ either side of γ_{trans}. The change in structure is apparent visually, as the tree transitions from an asymmetric to a symmetric configuration. At higher values of the root radius, the transition occurs more sharply, and is potentially characterised by the appearance of a maximally bifurcating tree (See Fig. 6.9), where all the bifurcations tend towards the same physical position. This indicates that for the length scale of the tissue sample considered, the specific values of γ, Q_0 and r_{root} cause the terminal segments to be the energetic minimum no matter the length.

As γ tends towards 0, the tree structure becomes maximally asymmetric, with a single trunk artery snaking through each of the end node sites (See left panel in Fig 6.8). This is due to the rapid reduction in radius caused by symmetric bifurcations, which scales as

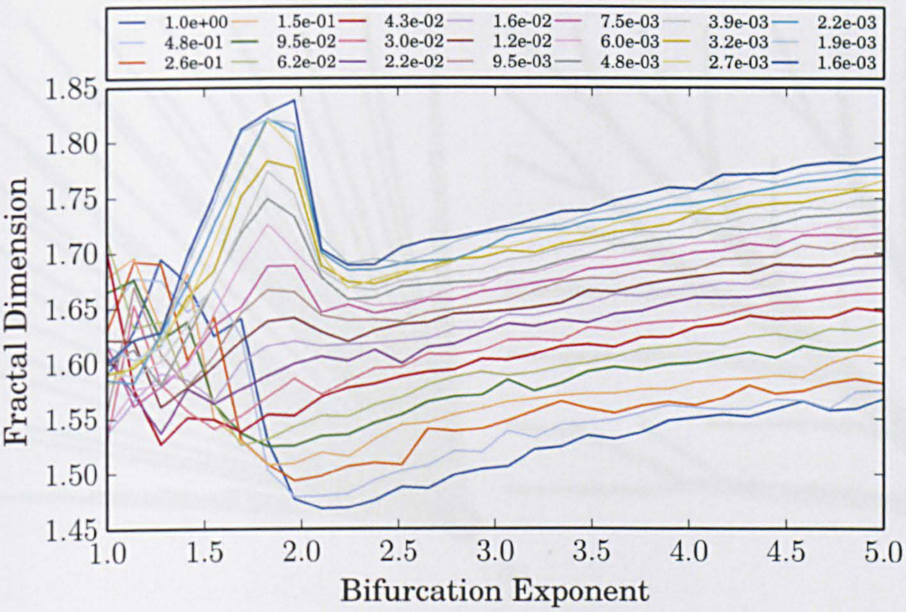

Figure 6.7: Fractal dimension calculated for 2D trees (terminal nodes place on grid sites). Each curve is for a specific value of $\frac{Q_0}{r_{\text{root}}^4}$, given in the legend. There is a clear anomaly at around $\gamma = 2$, where the structure of the tree changes significantly, though the exact location of the local peak of the fractal dimension changes as a function of the root radius.

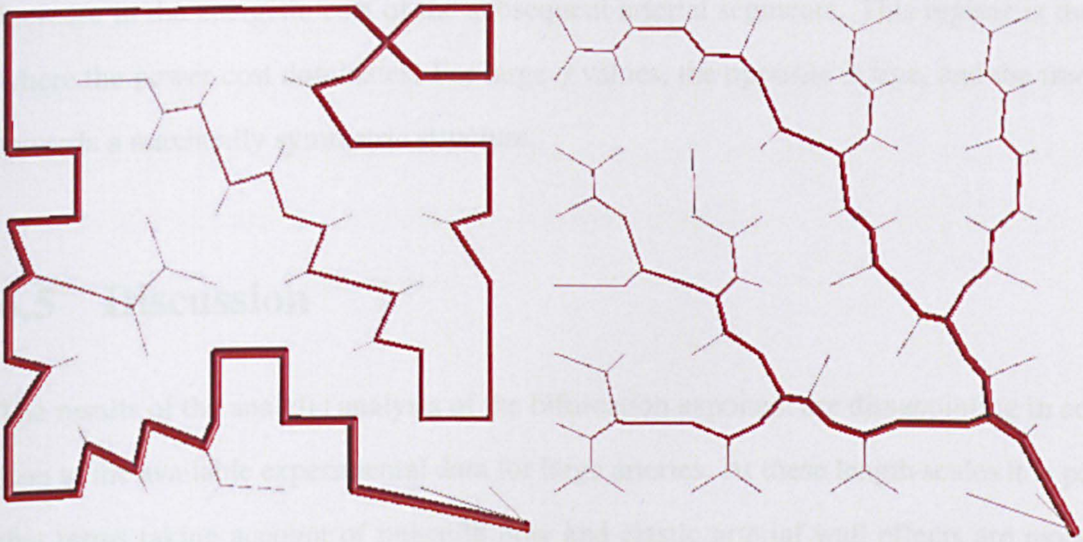

(a) (b)

Figure 6.8: Trees generated either side of γ_{trans} for a root radius of 1.1mm. There is a clear change in the structure of the tree. Left: $\gamma = 1.9$, Right: $\gamma = 2.1$.

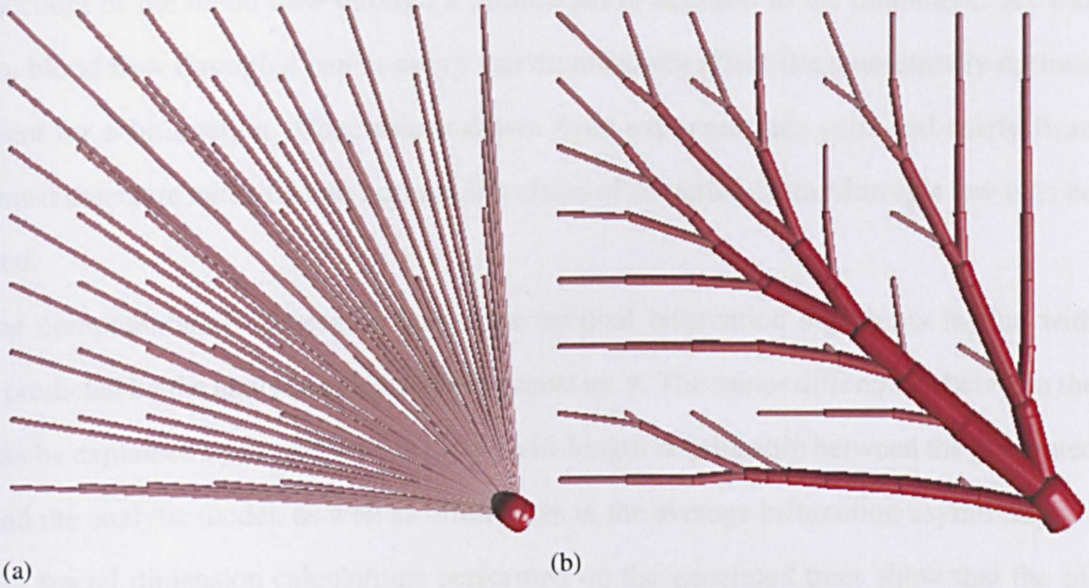

Figure 6.9: Trees generated either side of γ_{trans} for a root radius of 5mm. There is a clear change in the structure of the tree, where at values of γ just before the transition, the tree has taken a maximally bifurcating form. Left: $\gamma = 1.9$, Right: $\gamma = 2.1$.

$2^{-\frac{1}{\gamma}}$. Since the power cost scales as r^{-4}, for small γ a symmetric bifurcation causes a large increase in the energetic cost of the subsequent arterial segments. This regime is then one where the power cost dominates. For large γ values, the opposite is true, and the trees tend towards a maximally symmetric structure.

6.5 Discussion

The results of the analytic analysis of the bifurcation exponent are dissapointing in comparison to the available experimental data for large arteries. At these length scales it is possible that terms taking account of pulsatile flow and elastic arterial wall effects are required in the energetic cost function, however inclusion of these terms would potentially exclude the possibility of a closed form solution. For smaller arteries the results are inline with those found in the literature, that is that the optimal bifurcation exponent is close to 3. It is clear from the analysis that experimental investigations of deviations from Murray's law must take account of the blood flow through a bifurcation in addition to the diameters. As was shown, blood flow through a parent artery can dramatically affect the theoretically optimal exponent for a bifurcation. Conclusions drawn from exponent data extracted solely from radii must therefore take this into account if a claim of deviation from Murray's law is to be asserted.

The computationally generated trees have optimal bifurcation exponents in line with those predicted by the analytic calculation for constant γ. The minor differences between the two can be explained by the difference in the radii-length relationship between the generated tree and the analytic model, as well as differences in the average bifurcation asymmetry.

The fractal dimension calculations performed on the generated trees show that the bifurcation exponent is the most dominant factor in controlling the overall structure of the tree. That the fractal dimension of the generated trees can be used to correctly predict the bifurcation exponent of the retinal arterial tree is further confirmation of the validity of the arterial generation algorithm. The generation of a full three dimensional renal arterial tree with subsequent fractal dimension analysis and comparison to experimental data would provide further validation of the model. The striking change in structure which occurs suddenly as a result of changes in the bifurcation exponent suggests that arterial trees with exponents either side of this transition possess a fundamental difference. The exact details of this difference warrant further investigation.

6.6 Summary

In this chapter I have developed an extension to Murray's law which provides an analytic expression for the optimal bifurcation exponent of an entire symmetric arterial tree. The model is developed to take account of both independent values of γ and a constant value throughout the tree.

The parameter space of the generated arterial tree was more fully explored by the analysis of trees generated with end nodes placed upon grid points. The asymmetry parameter, optimal exponent value and fractal dimension of the generated trees were calculation and the implications of their values discussed.

Chapter 7

Conclusions and Future Work

In this chapter I summarise the main results of the thesis and their implications, as well as discuss possible future avenues of research and possible applications of the algorithm developed in this work.

7.1 Conclusions

A fundamental goal of this thesis was to develop a simple, global optimisation algorithm capable of generating large scale arterial trees for complex geometries derived from medical imaging. While this target was successfully achieved, the cerebral vasculatures generated by the algorithm were lacking in both morphometric and structural accuracy. Possible reasons for this were detailed in the discussion section of Chapter 5, and in the following sections various future modifications and extensions to the algorithm will be discussed. In some cases these changes represent overall improvements to the algorithm (e.g more accurate fluid dynamics) which may become feasible as computational power increases, or be currently applicable for arterial trees with small numbers of bifurcations.

7.1.1 Global Optimisation Algorithm

This thesis developed a simple, physiologically based model of arterial tree which could be entirely framed as an optimisation problem. In previous models such as constrained constructive optimisation (CCO), the inclusion of complex geometries necessitated the addition of ad-hoc rules which were separate to the optimisation; in contrast, the algorithm developed in this thesis produces arterial trees purely from optimisation principles. In addition, to the knowledge of the author, the algorithm developed in this thesis is the first to allow for the possibility of a globally optimal solution to be reached, and as a result is the first to produce arterial trees with a consistent arterial structure when provided with different starting conditions (random number seeds).

At the time CCO was first developed the available computational power dictated its construction: it was not possible to globally optimise trees of appreciable size given the existing hardware. The decision to produce an iterative algorithm was deliberate, and the consequences were discussed in the original paper of Schreiner *et. al*[118]. Since then, the decision does not appear to have been reconsidered publicly outside of the current work.

While the development of an algorithm which can produce globally optimal arterial trees is interesting in its own right, without validation against arterial trees of living organisms it would have limited applications.

7.1.2 Coronary Vasculature

In Chapter 4 the arterial generation algorithm was used to produce arterial trees for a simplified ellipsoidal model of the human heart. The results of the simulation were compared both morphologically and visually with *in-vivo* data. The morphological results represent an improvement vs those previously achieved by optimisation methods, but perhaps the more striking result was the consistely correct positioning of the larger coronary arteries. This suggests that the evolutionary pressure towards energy minimisation was a large driving force in the organisation of the coronary vasculature in adult humans. While this may previously have been assumed to be the case, it is difficult to imagine a more convincing demonstration of its validity.

7.1.3 Cerebral Vasculature

The results obtained for the cerebral vasculature are less impressive than those of the coronary vasculature. The mophometric and visual comparisons are less convincing, and this could be due to a variety of reasons. The first and most obvious is that the brain may not have been subject to the same energy minimisation pressure as the heart. The heart can undergo large variation in blood flow due to exercise[32], and myocardial tissue requires a much higher level of blood flow than even grey matter. In addition, the large quantity of grey matter in the human brain evolved rapidly[99], and so may be less optimised as a result. Nevertheless, the cerebral trees produced by the algorithm are, to this authors knowledge, the first vasculatures to be generated in geometries obtained from medical imaging, purely using optimisation criteria. It may well be that this type of algorithm is innarppriate for the cerebral vasculature, however reaching this conclusion will take further work.

The complexity of the cerebral topology is yet another potential source of the model innacuracy. High levels of curvature in the folds of the brain, combined with a larger overall tissue volume than that found in the heart may also have contributed to the lack of morphological and structural accuracy.

7.1.4 Stroke Model

The stroke model was successfully extended to use trees derived from the arterial generation algorithm. As a side benefit, this will also allow for trees generated by other means (e.g extract from MRI imaging or generated from a morphological database) to be used with the stroke model. The result of changing from a perfectly symmetric to an assymetric arterial tree topology was that of a reduced level of cerebral ischeamia, suggesting that cerebral arterial trees with higher levels of branching symmetry are potential more at risk from stroke.

The performance of the stroke model was improved by three orders of magnitude for solid emboli and an order of magnitude for gaseous emboli, allowing for potential real-time clinical applications. In addition, an analytic approximation was developed which would be capable of providing instantaneous esimations of the potential arterial blockage.

7.2 Future Work

While the develop arterial tree model was adequate for the coronary vasculature grown on an ellipsoid model of the heart, it is clear that further work will be required if it is to be reliably applied to other organs, in particular the brain, and this is a clear focus for further development.

•

7.2.1 Cerebral Vasculature

If the cerebral vasculature is indeed vestigal to large degree then it will not be possible to generate accurate arterial trees using the algorithm presented in this thesis. However, in order to fully rule out the possibility it will be necessary to perform further computational experiments. The first and simplest to undertake is to generate trees for a large number of simulated annealing steps, for various numbers of nodes; this work is already underway.

The acquisition of either the raw data of Wright *et. al*[144] or new cerebral arterial tree data would be highly beneficial, so that an analysis in terms of diameter defined strahler order (as performed for the cerebral arterial tree) could be performed. This is preferable to the branching order categorisation performed by Wright *et. al* as it compensates for the potentially large variation in diameter of arteries assigned similar branching indices.

Another possible extention would be to assign 3 inputs to the arterial tree generation algorithm, and to fix the perfusion territories of these inputs so that they correspond to the middle, posterior and anterior cerebral arteries. This would undoubtedly improve the results of the algorithm but represents a significant deviation from its original intention; however, it is perhaps reasonable to assume that if there are vestigal effects present in the cerebral vasculature, that they would be found near the Circle of Willis. This was originally considered but was excluded in favour of a single input in order to allow for the potential to draw a definite conclusion regarding the optimality of the cerebral vasculature. Nonetheless, it is a worthy avenue of potential research.

7.2.2 Fluid Dynamics

An obvious extension to the current model would be to include higher order fluid dynamics, or at first to matain the current poiseuille dynamics but allow the terminal node flows to vary. The current algorithm is capable of the latter currently, however it was disabled early on the grounds of computational efficiency. However, the capability could be re-enabled and used to investigate the effect for smaller two dimensional trees (e.g the retina).

In order to allow for higher order fluid dynamics the calculations would certainly have to be parallelised extensively for use on a computing cluster. The number of simulated annealing steps required for even small trees necessitates this. An accurate fluid dynamics simulation performed on a tree optimised using the poiseuille flow equations would also be an interesting avenue of research, where the laminar flow assumptions could be more fully verified and perhaps the trajectory of individual emboli through the tree could be more accurately assessed.

7.2.3 Blood Supply

Currently the algorithmn employs the simplified “microvascular black box” formalism to associated tissue volumes to terminal sites in the generated tree. This implies that there is no crossflow between branches of the arterial tree, and that within a given radius all tissue is supplied with an equal amount of blood from a given terminal site. These assumptions are clearly incorrect, and lead to an overestimation of the number of a terminal sites (and blood flow) required to supply a given volume of tissue. A simple modification would be to replace the fixed radius of supply with a function which decays with distance away from the end node. The difficulty arises from determining the form of this function. Acquiring organ specific data documenting the volume of tissue associated with an arterial segment of given size, for a specific organ, would allow an empircal estimation of this blood supply function. The algorithm could then be modified to include it. Obtaining such data however would represent a significant research challenge, and there are certainly more immediately available improvements to be had.

7.2.4 Other Organs

This thesis explored only the vasculatures of two organs in the human body. Both the liver and kidneys have unique vasculatures that represent a potential application for the current algorithm. The major difficulty in this regard lie in obtaining extensive morphological data for the purpose of comparison. As a first step it would be possible to simply perform visual inspections against both vascular imaging data and the representative images presented in various textbooks, but this is far from rigorous and true validation will require detailed measurements.

7.2.5 Bifurcation Exponent

The analysis presented in Chapter 6 of the optimal bifurcation exponent for a symmetrically bifurcating tree is another area worthy of further investigation. The fluid dynamics included in the energetic cost function were again poiseuillian, and there were no further terms involving energy dissipation (such as pulsatile flow). The addition of further terms may lead to more complex behaviour of the optimal exponent as a function of arterial segment radius. Further analysis may also lead to solutions involving more complex functions, where in the analysis presented the variation of the exponent was limited only to completely indendent and constant values.

7.2.6 Stroke Model

The results of the stroke model simulation suggest that branching asymmetry could be an important factor in the assessment of damage likely to occur during an embolic event. The use of clinical embolus sizing data in conjuction with the more accurate cerebral vasculature represents the next steps in this avenue of research. In addition, the spatial correlation of blockages is yet to be fully analysed, and would allow the determination of whether branching asymmetry results in more tightly focussed volumes of blockage.

Bibliography

[1] Aarts, E., Korst, J., and Michiels, W. (2005). Simulated annealing. In *Search methodologies*, pages 187–210. Springer.

[2] Adhyapak, S. and Parachuri, V. (2010). Architecture of the left ventricle: insights for optimal surgical ventricular restoration. *Heart Failure Reviews*, 15(1):73–83.

[3] Amanatides, J., Woo, A., et al. (1987). A fast voxel traversal algorithm for ray tracing. In *Eurographics*, volume 87, page 10.

[4] Anderhuber, F., Weiglein, A., and Pucher, R. K. (1990). [Trifurcations of the middle cerebral arteries]. *Acta Anat (Basel)*, 137(4):342–349.

[5] Anor, T., Grinberg, L., Baek, H., Madsen, J. R., Jayaraman, M. V., and Karniadakis, G. E. (2010). Modeling of blood flow in arterial trees. *Wiley Interdisciplinary Reviews: Systems Biology and Medicine*, 2(5):612–623.

[6] Atochin, D., Murciano, J., Gürsoy-Özdemir, Y., Krasik, T., Noda, F., Ayata, C., Dunn, A., Moskowitz, M., Huang, P., and Muzykantov, V. (2004). Mouse model of microembolic stroke and reperfusion. *Stroke*, 35(9):2177–2182.

[7] Bacigaluppi, M., Comi, G., and Hermann, D. M. (2010). Animal models of ischemic stroke. Part two: modeling cerebral ischemia. *Open Neurol J*, 4:34–38.

[8] Banks, A., Vincent, J., and Anyakoha, C. (2008). A review of particle swarm optimization. part ii: hybridisation, combinatorial, multicriteria and constrained optimization, and indicative applications. *Natural Computing*, 7(1):109–124.

[9] Barnard, J. and Speake, D. (2004). In open heart surgery is there a role for the use of carbon dioxide field flooding techniques to reduce the level of post-operative gaseous emboli? *Interactive CardioVascular and Thoracic Surgery*, 3(4):599–602.

[10] Beare, R. J., Das, G., Ren, M., Chong, W., Sinnott, M. D., Hilton, J. E., Srikanth, V., and Phan, T. G. (2011). Does the principle of minimum work apply at the carotid bifurcation: a retrospective cohort study. *BMC Med Imaging*, 11:17–17. 1471-2342-11-17[PII].

[11] Bebber, D. P., Hynes, J., Darrah, P. R., Boddy, L., and Fricker, M. D. (2007). Biological solutions to transport network design. *Proceedings of the Royal Society B Biological Sciences*, 274(1623):2307–2315.

[12] Blum, C. (2005). Ant colony optimization: Introduction and recent trends. *Physics of Life reviews*, 2(4):353–373.

[13] Breu, H., Gil, J., Kirkpatrick, D., and Werman, M. (1995). Linear time euclidean distance transform algorithms. *Pattern Analysis and Machine Intelligence, IEEE Transactions on*, 17(5):529–533.

[14] Bruinsma, P., Arts, T., Dankelman, J., and Spaan, J. A. (1988). Model of the coronary circulation based on pressure dependence of coronary resistance and compliance. *Basic Research in Cardiology*, 83(5):510–524.

[15] Bruyninckx, P., Loeckx, D., Vandermeulen, D., and Suetens, P. (2010). Segmentation of liver portal veins by global optimization. *Imaging*, 7624:76241Z–76241Z–12.

[16] Bui, A. V., Manasseh, R., Liffman, K., and Sutalo, I. D. (2010). Development of optimized vascular fractal tree models using level set distance function. *Medical Engineering & Physics*, 32(7):790–794.

[17] Bushi, D., Grad, Y., Einav, S., Yodfat, O., Nishri, B., and Tanne, D. (2005). Hemodynamic evaluation of embolic trajectory in an arterial bifurcation: An in-vitro experimental model. *Stroke*, 36(12):2696–2700.

[18] Calabrese, L. H., Dodick, D. W., Schwedt, T. J., and Singhal, A. B. (2007). Narrative review: reversible cerebral vasoconstriction syndromes. *Annals of internal medicine*, 146(1):34–44.

[19] Carr, I. A., Nemoto, N., Schwartz, R. S., and Shadden, S. C. (2013). Size-dependent predilections of cardiogenic embolic transport. *American Journal of Physiology - Heart and Circulatory Physiology*, 305(5):H732–H739.

[20] Casals, J. B., Pieri, N. C., Feitosa, M. L., Ercolin, A. C., Roballo, K. C., Barreto, R. S., Bressan, F. F., Martins, D. S., Miglino, M. A., and Ambr6sio, C. E. (2011). The use of animal models for stroke research: A review. *Comp Med*, 61(4):305–313. 2011000305[PII].

[21] Cassot, F., Lauwers, F., Fouard, C., Prohaska, S., and Lauwers-Cances, V. (2006a). A novel three-dimensional computer-assisted method for a quantitative study of microvascular networks of the human cerebral cortex. *Microcirculation (New York, N.Y. : 1994)*, 13(1):1–18.

[22] Cassot, F., Lauwers, F., Fouard, C., Prohaska, S., and LAUWERS-CANCES, V. (2006b). A novel three-dimensional computer-assisted method for a quantitative study of microvascular networks of the human cerebral cortex. *Microcirculation*, 13(1):1–18.

[23] Changizi, M. A. and Cherniak, C. (2000). Modeling the large-scale geometry of human coronary arteries. *Canadian journal of physiology and pharmacology*, 78(8):603–611.

[24] Chung, E. M., Hague, J. P., Chanrion, M.-A., Ramnarine, K. V., Katsogridakis, E., and Evans, D. H. (2010a). Embolus trajectory through a physical replica of the major cerebral arteries. *Stroke*, 41(4):647–652.

[25] Chung, E. M., Hague, J. P., Chanrion, M.-A., Ramnarine, K. V., Katsogridakis, E., and Evans, D. H. (2010b). Embolus trajectory through a physical replica of the major cerebral arteries. *Stroke*, 41(4):647–652.

[26] Chung, E. M. L., Hague, J. P., and Evans, D. H. (2007a). Revealing the mechanisms underlying embolic stroke using computational modelling. *Physics in Medicine and Biology*, 52(23):7153.

[27] Chung, E. M. L., Hague, J. P., and Evans, D. H. (2007b). Revealing the mechanisms underlying embolic stroke using computational modelling. *Physics in Medicine and Biology*, 52(23):7153.

[28] Cohen, D. (1994). Voxel traversal along a 3d line. *Graphics gems IV*, 4:366.

[29] College, O. (2013). *Anatomy and Physiology [ISBN 978-1-938168-13-0, Available at Connexions Web site, http://cnx.org/content/col11496/1.6/]*.

[30] Cross, S. S., Start, R. D., Silcocks, P. B., Bull, A. D., Cotton, D. W., and Underwood, J. C. (1993). Quantitation of the renal arterial tree by fractal analysis. *The Journal of pathology*, 170(4):479–484.

[31] Dorigo, M. and Blum, C. (2005). Ant colony optimization theory: A survey. *Theoretical computer science*, 344(2):243–278.

[32] Duncker, D. J. and Bache, R. J. (2008). Regulation of coronary blood flow during exercise. *Physiological reviews*, 88(3):1009–1086.

[33] Endo, K., Sata, N., Ishiguro, Y., Miki, A., Sasanuma, H., Sakuma, Y., Shimizu, A., Hyodo, M., Lefor, A., and Yasuda, Y. (2014). A patient-specific surgical simulator using preoperative imaging data: an interactive simulator using a three-dimensional tactile mouse. *Journal of Computational Surgery*, 1(1).

[34] Enzmann, D. R., Ross, M. R., Marks, M. P., and Pelc, N. J. (1994). Blood flow in major cerebral arteries measured by phase-contrast cine mr. *American Journal of Neuroradiology*, 15(1):123–9.

[35] Fabbri, D., Long, Q., Das, S., and Pinelli, M. (2014). Computational modelling of emboli travel trajectories in cerebral arteries: influence of microembolic particle size and density. *Biomech Model Mechanobiol*, 13(2):289–302.

[36] Faraci, F. M. and Heistad, D. D. (1990). Regulation of large cerebral arteries and cerebral microvascular pressure. *Circulation Research*, 66(1):8–17.

[37] Federspiel, W. J. and Popel, A. S. (1986). A theoretical analysis of the effect of the particulate nature of blood on oxygen release in capillaries. *Microvascular Research*, 32(2):164 - 189.

[38] Frackowiak, R. S., Lenzi, G.-L., Jones, T., and Heather, J. D. (1980). Quantitative measurement of regional cerebral blood flow and oxygen metabolism in man using 15o and positron emission tomography: theory, procedure, and normal values. *Journal of computer assisted tomography*, 4(6):727–736.

[39] Fraenkel, G. and Herford, G. (1938). The Respiration of Insects Through the Skin. *Journal of Experimental Biology.*

[40] Frame, M. and Sarelius, I. (1995). Energy optimization and bifurcation angles in the microcirculation. *Microvascular research*, 50:301–310.

[41] Georg, A. M., Preusser, T., Hahn, H. K., and Georg, M. (2010). Global Constructive Optimization of Vascular Systems Global Constructive Optimization of Vascular Systems. *Most*, (314).

[42] Gharib, A. M., Ho, V. B., Rosing, D. R., Herzka, D. A., Stuber, M., Arai, A. E., and Pettigrew, R. I. (2008). *Radiology*, 247(1):220–227.

[43] Glenny, R., Bernard, S., Neradilek, B., and Polissar, N. (2007). *Proceedings of the National Academy of Sciences of the United States of America*, 104(16):6858–6863.

[44] Grassberger, P. (1985). Generalizations of the hausdorff dimension of fractal measures. *Physics Letters A*, 107(3):101–105.

[45] HAGUE, J. P. and CHUNG, E. M. L. (2009). Similarities between embolic stroke and percolation problems. *International Journal of Modern Physics B*, 23(20n21):4150–4157.

[46] Hague, J. P. and Chung, E. M. L. (2009). Statistical physics of cerebral embolization leading to stroke. *Phys. Rev. E*, 80:051912.

[47] Hajek, B. (1988). Cooling schedules for optimal annealing. *Mathematics of operations research*, 13(2):311–329.

[48] Hall, J. E. (2010). *Guyton and Hall Textbook of Medical Physiology.* Elsevier.

[49] Haynes, R. H. and Burton, A. C. (1959). Role of the non-newtonian behavior of blood in hemodynamics. *American Journal of Physiology – Legacy Content*, 197(5):943–950.

[50] Hinkle, J. L. and Guanci, M. M. (2007). Acute ischemic stroke review. *Journal of Neuroscience Nursing*, 39(5):285–293.

[51] HOOD, W. P., THOMSON, W. J., RACKLEY, C. E., and ROLETT, E. L. (1969). Comparison of calculations of left ventricular wall stress in man from thin-walled and thick-walled ellipsoidal models. *Circulation Research*, 24(4):575–582.

[52] Horsfield, K. and Woldenberg, M. J. (1989). Diameters and cross-sectional areas of branches in the human pulmonary arterial tree. *The Anatomical record*, 223(3):245–251.

[53] Houck, C. R., Joines, J., and Kay, M. G. (1995). A genetic algorithm for function optimization: a matlab implementation. *NCSU-IE TR*, 95(09).

[54] Ingber, L. and Rosen, B. (1992). Genetic algorithms and very fast simulated reannealing: A comparison. *Mathematical and Computer Modelling*, 16(11):87–100.

[55] Jiang, Z. L., Kassab, G. S., and Fung, Y. C. (1994). Diameter-defined Strahler system and connectivity matrix of the pulmonary arterial tree. *J. Appl. Physiol.*, 76(2):882–892.

[56] Johnson, K., Sharma, P., and Oshinski, J. (2008). *Journal of Biomechanics*, 41(3):595–602.

[57] Johnson, P. C. (1986a). Autoregulation of blood flow. *Circulation Research*, 59(5):483–95.

[58] Johnson, P. C. (1986b). Brief review: Autoregulation of blood flow. *Circ Res*, 59:483–495.

[59] Kaimovitz, B., Huo, Y., Lanir, Y., and Kassab, G. S. (2008). *American journal of physiology Heart and circulatory physiology*, 294(2):H714–H723.

[60] Kaimovitz, B., Lanir, Y., and Kassab, G. S. (2005a). Large-scale 3-d geometric reconstruction of the porcine coronary arterial vasculature based on detailed anatomical data. *Annals of biomedical engineering*, 33(11):1517–1535.

[61] Kaimovitz, B., Lanir, Y., and Kassab, G. S. (2005b). Large-scale 3-D geometric reconstruction of the porcine coronary arterial vasculature based on detailed anatomical data. *Annals of biomedical engineering*, 33(11):1517–35.

[62] Kamiya, A. and Takahashi, T. (2007). Quantitative assessments of morphological and functional properties of biological trees based on their fractal nature. *Journal of Applied Physiology*, 102(6):2315–2323.

[63] Karau, K. L., Molthen, R. C., Dhyani, A., Haworth, S. T., Hanger, C. C., Roerig, D. L., Johnson, R. H., and Dawson, C. A. (2001). Pulmonary arterial morphometry from microfocal X-ray computed tomography. *Am. J. Physiol. Heart Circ. Physiol.*, 281(6):H2747–2756.

[64] Karch, R., Neumann, F., Neumann, M., and Schreiner, W. (1999). A three-dimensional model for arterial tree representation, generated by constrained constructive optimization. *Computers in biology and medicine*, 29(1):19–38.

[65] Karch, R., Neumann, F., Neumann, M., and Schreiner, W. (2000). Staged growth of optimized arterial model trees. *Annals of Biomedical Engineering*, 28(5):495–511.

[66] Kassab, G. S. (2006). Scaling laws of vascular trees: of form and function. *American journal of physiology. Heart and circulatory physiology*, 290(2):H894–903.

[67] Kassab, G. S. and Fung, Y. C. (1994). Topology and dimensions of pig coronary capillary network. *American Journal of Physiology*, 267(1 Pt 2):H319–H325.

[68] Kassab, G. S., Pallencaoe, E., Schatz, A., and Fung, Y. C. (1997). Longitudinal position matrix of the pig coronary vasculature and its hemodynamic implications. *American Journal of Physiology*, 273(6 Pt 2):H2832–H2842.

[69] Kassab, G. S., Rider, C. A., Tang, N. J., and Fung, Y. C. (1993a). Morphometry of pig coronary arterial trees. *American Journal of Physiology*, 265(1):H350–65.

[70] Kassab, G. S., Rider, C. A., Tang, N. J., and Fung, Y.-C. (1993b). Morphometry of pig coronary arterial trees. *American Journal of Physiology-Heart and Circulatory Physiology*, 265(1):H350–H365.

[71] Kennedy, J. (2010). Particle swarm optimization. In *Encyclopedia of Machine Learning*, pages 760–766. Springer.

[72] Kiselev, V. and Posse, S. (1999). Analytical model of susceptibility-induced mr signal dephasing: effect of diffusion in a microvascular network. *Magnetic resonance in medicine*, 41(3):499–509.

[73] Klocke, F., Bunnell, I., Greene, D., Wittenberg, S., and Visco, J. (1974). *Circulation*, 50(3):547–549.

[74] Koushanpour, E. and Collings, W. (1966a). Validation and dynamic applications of an ellipsoid model of the left ventricle. *Journal of applied physiology*, 21(5):1655–1661.

[75] Koushanpour, E. and Collings, W. D. (1966b). Validation and dynamic applications of an ellipsoid model of the left ventricle. *Journal of Applied Physiology*, 21(5):1655–1661.

[76] Krabbe-Hartkamp, M. J., Van der Grond, J., De Leeuw, F., De Groot, J., Algra, A., Hillen, B., Breteler, M., and Mali, W. (1998). Circle of willis: morphologic variation on three-dimensional time-of-flight mr angiograms. *Radiology*, 207(1):103–111.

[77] Krams, R., Wentzel, J., Oomen, J., Vinke, R., Schuurbiers, J., De Feyter, P., Serruys, P., and Slager, C. (1997). Evaluation of endothelial shear stress and 3d geometry as factors determining the development of atherosclerosis and remodeling in human coronary arteries in vivo combining 3d reconstruction from angiography and ivus (angus) with computational fluid dynamics. *Arteriosclerosis, thrombosis, and vascular biology*, 17(10):2061–2065.

[78] Kretowski, M., Rolland, Y., Bézy-Wendling, J., and Coatrieux, J.-L. (2003). Fast algorithm for 3-D vascular tree modeling. *Computer methods and programs in biomedicine*, 70(2):129–36.

[79] Ku, D. (1997a). Blood flow in arteries. *ANNUAL REVIEW OF FLUID MECHANICS*, 29:399–434.

[80] Ku, D. N. (1997b). Blood flow in arteries. *Annual Review of Fluid Mechanics*, 29(1):399–434.

[81] Kumar, M., Husian, M., Upreti, N., and Gupta, D. (2010). Genetic algorithm: Review and application. *International Journal of Information Technology and Knowledge Management*, 2(2):451–454.

[82] Landini, G., Misson, G. P., and Murray, P. I. (1993). Fractal analysis of the normal human retinal fluorescein angiogram. *Current eye research*, 12(1):23–27.

[83] Lapi, D., Marchiafava, P. L., and Colantuoni, A. (2008). Geometric characteristics of arterial network of rat pial microcirculation. *Journal of Vascular Research*, 45(1):69–77.

[84] Lewis, R. M., Torczon, V., and Trosset, M. W. (2000). Direct search methods: then and now. *Journal of computational and Applied Mathematics*, 124(1):191–207.

[85] Liu, P., Uh, J., Devous, M. D., Adinoff, B., and Lu, H. (2012). Comparison of relative cerebral blood flow maps using pseudo-continuous arterial spin labeling and single photon emission computed tomography. *NMR in Biomedicine*, 25(5):779–786.

[86] Liu, Y. and Kassab, G. S. (2007). *American journal of physiology Heart and circulatory physiology*, 292(3):H1336–H1339.

[87] Lorthois, S., Cassot, F., and Lauwers, F. (2011). Simulation study of brain blood flow regulation by intra-cortical arterioles in an anatomically accurate large human vascular network. part ii: flow variations induced by global or localized modifications of arteriolar diameters. *Neuroimage*, 54(4):2840–2853.

[88] M. Monma, T. Saito, Y. Yonezawa, T. I., Monma, M., Saito, T., Yonezawa, Y., and Igarashi, T. (2000). Circulation Transport Phenomena Involving the Interaction between Arterial and Venous Vessel Systems Based on a Simulation Using Fractal Properties. *Complex Systems*, 12:457–464.

[89] Matsukubo, H., Matsuura, T., Endo, N., Asayama, J., and Watanabe, T. (1977). Echocardiographic measurement of right ventricular wall thickness. a new application of subxiphoid echocardiography. *Circulation*, 56(2):278–84.

[90] Mayerich, D., Abbott, L., and Keyser, J. (2008). Visualization of cellular and microvascular relationships. *IEEE Transactions on Visualization and Computer Graphics*, 14(6):1611–1618.

[91] Mitchell, G. F., van Buchem, M. A., Sigurdsson, S., Gotal, J. D., Jonsdottir, M. K., Kjartansson, Ó., Garcia, M., Aspelund, T., Harris, T. B., Gudnason, V., et al. (2011). Arterial stiffness, pressure and flow pulsatility and brain structure and function: the age, gene/environment susceptibility–reykjavik study. *Brain*, 134(11):3398–3407.

[92] Morris, P. D., Narracott, A., von Tengg-Kobligk, H., Silva Soto, D. A., Hsiao, S., Lungu, A., Evans, P., Bressloff, N. W., Lawford, P. V., Hose, D. R., and Gunn, J. P. (2015). Computational fluid dynamics modelling in cardiovascular medicine. *Heart*.

[93] Mukherjee, D. and Shadden, S. C. (2014). A patient-specific cfd-based study of embolic particle transport for stroke. *Bulletin of the American Physical Society*, 59.

[94] Murray, C. D. (1926). The Physiological Principle of Minimum Work: I. The Vascular System and the Cost of Blood Volume. *Proceedings of the National Academy of Sciences of the United States of America*, 12(3):207–14.

[95] Murray, C. D. (1927). a Relationship Between Circumference and Weight in Trees and Its Bearing on Branching Angles. *The Journal of general physiology*, 10(5):725–9.

[96] Muth, C. M. and Shank, E. S. (2000). Gas embolism. *New England Journal of Medicine*, 342(7):476–482.

[97] Nakamura, Y. and Awa, S. (2014a). Radius exponent in elastic and rigid arterial models optimized by the least energy principle. *Physiol Rep*, 2(2):e00236. phy2236[PII].

[98] Nakamura, Y. and Awa, S. (2014b). Radius exponent in elastic and rigid arterial models optimized by the least energy principle. *Physiol Rep*, 2(2):e00236. phy2236[PII].

[99] Navarrete, A., van Schaik, C. P., and Isler, K. (2011). Energetics and the evolution of human brain size. *Nature*, 480(7375):91–93.

[100] Neumann, F., Schreinerb, W., and Neumann, M. (1997). Computer simulation of coronary arterial trees. *Optimization*, 9978(97).

[101] Nishimura, N., Rosidi, N. L., Iadecola, C., and Schaffer, C. B. (2010). Limitations of collateral flow after occlusion of a single cortical penetrating arteriole. *Journal of cerebral blood flow and metabolism : official journal of the International Society of Cerebral Blood Flow and Metabolism*, 30(12):1914–1927.

[102] Olufsen, M. S. (1999). Structured tree outflow condition for blood flow in larger systemic arteries. *American journal of physiology-Heart and circulatory physiology*, 276(1):H257–H268.

[103] O'Rourke, M. F. and Avolio, A. P. (1980). Pulsatile flow and pressure in human systemic arteries. studies in man and in a multibranched model of the human systemic arterial tree. *Circulation Research*, 46(3):363–72.

[104] Orset, C., Macrez, R., Young, A. R., Panthou, D., Angles-Cano, E., Maubert, E., Agin, V., and Vivien, D. (2007). Mouse model of in situ thromboembolic stroke and reperfusion. *Stroke*, 38(10):2771–2778.

[105] Ozgel, O., Haligur, A., Dursun, N., and Karakurum, E. (2004). *Anat. Histol. Embryol*, 33:278–283.

[106] Painter, P., Edén, P., and Bengtsson, H.-U. (2006). Pulsatile blood flow, shear force, energy dissipation and murray's law. *Theoretical Biology and Medical Modelling*, 3(1).

[107] PHAN, T. G., Hilton, J., Beare, R., Srikanth, V., and Sinnott, M. (2014). Computer modelling of anterior circulation stroke: Proof of concept in cerebrovascular occlusion. *Frontiers in Neurology*, 5(176).

[108] Pollanen, M. (1992). Dimensional optimization at different levels of the arterial hierarchy. *Journal of theoretical biology*, 159(2):267–270.

[109] Pollanen, M. S. (1991). Behaviour of suspended particles at bifurcations: implications for embolism. *Physics in Medicine and Biology*, 36(3):397.

[110] Pries, A., Ley, K., Claassen, M., and Gaehtgens, P. (1989). Red cell distribution at microvascular bifurcations. *Microvascular Research*, 38(1):81 – 101.

[111] Pries, A. R. and Secomb, T. W. (2009). *Cardiovascular Research*, 81(2):328–335.

[112] Restrepo, J. G., Ott, E., and Hunt, B. R. (2006). Scale dependence of branching in arterial and bronchial trees. *Phys. Rev. Lett.*, 96:128101.

[113] Revellin, R., Rousset, F., Baud, D., and Bonjour, J. (2009). Extension of murray's law using a non-newtonian model of blood flow. *Theor Biol Med Model*, 6:7–7. 1742-4682-6-7[PII].

[114] Riva, C. E., Grunwald, J. E., Sinclair, S. H., and Petrig, B. (1985). Blood velocity and volumetric flow rate in human retinal vessels. *Investigative ophthalmology & visual science*, 26(8):1124–1132.

[115] Rordorf, G., Koroshetz, W. J., Copen, W. A., Cramer, S. C., Schaefer, P. W., Budzik, R. F., Schwamm, L. H., Buonanno, F., Sorensen, A. G., and Gonzalez, G. (1998). Regional ischemia and ischemic injury in patients with acute middle cerebral artery stroke as defined by early diffusion-weighted and perfusion-weighted mri. *Stroke*, 29(5):939–943.

[116] Rossitti, S. and Löfgren, J. (1993). Vascular dimensions of the cerebral arteries follow the principle of minimum work. *Stroke: A Journal of Cerebral Circulation*, 24(3):371–377.

[117] Runions, A., Fuhrer, M., Lane, B., Federl, P., Rolland-Lagan, A.-G., and Prusinkiewicz, P. (2005). Modeling and visualization of leaf venation patterns. *ACM SIGGRAPH 2005 Papers on SIGGRAPH 05*, 24(1):702.

[118] Schreiner, W. and Buxbaum, P. F. (1993). Computer-optimization of vascular trees. *IEEE transactions on bio-medical engineering*, 40(5):482–91.

[119] Schreiner, W., Karch, R., Neumann, M., Neumann, F., Szawlowski, P., and Roedler, S. (2006). Optimized arterial trees supplying hollow organs. *Medical Engineering & Physics*, 28(5):416–429.

[120] Schreiner, W., Neumann, F., and Mohl, W. (1990). The role of intramyocardial pressure during coronary sinus interventions: a computer model study. *IEEE Transactions on Biomedical Engineering*, 37(10):956–967.

[121] Sefidgar, M., Soltani, M., Raahemifar, K., Sadeghi, M., Bazmara, H., Bazargan, M., and Naeenian, M. M. (2015). Numerical modeling of drug delivery in a dynamic solid tumor microvasculature. *Microvascular Research*, 99:43 – 56.

[122] Shaughnessy, E. J. (2010). Introduction to fluid mechanics.

[123] Stefani, M. A., Schneider, F. L., Marrone, A. C. H., and Severino, A. G. (2013a). Influence of the gender on cerebral vascular diameters observed during the magnetic resonance angiographic examination of willis circle. *Brazilian Archives of Biology and Technology*, 56:45 – 52.

[124] Stefani, M. A., Schneider, F. L., Marrone, A. C. H., and Severino, A. G. (2013b). Influence of the gender on cerebral vascular diameters observed during the magnetic resonance angiographic examination of willis circle. *Brazilian Archives of Biology and Technology*, 56:45 – 52.

[125] Stein, P. and Barzilay, J. (2011). Abnormal heart rate turbluence predicts cardiac mortality in low, intermediate and high risk older adults. *Journal of cardiovascular electrophysiology*, 22:122–127.

[126] Stein, P. D. and Sabbah, H. N. (1976). Turbulent blood flow in the ascending aorta of humans with normal and diseased aortic valves. *Circulation Research*, 39(1):58–65.

[127] Sun, Y. and Gewirtz, H. (1988). Estimation of intramyocardial pressure and coronary blood flow distribution. *American Journal of Physiology*, 255(3 Pt 2):H664–H672.

[128] Sunni, S., Bishop, S. P., Kent, S. P., and Geer, J. C. (1986). *Archives of pathology laboratory medicine*, 110(5):375–381.

[129] Šutalo, I., Bui, A., Liffman, K., and Manasseh, R. (2011). Modelling of embolus transport and embolic stroke. *Environmental Health and Biomedicine, WIT Transactions on Biomedicine and Health*, 15:347–358.

[130] Thompson, D. and Bilbro, G. (2000). Comparison of a genetic algorithm with a simulated annealing algorithm for the design of an atm network. *Communications Letters, IEEE*, 4(8):267–269.

[131] TROY, B. L., POMBO, J., and RACKLEY, C. E. (1972). Measurement of left ventricular wall thickness and mass by echocardiography. *Circulation*, 45(3):602–611.

[132] Uren, N. G., Melin, J. A., De Bruyne, B., Wijns, W., Baudhuin, T., and Camici, P. G. (1994). Relation between myocardial blood flow and the severity of coronary-artery stenosis. *New England Journal of Medicine*, 330(25):1782–1788.

[133] van den Broek, J. and van den Broek, M. (1980). Application of an ellipsoidal heart model in studying left ventricular contractions. *Journal of Biomechanics*, 13(6):493 – 503.

[134] Van Den Broek, J. J. J. M. and Van Den Broek, M. H. L. M. (1980). *J. Biomechanics*, 13:493–503.

[135] Van Laarhoven, P. J. and Aarts, E. H. (1987). *Simulated annealing: theory and applications*, volume 37. Springer Science & Business Media.

[136] Vermeer, S. E., Longstreth, W. T., and Koudstaal, P. J. (2007). Silent brain infarcts: a systematic review. *The Lancet Neurology*, 6(7):611–619.

[137] Vinnakota, K. C. and Bassingthwaighte, J. B. (2004). Myocardial density and composition: a basis for calculating intracellular metabolite concentrations. *American Journal of Physiology-Heart and Circulatory Physiology*, 286(5):H1742–H1749.

[138] Wang, Y.-Y. L., Hsu, T.-L., Jan, M.-Y., and Wang, W.-K. (2010). Review: theory and applications of the harmonic analysis of arterial pressure pulse waves. *Journal of Medical and Biological Engineering*, 30(3):125–131.

[139] Watkins, K., Paus, T., Lerch, J., Zijdenbos, A., Collins, D., Neelin, P., Taylor, J., Worsley, K., and Evans, A. (2001). Structural asymmetries in the human brain: a voxel-based statistical analysis of 142 mri scans. *Cerebral Cortex*, 11(9):868–877.

[140] West, G. B., Brown, J. H., and Enquist, B. J. (1997). A general model for the origin of allometric scaling laws in biology. *Science*, 276(5309):122–126.

[141] West, G. B., Brown, J. H., and Enquist, B. J. (2011). A General Model for the Origin of Allometric Scaling Laws in Biology. *Yeast*, 122(1997).

[142] Wilkinson, I., Bull, J., du Boulay, G., Marshall, J., Russell, R., and Symon, L. (1969). The heterogeneity of blood flow throughout the normal cerebral hemisphere. In Brock, M., Fieschi, C., Ingvar, D., Lassen, N., and Schürmann, K., editors, *Cerebral Blood Flow*, pages 17–18. Springer Berlin Heidelberg.

[143] Wischgoll, T., Choy, J. S., and Kassab, G. S. (2009). Extraction of morphometry and branching angles of porcine coronary arterial tree from CT images. *American journal of physiology. Heart and circulatory physiology*, 297(5):H1949–55.

[144] Wright, S. (2013). *Using Digital Reconstructions, Morphometry, and Computational Models to Generate Novel Maps of Human Brain Vascular Architecture*. PhD thesis, George Mason University.

[145] Wright, S. N., Kochunov, P., Mut, F., Bergamino, M., Brown, K. M., Mazziotta, J. C., Toga, A. W., Cebral, J. R., and Ascoli, G. A. (2013). Digital reconstruction and morphometric analysis of human brain arterial vasculature from magnetic resonance angiography. *NeuroImage*, 82:170–181.

[146] Yoldas, A., Ozmen, E., and Ozdemir, V. (2010). *Journal of the South African Veterinary Association*, 81(4):247–252.

[147] Zamir, M. (1976). *Journal of Theoretical Biology*, pages 227–251.

[148] Zamir, M. (1982). Local geometry of arterial branching. *Bulletin of Mathematical Biology*, 44(5):597–607.

[149] Zamir, M. (2001). Fractal dimensions and multifractility in vascular branching. *Journal of theoretical biology*, 212(2):183–90.

[150] Zamir, M. and Bigelow, D. (1984). Cost of departure from optimality in arterial branching. *Journal of Theoretical Biology*, 109(3):401–409.

[151] Zamir, M. and Chee, H. (1987). Segment analysis of human coronary arteries. *Blood Vessels*, 24(1-2):76–84.

[152] Zamir, M. and Medeiros, J. A. (1982). Arterial Branching in Man and Monkey. 79(March):353–360.

[153] Zamir, M., Medeiros, J. A., and Cunningham, T. K. (1979). Arterial bifurcations in the human retina. *The Journal of general physiology*, 74(4):537–548.

[154] Zamir, M., Wrigley, S. M., and Langille, B. L. (1983). Arterial bifurcations in the cardiovascular system of a rat. *The Journal of general physiology*, 81(3):325–35.

[155] Zang, H., Zhang, S., and Hapeshi, K. (2010). A review of nature-inspired algorithms. *Journal of Bionic Engineering*, 7:S232–S237.

[156] Zhou, Y., Kassab, G. S., and Molloi, S. (1999). *Sciences-New York*, 2929.